National Aeronautics and Space Administration

Integrating GPS, strong motion and teleseismic data for tsunami early detection

Kejie Chen (329B)
Tony Song (329B) and Zhen Liu (329A)

Introduction

The "GPS-aided Real-Time Earthquake And Tsunami (GREAT) Alert System", which utilizes coastal GPS data for estimation of submarine earthquake features and resulting tsunamis, has been set up and operated at JPL.

Advantages of GPS :

- ✓ Directly measure dynamic ground displacements at cm to mm level accuracy without saturation.
- ✓ Provide important constraints on the location and extent of the rupture plane, unambiguous resolution of the nodal plane

Limitations of GPS :

- ✓ Dense GPS network exists only in areas such as California and Japan
- ✓ Only part of the data is publicly available (see in Fig. 1)
- ✓ Earthquake signal decays very fast and can be beyond the detection ability of GPS

Research objectives:

To overcome the limitations of GPS by utilizing all available real-time data for rapid seismic source estimation and tsunami early warning.

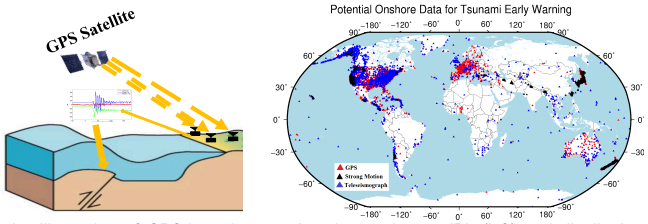

Fig. 1 : Illustration of GPS-based tsunami early warning at JPL (left) and distribution of publically available GPS, strong motion and teleseismic data (right).

Data and Method

Strong motion data: accelerometers, low cost, high frequency (100-200 Hz), easy to install at key locations. More sensitive than GPS, but there is drift when integrating acceleration to displacements, which can be corrected by Kalman filter when collocated with GPS.

Teleseismic data: velocities, have the highest precision, designed to record motions at distant locations and globally distributed (see in Fig. 1). Most of the data are publically available, but will saturate in near field.

Method: We have developed a strategy and an algorithm to integrate these three real-time data for rapid inversion of large earthquakes:

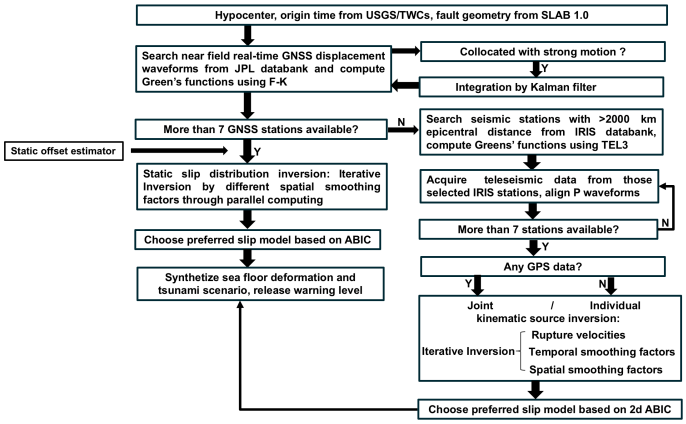

Fig. 2 : Diagram of earthquake source inversion and tsunami early warning using GPS, strong motion and teleseismic data.

National Aeronautics and Space Administration
Jet Propulsion Laboratory
California Institute of Technology
Pasadena, California

www.nasa.gov

Results and Implications

Retrospective analysis of three historical events

Here we show three typical results by our method: the 2011 Tohoku tsunami with dense GPS network, the 2015 Illapel tsunami with sparse GPS network, and the 2016 Solomon tsunami without nearby GPS data (Fig.3).

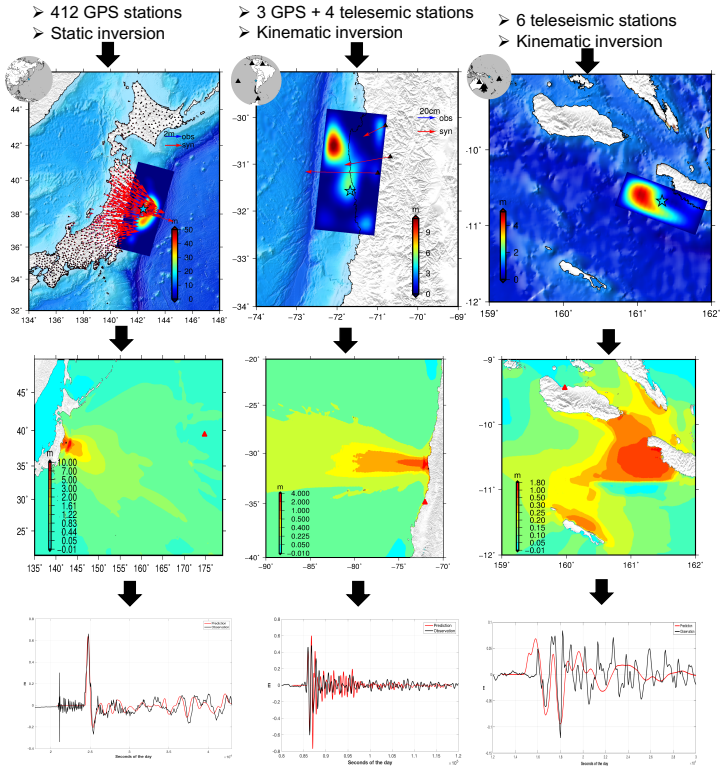

Fig. 3 : Slip distribution model (top), maximum tsunami wave amplitude (middle) and comparisons between predicted and recorded wave heights at selected tide gauges.

Improvement and future work

To show the improvement, we have analyzed all of Mw > 7.0 earthquakes (most are tsunamigenic subduction earthquakes) since 1990 by comparing the responding time (see in Fig. 4) for earthquake source inversion. As expected, near filed GPS/strong motion data are not always available and may affect tsunami warning severely (left). By integrating with teleseismic data, the responding time can be reduce by a half (right). As an on-going project, we are testing and improving our algorithms for a more reliable tsunami early warning system.

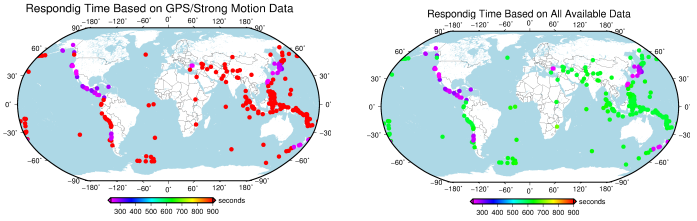

Fig.4 :Time needed for earthquake source inversion: (right) using GPS and strong motion data only, and (right) using all three data, for all Mw>7.0 earthquakes (color dots on the map) since 1990.

Poster No. EB-01

Forcing of eddy variability in the southern subtropical Indian Ocean, from remotely sensed altimeter and scatterometer data

Author: Andrew Delman (329B)
Co-Authors: Tong Lee (329B), Bo Qiu (U. Hawai'i)

Motivation

- Mesoscale eddies play a critical role in the ocean's contribution to the global energy cycle, and also affect biogeochemical conditions for marine life
- In the Indian Ocean, eddy activity varies substantially from year to year, influenced by changes in winds and ocean currents
- **Understanding** and **predicting** the interannual variability of eddy activity improves projections of regional changes in climate and biological productivity

Study region

- A band of elevated mesoscale eddy activity spans the **southern subtropical Indian Ocean (SSIO)** between Africa and Australia

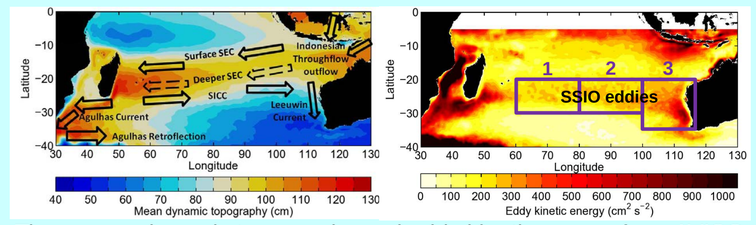

Time-mean dynamic topography and eddy kinetic energy from AVISO

Data sources

- Sea level anomaly (SLA) from the AVISO merged altimeter product
  - Merged data from TOPEX/Poseidon, Jason-1/2, ERS-1/2, ENVISAT, and other satellite missions
- 10 m (surface) wind data from the CCMP merged scatterometer product
  - Merged data from QuikSCAT, AQUA, TRMM, DMSP, Coriolis, and other satellite missions
- Niño3.4 index (indicator of El Niño-Southern Oscillation) from NOAA ERSSTv4 data

Research question

- **Which remote and local features in the ocean-atmosphere system, detected by remote sensing data, drive eddy kinetic energy (EKE) variability in the SSIO?**

Hypothesis

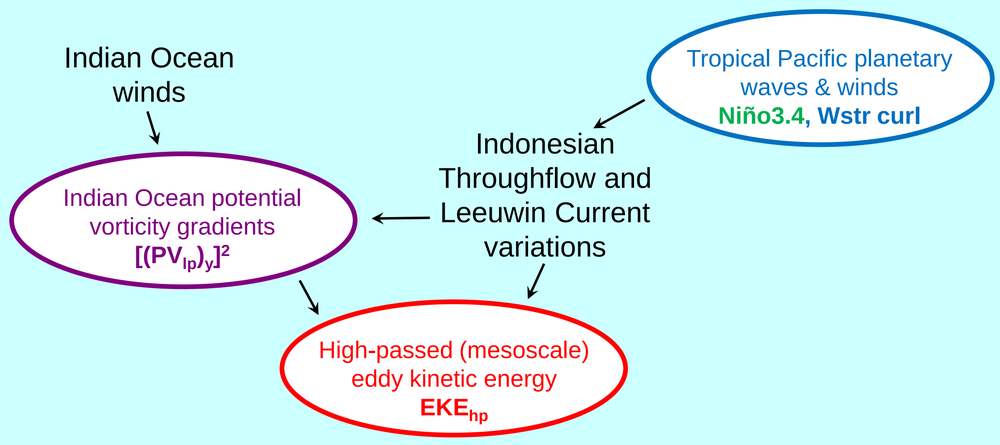

Method

- Decompose sea level anomaly into low-passed (larger-scale) and high-passed (mesoscale) components

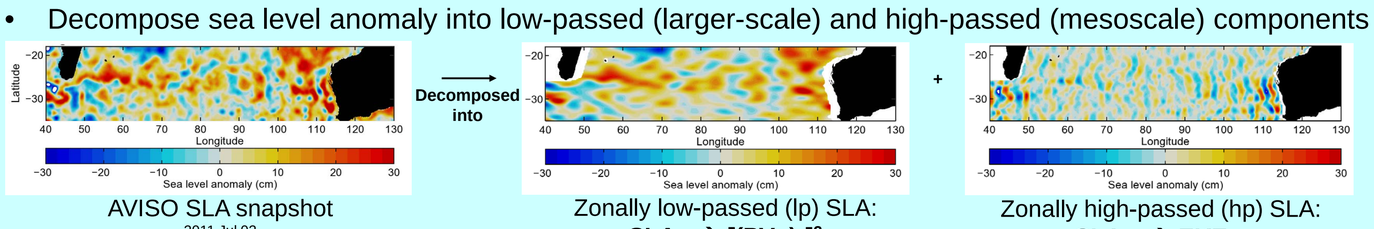

AVISO SLA snapshot
2011 Jul 02

Zonally low-passed (lp) SLA:
SLA$_{lp}$ → [(PV$_{lp}$)$_y$]^2

Zonally high-passed (hp) SLA:
SLA$_{hp}$ → EKE$_{hp}$

Use lagged correlations and time series to compare:

- **EKE$_{hp}$**, an indicator of mesoscale eddy activity derived from SLA$_{hp}$
- Variance of meridional potential vorticity gradient **[(PV$_{lp}$)$_y$]^2**, an indicator of flow instability, derived from SLA$_{lp}$
- The **curl of surface wind stress**, which induces vertical motions in the ocean
- **Niño3.4 index**, an indicator of El Niño-Southern Oscillation (ENSO)

Results: Local forcing

- A necessary condition for the instability that generates mesoscale eddies is that the meridional gradient of potential vorticity (PV) changes sign (e.g., Charney and Stern, 1962)
- The barotropic component of this condition (which can be estimated at the surface using SLA) is $\partial/\partial y[f + v_x - u_y] < 0$, here notated as $(PV)_y < 0$
- $(PV)_y$ is usually positive; however if the variance in $(PV)_y$ values is sufficiently high, then its value will likely cross zero in some locations

Optimum (maximum magnitude) correlations of [(PV$_{lp}$)$_y$]^2 leading 〈EKE$_{hp}$〉, with lead times in the range 0-24 months.
The correlations are on interannual timescales, i.e., data are pre-processed with a 14-month low-pass temporal filter.

Corr. [(PV$_{lp}$)$_y$]^2 with 〈EKE$_{hp}$〉 in box 1 (60°-80°E)

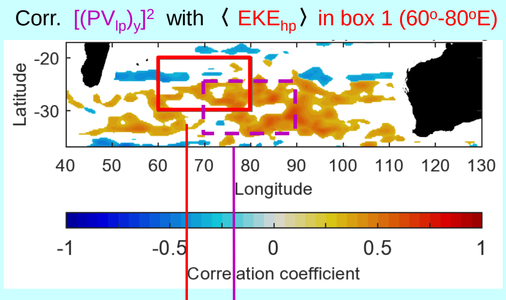

Corr. [(PV$_{lp}$)$_y$]^2 with 〈EKE$_{hp}$〉 in box 2 (80°-100°E)

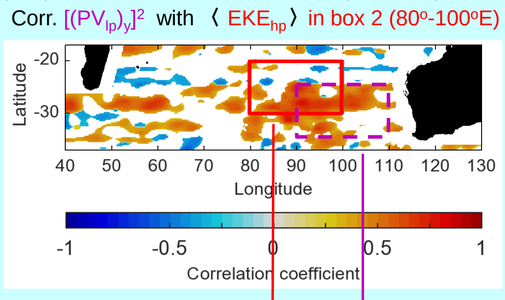

Interannual (periods > 14 months) time series of 〈EKE$_{hp}$〉 averaged in boxes 1 and 2, along with box-averaged 〈[(PV$_{lp}$)$_y$]^2〉

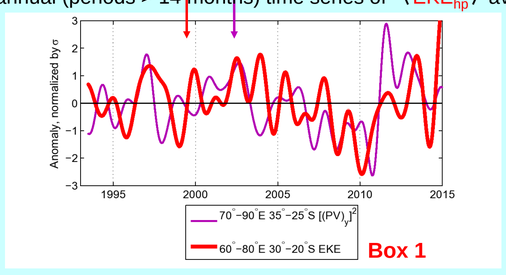

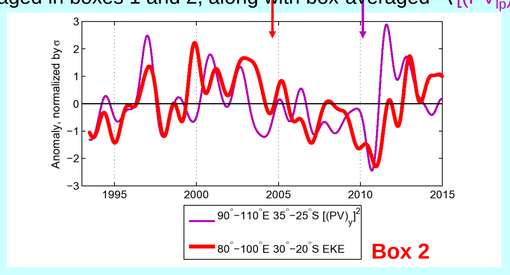

Note: Angle brackets 〈 〉 indicate that the quantity is spatially-averaged in a box to create a time series, prior to display or use in lagged correlations

Results: Remote forcing

- Atmosphere-ocean dynamics in the tropical Pacific may drive eddy activity in the SSIO, through Pacific wind forcing and planetary wave propagation (e.g., Potemra, 2001; Lee and McPhaden, 2008; Jia et al., 2011)
- In our analysis, the Niño3.4 index (based on equatorial Pacific sea surface temperatures) represents the coupled ocean-atmosphere state over the tropical Pacific; N Trop Pac and S Trop Pac represent two areas where planetary waves in the ocean are forced by Pacific wind stress curl

In what areas does wind forcing (remotely) affect SSIO eddy activity?

(right) Interannual (periods > 14 months) optimum correlations of 〈EKE$_{hp}$〉 in box 3 with wind stress curl.
Wind stress curl leads EKE by 0-24 months.

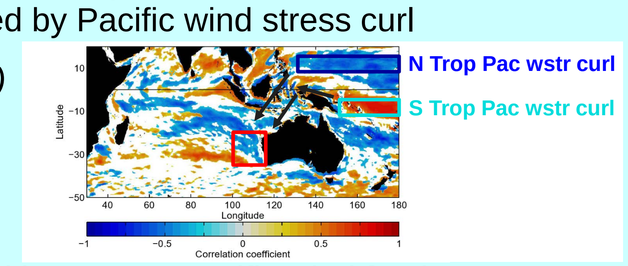

Where in the SSIO is eddy activity affected by remote Pacific wind forcing?

Optimum correlations 〈Niño3.4〉 - EKE$_{hp}$

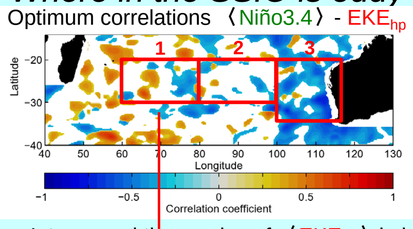

Opt. corr. 〈N Trop Pac wstr curl〉 - EKE$_{hp}$

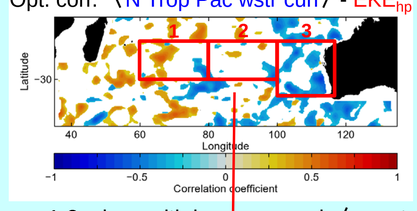

Opt. corr. 〈S Trop Pac wstr curl〉 - EKE$_{hp}$

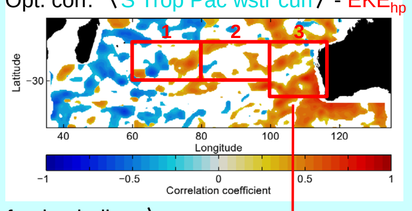

Interannual time series of 〈EKE$_{hp}$〉 in boxes 1-3, along with box-averaged 〈remote forcing indices〉

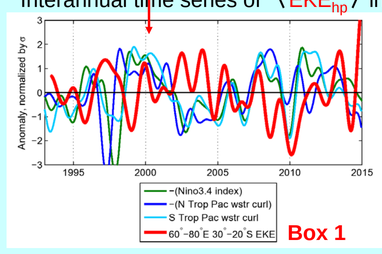

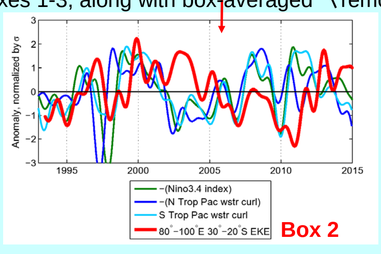

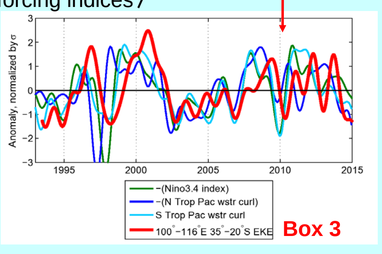

Conclusions & Future Work

- Local forcing: the variance of the potential vorticity gradient, an indicator of instability in the flow, may be useful for **predicting increases and decreases in SSIO eddy activity**
- Remote forcing: **El Niño/La Niña and tropical Pacific wind stress curl** induce changes in SSIO eddy activity, especially **near the eastern boundary**
- Next: consider effects of **high wavenumber/frequency wind energy input** on SSIO eddy activity, and study **eddy energy conversions** with an ocean GCM

National Aeronautics and Space Administration

Jet Propulsion Laboratory
California Institute of Technology
Pasadena, California

www.nasa.gov

References

- Charney, J. G., and M. E. Stern (1962), On the stability of internal baroclinic jets in a rotating atmosphere, *J. Atmos. Sci., 19,* 159-172.
- Jia, F., L. Wu, J. Lan, and B. Qiu (2011), Interannual modulation of eddy kinetic energy in the southeast Indian Ocean by Southern Annular Mode, *J. Geophys. Res., 116,* C02029.
- Lee, T., and M. J. McPhaden (2008), Decadal phase change in large-scale sea level and winds in the Indo-Pacific region at the end of the 20th century, *Geophys. Res. Lett., 35,* L01605.
- Potemra, J. T. (2001), Contribution of equatorial Pacific winds to southern tropical Indian Ocean Rossby waves, *J. Geophys. Res., 106,* 2407-2422.

This research was supported by an appointment to the NASA Postdoctoral Program at the Jet Propulsion Laboratory, administered by Universities Space Research Association under contract with NASA.

Poster No. EB-02

National Aeronautics and Space Administration

Towards an improved estimate of mountain glaciers contribution to sea level rise since 1972

Amaury Dehecq (329C), Alex Gardner (329C), Oleg Alexandrov (Ames Center)

Context

Glaciers contribution to sea-level change: Glaciers mass loss accounted for ~1/3 of the sea level rise since 1971 (IPCC). However, long term estimates of glacier mass change come with large uncertainties as they rely on sparse field observations prior to region-wide satellite observations that started in ~2000.

Hexagon satellites: The KH-9 series satellites, operated by the US National Reconnaissance Office (NRO), were placed in low Earth orbit (~170 km) between June 1971 and April 1986 (*Burnett*, 2012). They provided a global mapping capability with a 6-meter ground resolution frame camera (MCS) that collected nadir imagery with an overlap of 70% between adjacent images, enabling stereo reconstruction of topography. Declassification of the data in 2002 open new possibilities for better constraining glacier mass change over the last half decade (*Pieczonka et al.*, 2013; *Maurer et al.*, 2015).

Research Objectives:

- ✓ Develop an automated pipeline to generate Digital Elevation Models (DEM) at 24 m resolution from the scanned KH-9 positives.
- ✓ Compare historical DEMs with recent topography (e.g. ArcticDEM*) to estimate glaciers volume changes and contribution to sea level rise over the last 40 years.

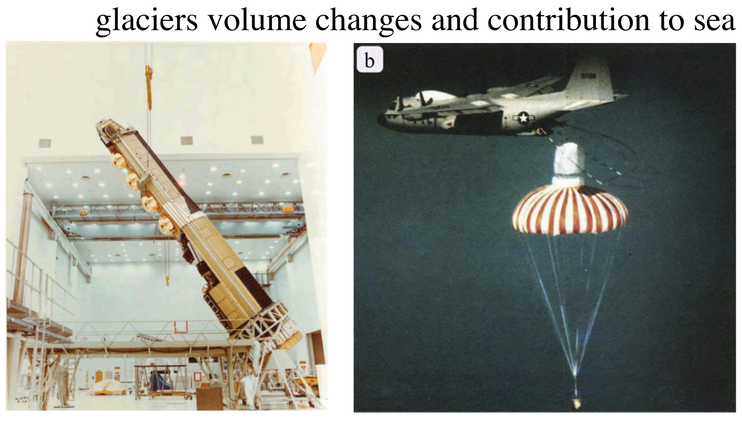

Fig. 1: KH-9 satellite. (Left) KH-9 vehicle during assembly. The canisters of exposed films (gold domes) were periodically ejected, deorbited and captured during descent by a special trained group within the airforce (right) (*Burnett at al.*, 2012)

Image preprocessing

Challenges: - Images stored on 18”x9” photographic films, scanned as two seven micron 9.5”x9” overlapping images.
- Storing/scanning caused distortion that must be corrected prior to the stereo processing.

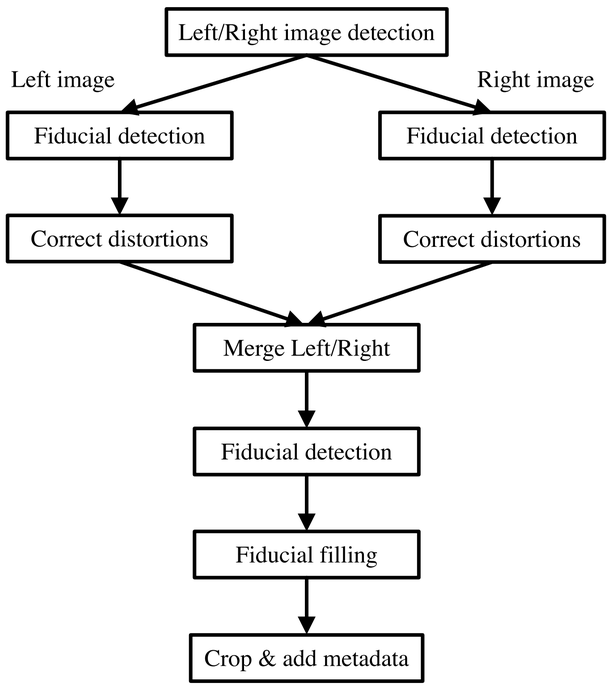

Fig. 2: KH-9 pre-processing workflow.

Correction of distortion: KH-9 images have 1058 fiduciary marks (crosses) identifying the original film geometry at the time of exposure (*Surazakov & Aizen*, 2010). Each fiducial is located with subpixel precision by convoluting a cross-like kernel and looking for local regular maxima. The distance of the cross centers to a regular grid yields the image distortion at the réseau grid. A thin-plate-spline interpolation is used to estimate and correct the distortion at each pixel.

Image stitching : The left/right scanned images are stitched together using feature-tracking technics to identify the exact area of overlap. The fiducials are located again on the full image and filled with white noise to avoid mismatches during the stereo processing. Finally the image is cropped to remove image borders.

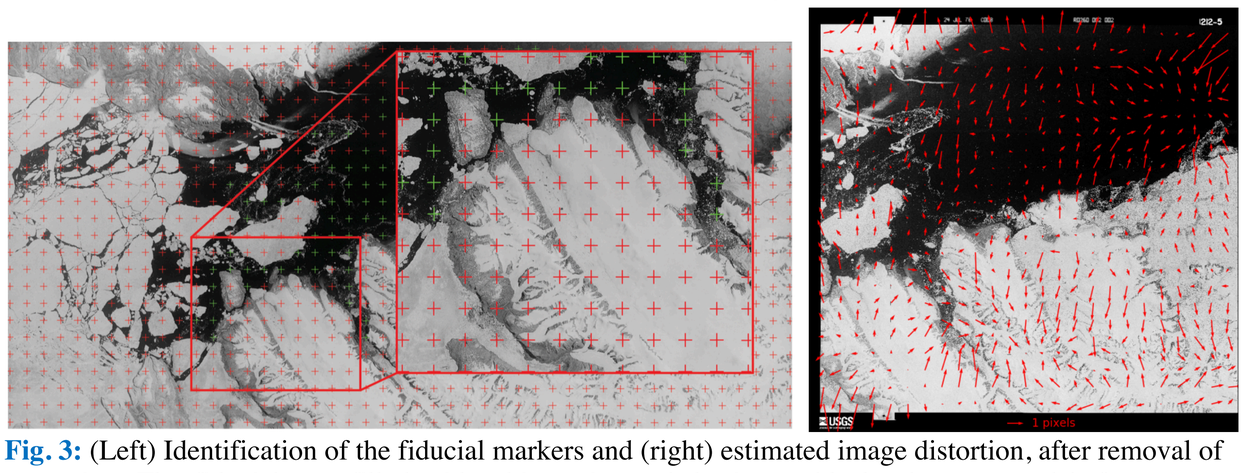

Fig. 3: (Left) Identification of the fiducial markers and (right) estimated image distortion, after removal of a rotation. The fiducials are filled with white noise and the image black edges cropped before stereo processing.

Stereo processing

Objective: The open-source AMES stereo pipeline (*Shean et al.*, 2016) is used to reconstruct topography from image pairs/triplets.

Challenges: - Images are crudely geolocated (no existing Ground Control Points)
- Precise satellite position is classified.

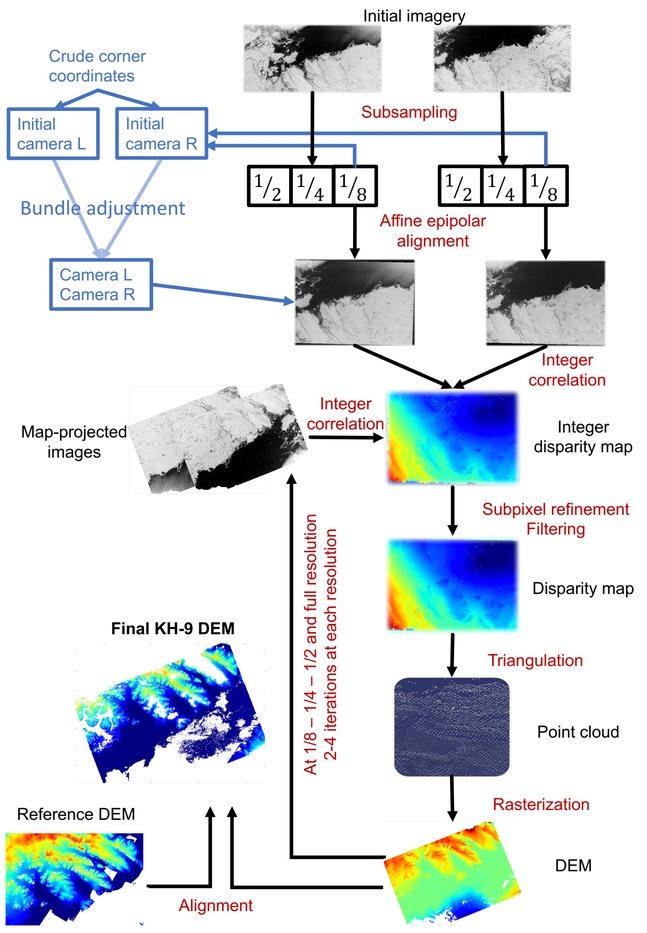

Fig. 4: Stereo processing workflow.

Solve for camera: - Pinhole camera model
- Camera intrinsic: focal length = 12”, optical center = center of réseau grid
- Camera extrinsic: (1) from crude corner coordinates provided by USGS, a camera position/orientation is estimated for each image, (2) bundle adjustment is used to ensure consistency in the position of automatically generated interest points in all images, (3) after alignment of the final DEM with a reference, the camera models can be further refined.

Stereo: - A disparity map is estimated between two images, using the Semi-Global Matching algorithm, with 7x7 pixels correlation windows.
- a point-cloud and DEM are generated from the disparity map using triangulation.
- Process is ran at 1/8 the resolution, to limit search range and memory usage. The output DEM is then used to map-project the images, reducing the disparity between the left/right image and improving the correlation. The process is repeated at ¼, ½ and full resolution.
- Final DEM is aligned with a reference DEM using Iterative Closest Point (ICP)

Preliminary results

Example of application to an image pair in the Canadian Arctic, acquired 24/07/1976. Off-ice elevation difference: **median = 2.5 m, standard deviation = 17.5 m**.

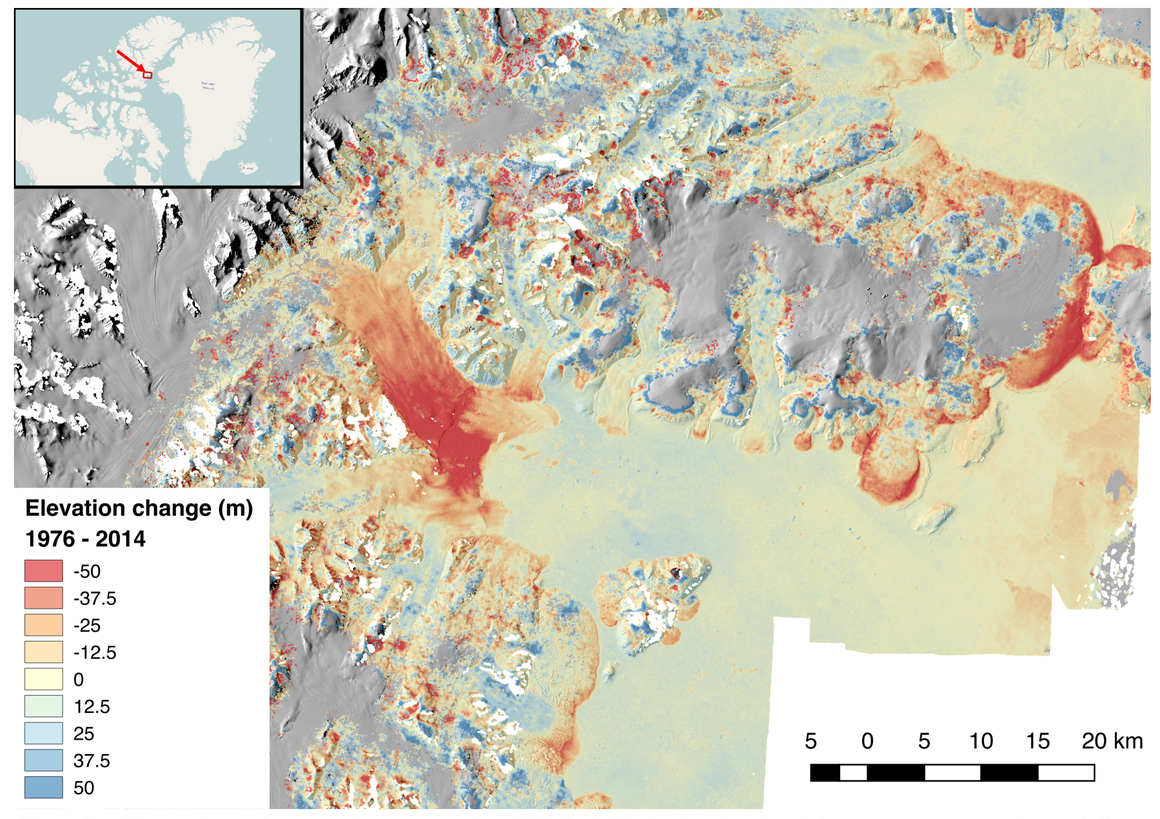

Fig. 5: Elevation change between the KH-9 DEM obtained with our automated workflow and ArcticDEM* (from WorldView imagery). The retreat and thinning of the tidewater glaciers Trinity and Sparks is clearly visible.

- ❖ We developed an automated preprocessing workflow able to convert the scanned imagery into undistorted digital images. To date >300 images have been pre-processed, with a global coverage of glaciers.
- ❖ A beta stereo processing workflow has been developed and is able to estimate unknown satellite positions and reconstruct historical topography with ~10-20 m accuracy.

References: Burnett, M. G. (2012), *Hexagon (KH-9) Mapping Camera Program and Evolution*, 364 pp., Center for the study of National Reconnaissance Chantilly, VA.
Maurer, J. & Rupper, S. Tapping into the Hexagon spy imagery database: A new automated pipeline for geomorphic change detection. *ISPRS Journal of Photogrammetry and Remote Sensing* **108,** 113–127 (2015).
Pieczonka, T., Bolch, T., Junfeng, W. & Shiyin, L. Heterogeneous mass loss of glaciers in the Aksu-Tarim Catchment (Central Tien Shan) revealed by 1976 KH-9 Hexagon and 2009 SPOT-5 stereo imagery. *Remote Sensing of Environment* **130,** 233–244 (2013).
Shean, D. E. *et al*. An automated, open-source pipeline for mass production of digital elevation models (DEMs) from very-high-resolution commercial stereo satellite imagery. *ISPRS Journal of Photogrammetry and Remote Sensing* **116,** 101–117 (2016).
Surazakov, A. & Aizen, V. Positional Accuracy Evaluation of Declassified Hexagon KH-9 Mapping Camera Imagery. *Photogrammetric Engineering & Remote Sensing* **76,** 603–608 (2010).
* *DEMs provided by the Polar Geospatial Center under NSF OPP awards 1043681, 1559691 and 1542736 - www.pgc.umn.edu/data/arcticdem/*

National Aeronautics and Space Administration
Jet Propulsion Laboratory
California Institute of Technology
Pasadena, California
www.nasa.gov

This research was carried out at the **Jet Propulsion Laboratory** and the **California Institute of Technology** under a contract with the **National Aeronautics and Space Administration** and funded through the **Caltech Postdoctoral** fellowship.

Poster No. EB-03

National Aeronautics and Space Administration

30-year synthesis of satellite and airborne altimetry records to resolve long-term ice sheet trends

Author: Johan Nilsson (329C)

Introduction

Satellite and airborne altimetry has since the early 1990's provides the longest continuous record for studying the geophysical processes of the ice sheets and their current contribution to sea level rise. However, this long-term record comprises of several different sensors, of different types, quality and resolution, providing a major challenge in the interpretation and reconstruction of consistent time series.

Previous multi-mission long-term studies have mainly used a cross-calibration methodology based on conventional crossover bias analysis to merging records from different sensors. This methodology is very precise but has a main disadvantage in the form of spatial coverage, restricting the usage of the method to regional or continental wide studies, with a spatial resolution on the order of 10-50 km.

In this presentation a novel assimilation framework will be presented for integrating heterogeneous altimetry records, using an adaptive least-squares minimization procedure. This merging procedure allows us to solve for inter-mission, spatial and temporal biases down to 1 km scales. It also allows us to account for difference in both data quality and sensor resolution to reconstruct robust long-term time series, enabling us to acquire a wealth of information on ice sheet wide processes at fine spatial and temporal scales.

Current Status and Future Work

- Currently in the process of merging all available space-borne altimeters: **ERS -1/2, Envisat, ICESat and CryoSat-2.**
- Validation and analysis of several general radar/laser altimetry corrections and generated time series.

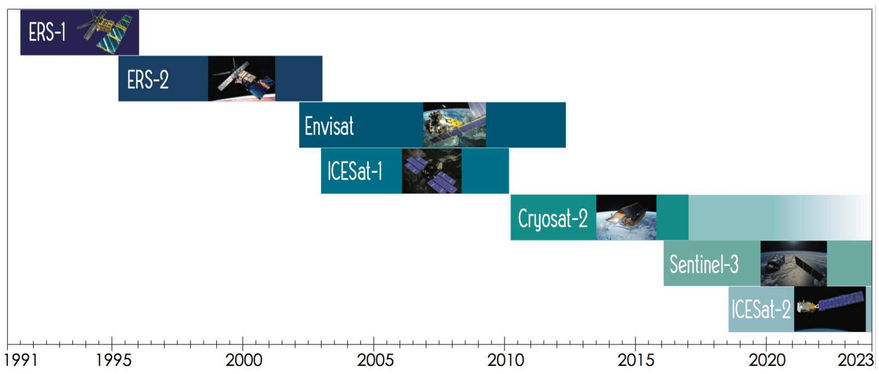

Figure 1: Radar and laser altimetry mission to be synthesized into a continuous 30 year record of ice sheet elevation change

- Implementation of a Kalman-smoother for filtering, interpolation and extrapolation of time series. (see examples below)

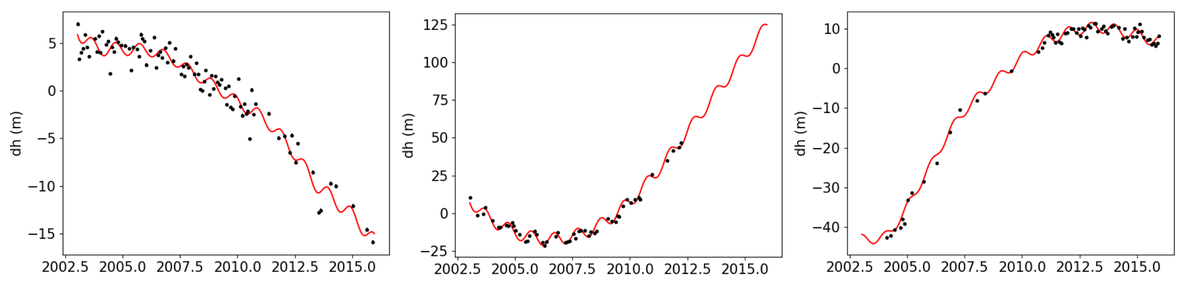

Figure 2: Processed time series (black) from the merging algorithm, which has been further processed using the Kalman-smoother (red).

Elevation Change (1991-2016)

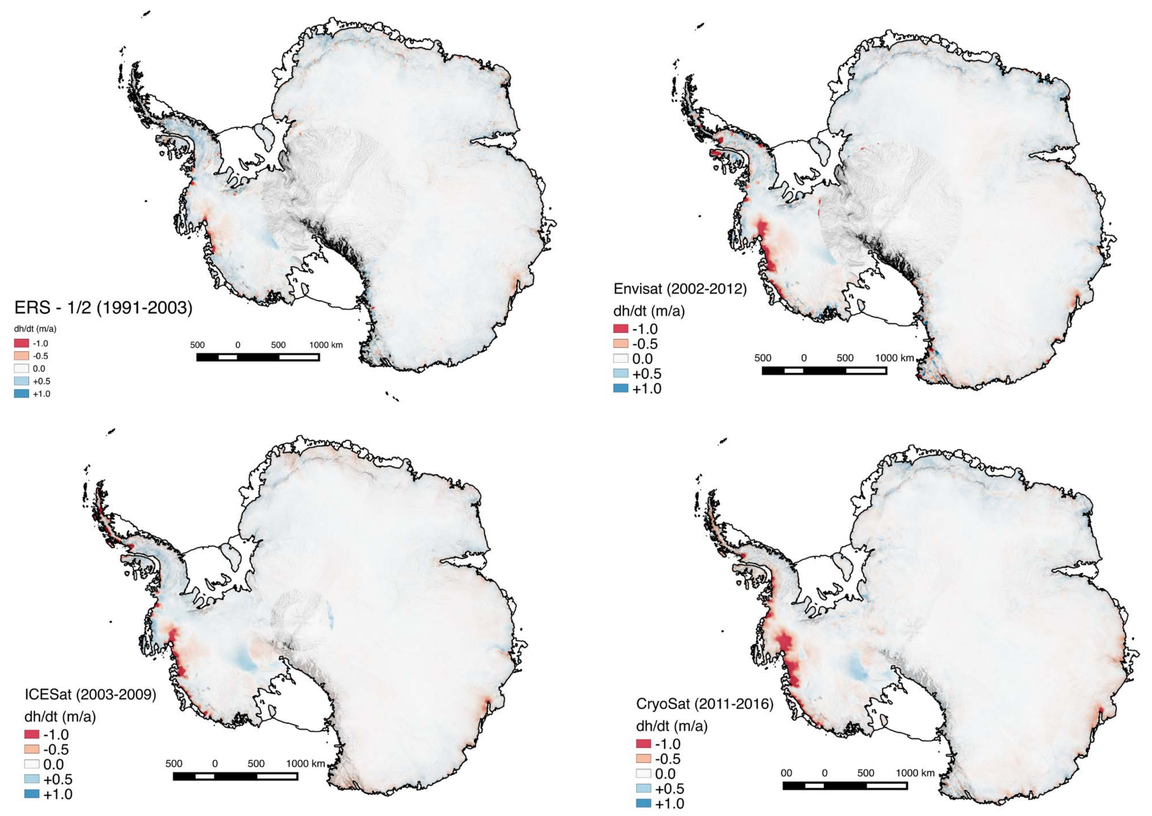

Figure 3: Individual linear elevation change rates from current (available) mission, which will be updated as new mission data becomes available

Merged Solution (2003-2016)

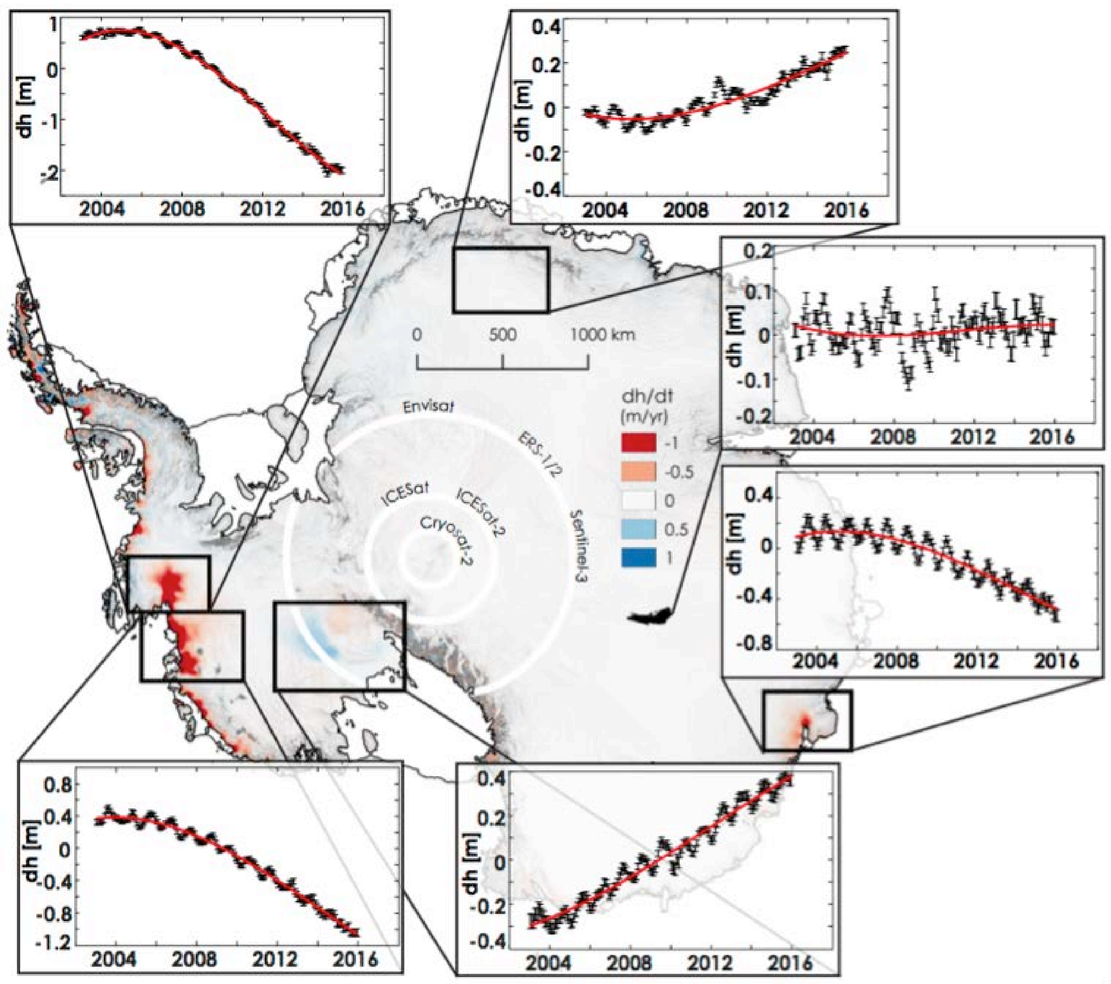

Figure 4: Initial results from a demonstration synthesis of Envisat, ICESat, and CryoSat-2 altimetry records processed using the proposed synthesis methodology. Monthly time series for boxes located over select glaciers are shown with respective errors. 3rd order polynomial fits shown in red.

National Aeronautics and Space Administration

Jet Propulsion Laboratory
California Institute of Technology
Pasadena, California

www.nasa.gov

Poster No. EB-04

National Aeronautics and Space Administration

Browsing through the last glacial cycle history scenarii: a necessary milestone to build up our understanding of present-day climate change

Author: Lambert Caron (329-C)
Erik Ivins, Eric Larour and Surendra Adhikari (329-C)

What is Glacial Isostatic Adjustment?

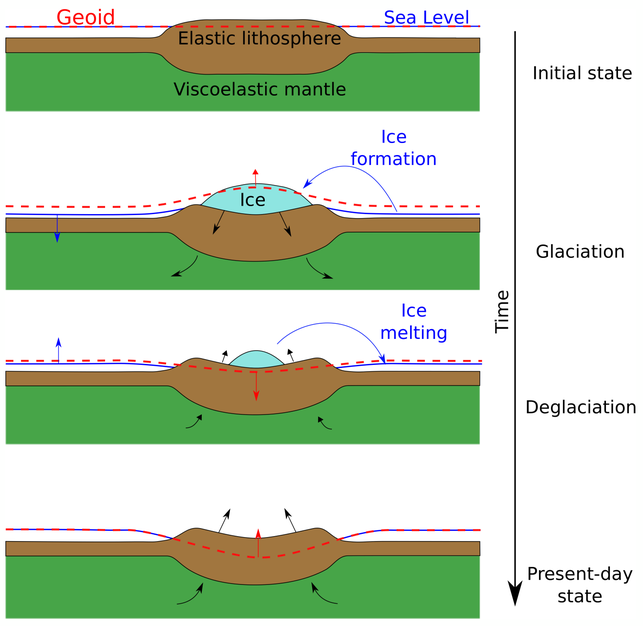

Why does it matter?

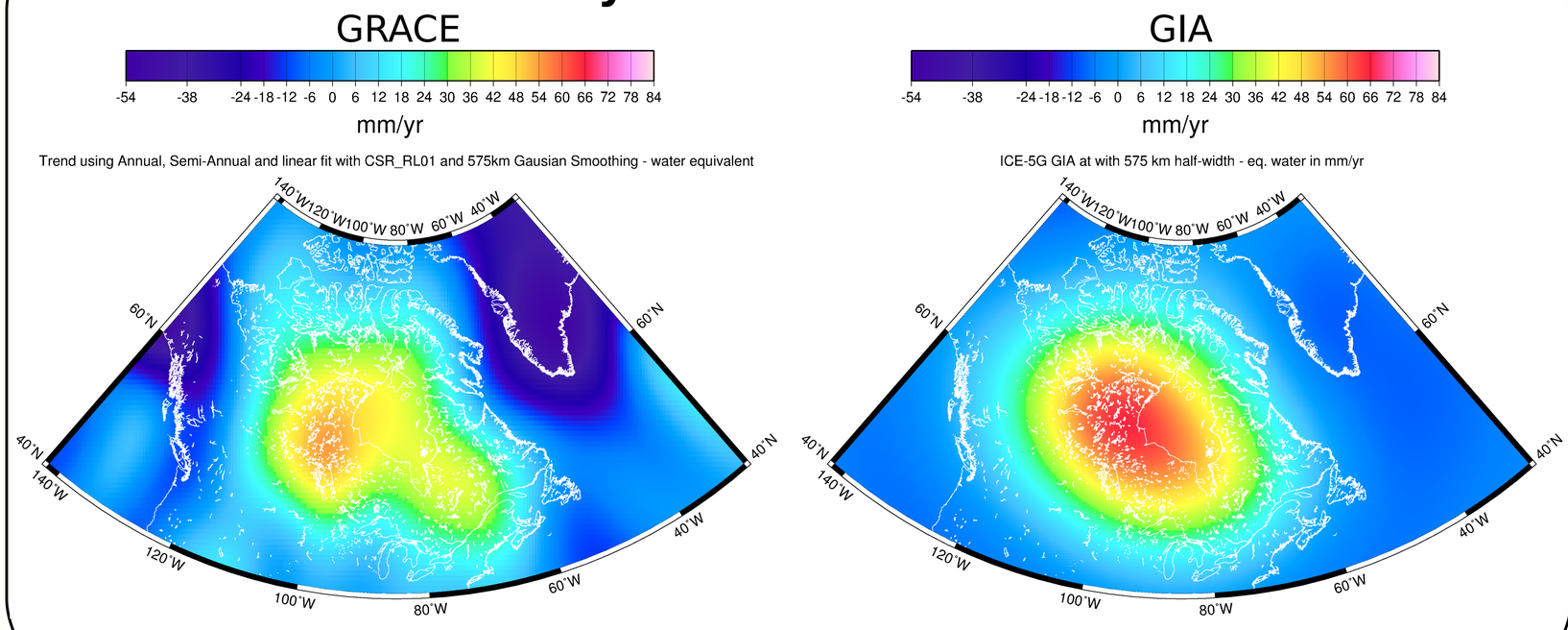

Constraining data: Relative Sea Level and GPS

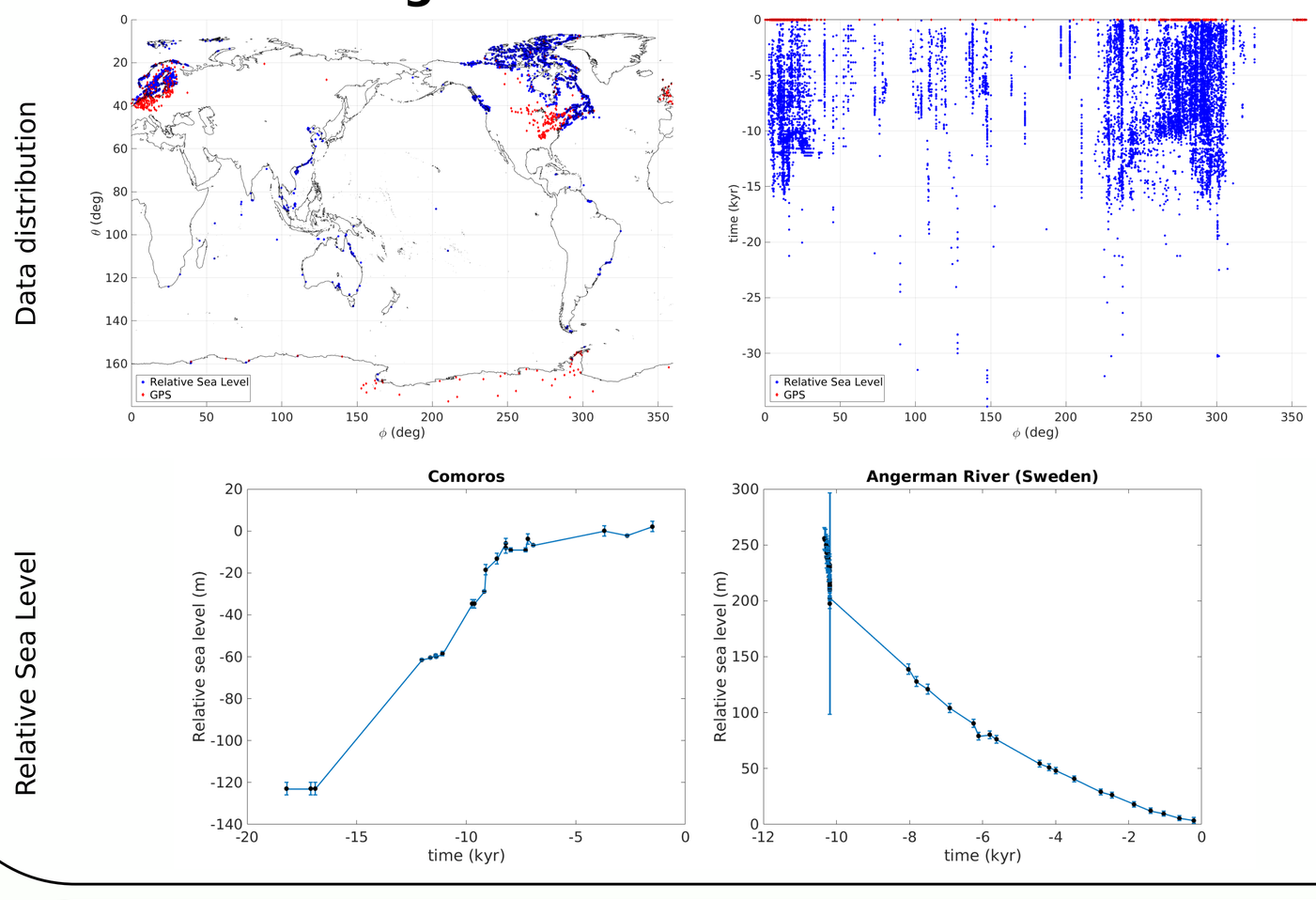

Bayesian inversion

$$p_i = exp\left(-\frac{1}{2N}(\mathbf{data}-\mathbf{model_i})^T\mathbf{\Sigma}^{-1}(\mathbf{data}-\mathbf{model_i})\right)$$

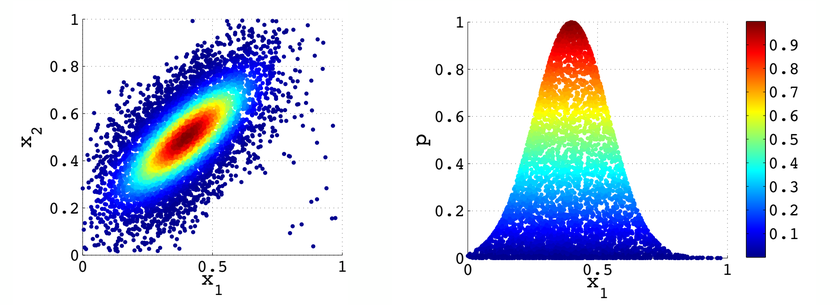

Earth rheology

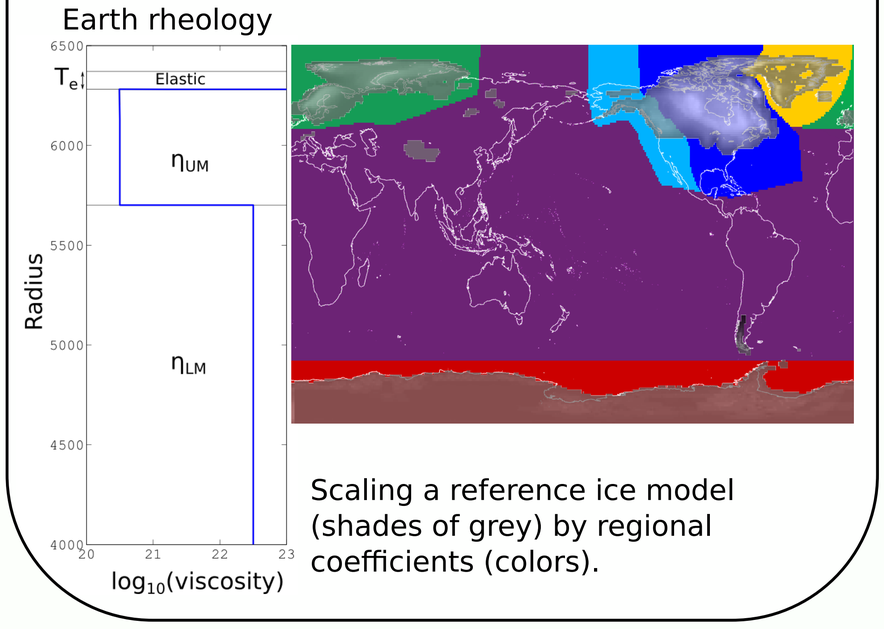

Scaling a reference ice model (shades of grey) by regional coefficients (colors).

Present-day predictions

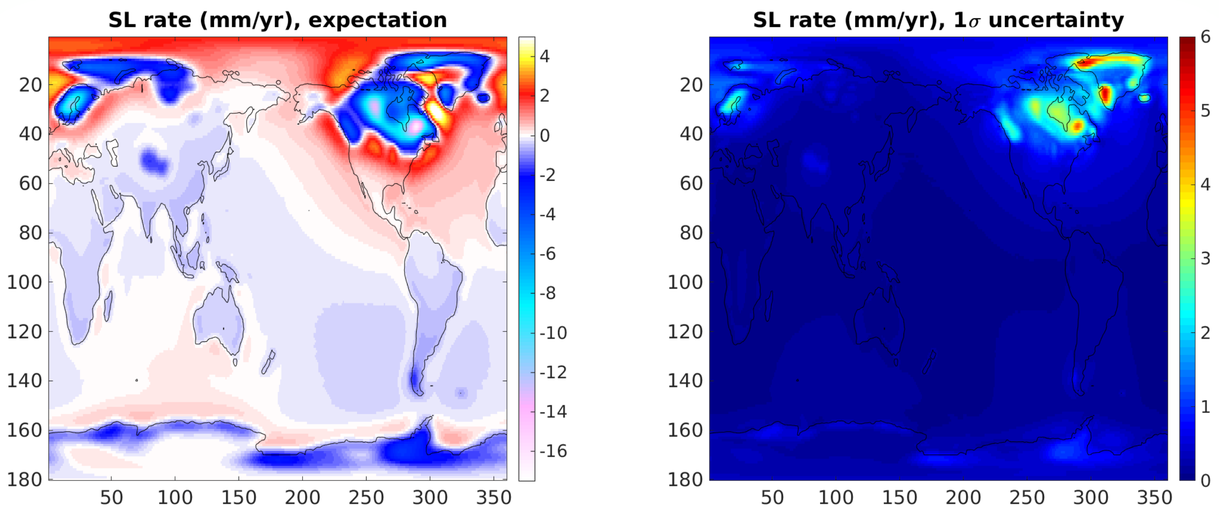

Goals & Impacts

- Getting out of the single best model philosophy
- Formal GIA uncertainty
- Hydrology (GRACE)
- Ocean Altimetry (SWOT, JASON)
- Sea level projections

National Aeronautics and Space Administration

Jet Propulsion Laboratory
California Institute of Technology
Pasadena, California

www.nasa.gov

Poster No. EB-06

National Aeronautics and Space Administration

Origin of Circumpolar Deep Water intruding onto the Amundsen and Bellingshausen Sea continental shelves

Author: Yoshihiro Nakayama (329C)
Dimitris Menemenlis (329C), Michael Schodlok (329C), Eric Rignot (3340)

1. Why Amundsen and Bellingshausen Seas?

- Warm CDW (Circumpolar Deep Water) → Ice shelf thinning → Speed up ice flow → Grounded ice loss → Sea level rise
- Increased melt in AS → Freshening locally and downstream → Thermohaline circulation weakening

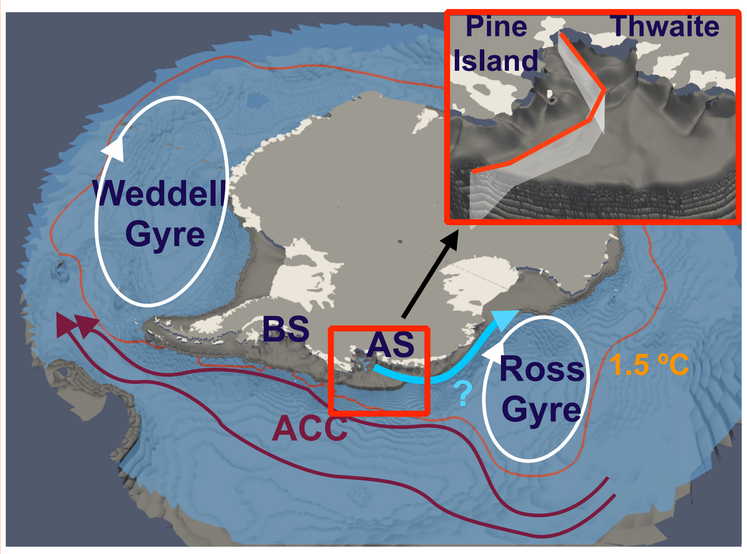

Key Questions

- What are the pathways of CDW intruding onto the Amundsen Sea (AS) and Bellingshausen Sea (BS) continental shelves ?
- What physical processes influence the pathway and properties of CDW intruding onto the AS and BS continental shelves ?

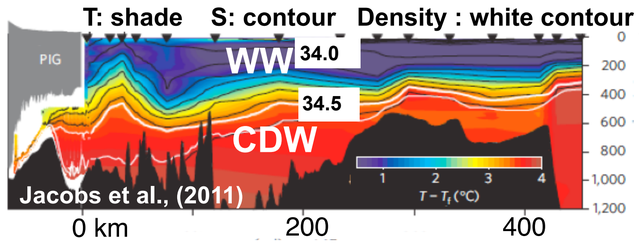

Ross Sea Freshening

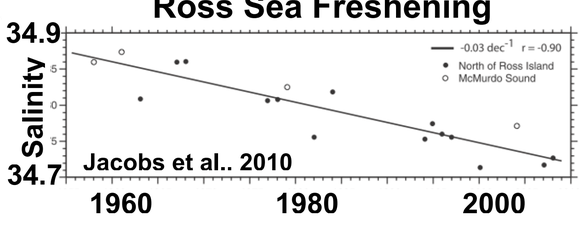

2. MITgcm regional AS/BS configuration

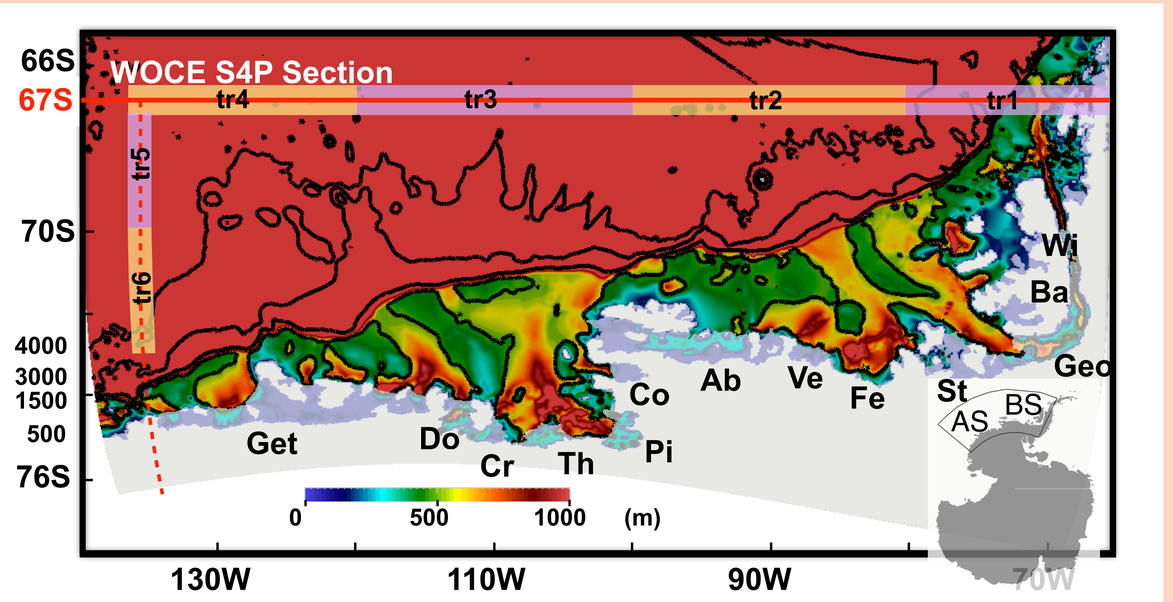

- **Tracers representing CDW are initially released from purple and orange boxes with potential density of 27.60-27.80 near northern and eastern boundaries of the model domain.**
- Initial condition from WOA 2013, boundary conditions from Estimating the Circulation and Climate of the Ocean (ECCO), bathymetry from IBSCO, and ice shelf draft from BEDMAP.
- 5-year simulations (**2001-2006** and **2009-2014**) with ECCO optimized atmospheric forcing.
- Horizontal grid spacing of 2-3 km and 50 vertical levels.
- Heat and salt transfer coefficients for ice shelf-ocean boundary are adjusted for the estimates of ice shelf melt rates (Rignot et al., 2013), as is done in Nakayama et al., 2017.
- Simulated vertical section of monthly mean potential temperature in January 2011 along 66.67ºS qualitatively agrees with observed vertical section (S4P) at the same time.

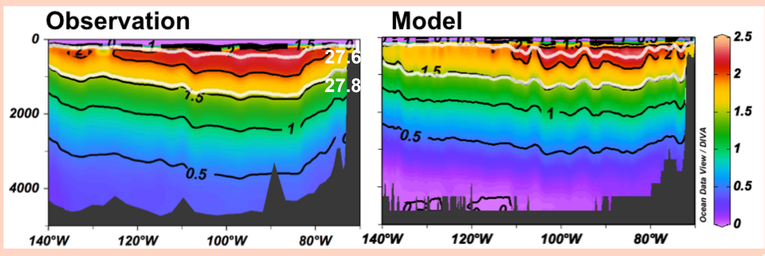

3. Pathway of CDW towards AS and BS shelves

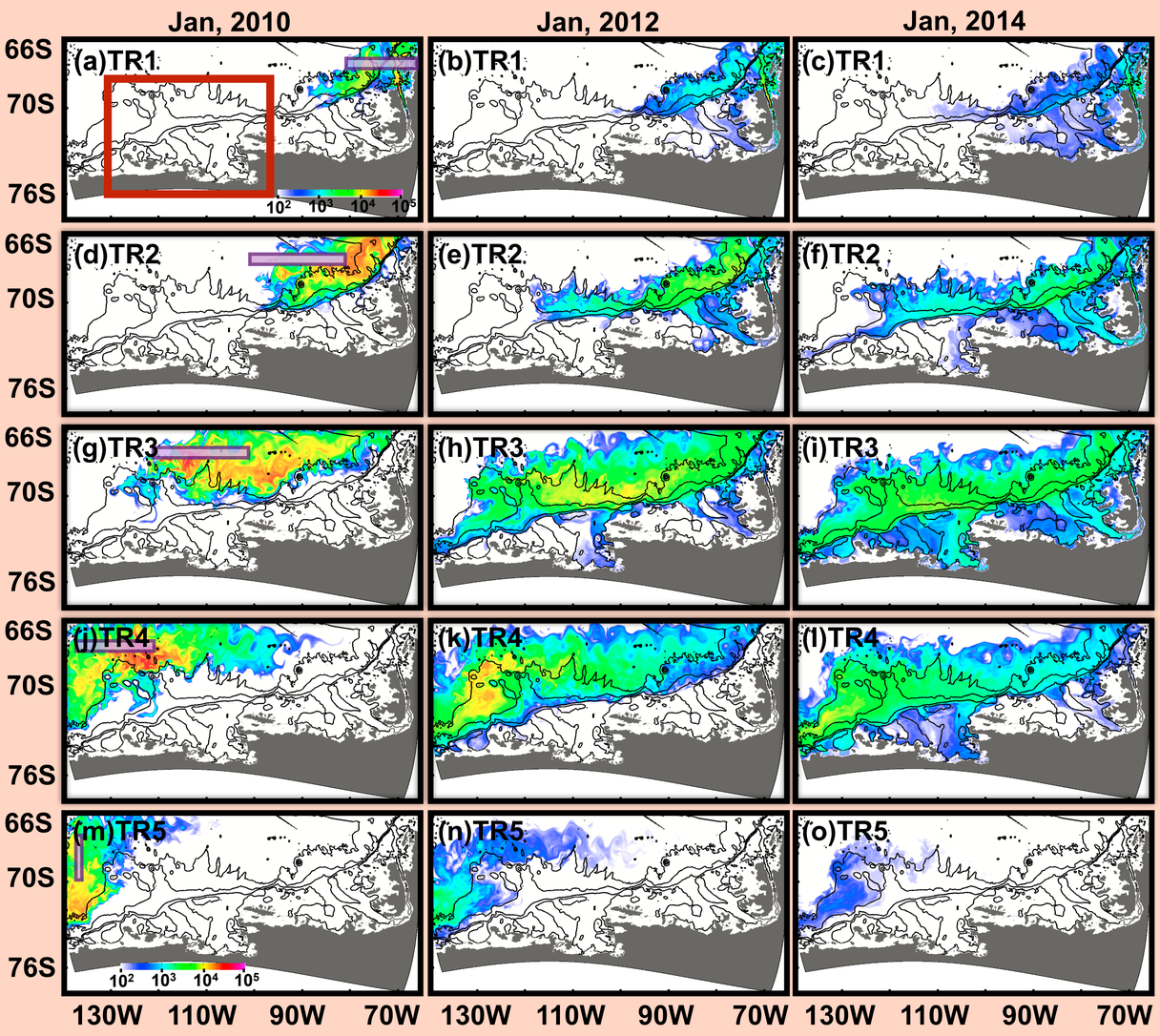

- Largest amount of CDW intruding onto the AS and BS continental shelves originates from the 120º-100ºW and 100º-80ºW of S4P (along 67ºS) section, respectively.
- It takes 3-5 years for the CDW tracer to reach AS and BS continental shelves from S4P section.

4. What controls the pathway of CDW ?

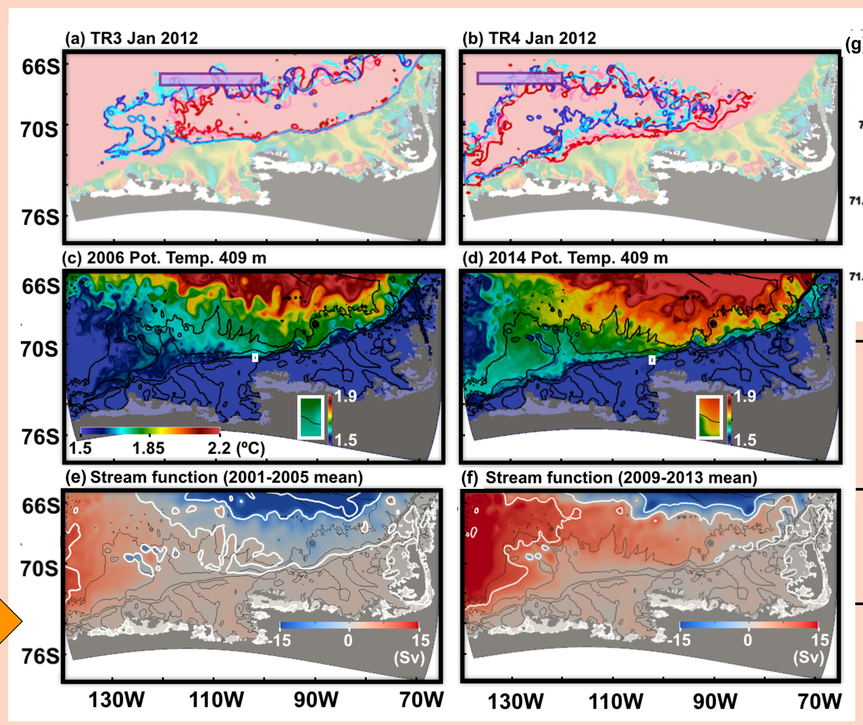

- CDW tracer is transported more eastwards in 2009-2014 case (blue) than in 2001-2005 case (red).
- Warmer CDW is present off the AS continental shelf break in 2014 than in 2006.
- 2009-2014 case shows stronger and larger Ross Gyre (>20 Sv) than in 2001-2005 case (~10 Sv).
- Model shows a potential temperature increase by ~0.2ºC off the AS continental shelf (white box) comparing 2006 and 2014. Repeated CTD observations show a similar temperature increase.

5. Summary and Outlook

CDW pathway in the Pacific Sector of the Southern Ocean (specifically pathway from S4P section to the AS and BS continental shelves) **has been investigated for the first time using eddy admitting (2-3 km) simulation of AS/BS domain.**

Model results show that model boundary conditions (and thus large scale wind forcing and water mass formation) **controls the strength of Ross Gyre and thus modulating the pathway as well as water mass characteristics of CDW off the AS and BS continental shelves.**

Physical understanding of processes controlling the basal melt rates of ice shelves in the AS/BS will enable improved projections of sea level change.

Poster No. EB-07

National Aeronautics and Space Administration

Sensitivity of marine-terminating glaciers on the West Antarctic Peninsula to global atmosphere-ocean forcing

Authors: Catherine C. Walker (329C) and Alex S. Gardner (329C)

Antarctic ice-ocean interaction:

Most of Antarctica's ice streams and glaciers end at the ocean, either as floating ice shelves or as marine-terminating glaciers. These oceanic margins exhibit the most rapid change. Warm waters can infiltrate the continental shelf, and melt the ice at depth from below. This can lead to an increase in flow of grounded inland ice towards the oceans. Warm, salty Circumpolar Deep Water (CDW) is the largest water mass by volume in the Antarctic Circumpolar Current (ACC).

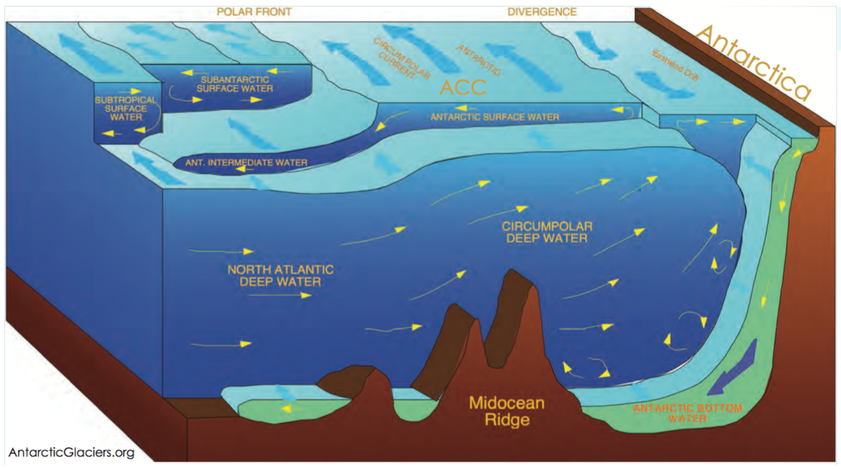

The dominating influence of winds:

- Winds over the ocean exert stress
- Wind stress induces currents in the ocean's upper layers
- Vertical transport replaces/removes water; degree of vertical transport (Ekman transport) is proportional to the curl of the wind stress
- Westerly winds around Antarctica intensify during positive phases of the Southern Annular Mode (SAM).
- During La Niña periods (-ENSO), winds are ~from the north over the west Antarctic Peninsula (WAP).
- Paired +SAM and –ENSO phases result in a cyclonic wind pattern at the WAP.

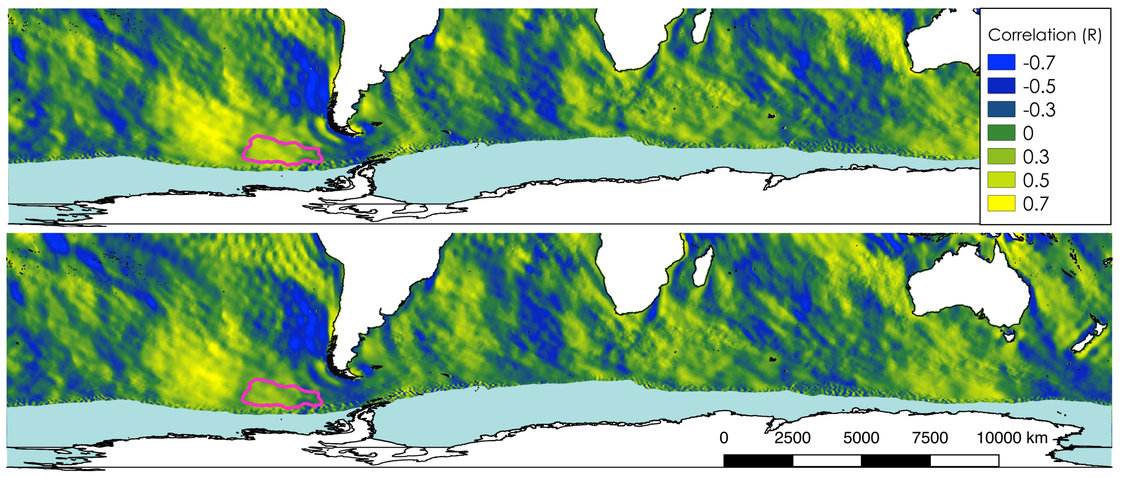

1993-2014 correlation of global atmospheric patterns (Top: SAM; Bottom: ENSO-SAM) to wind stress curl in the Southern Hemisphere using the ECCO2 model. Pink outline shows the area over which parameters are averaged in this study. Light blue shows average sea ice extent 1993-2014.

The former Wordie Ice Shelf (WIS) was set in the largest bay on the WAP, Marguerite Bay. The ACC (blue contours, below) flows right along the continental shelf break at the WAP, unique among other Antarctic coastlines.

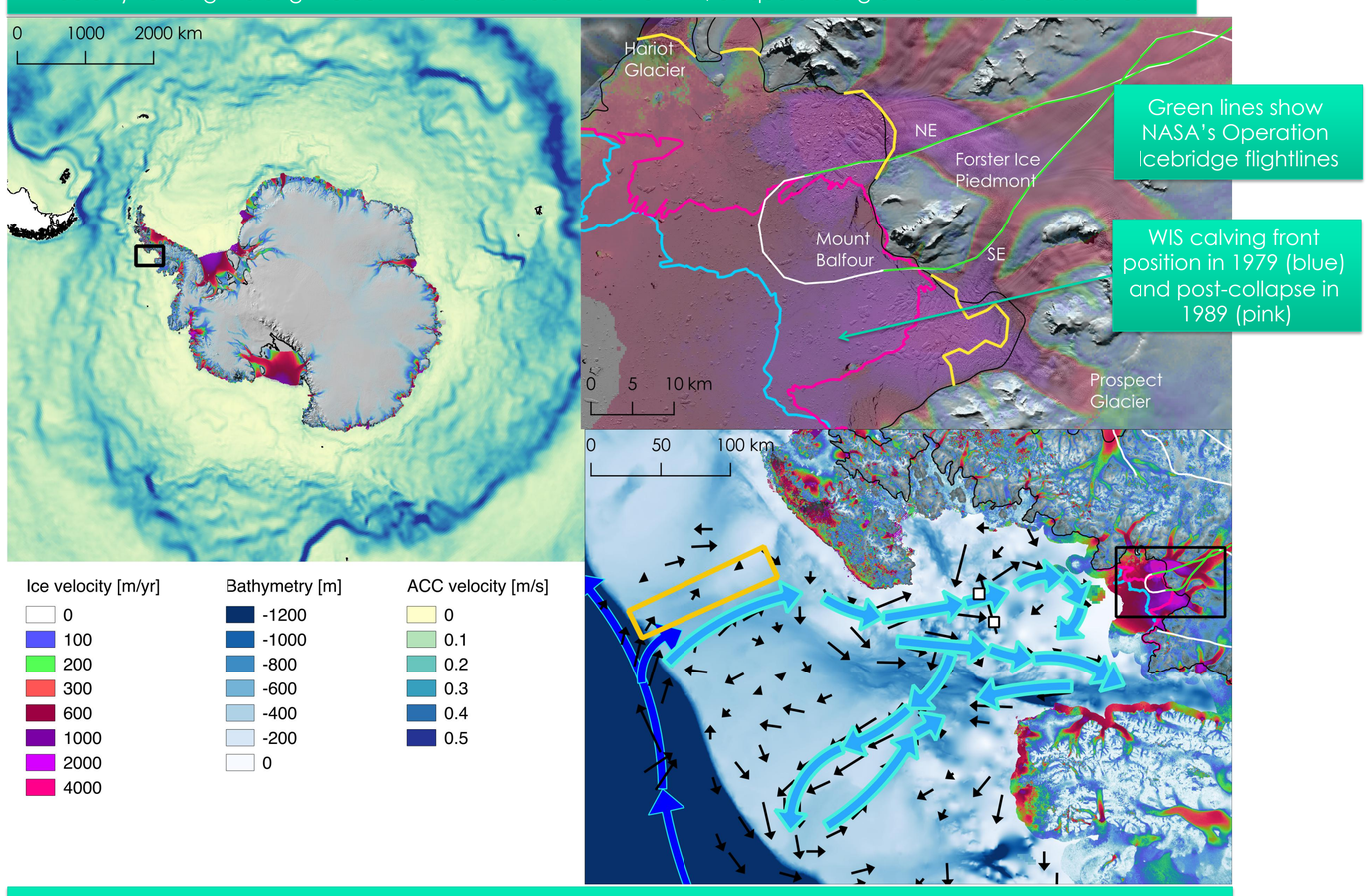

Black and blue arrows show on-shelf ocean currents in the bay; shades of blue show deep bathymetry on the shelf. Yellow box shows locations of in-situ oceanographic measurements. Black box outlines zoomed region, expanded at top right. Shades of purple show velocities derived from Landsat image pairs (Gardner et al. 2017)

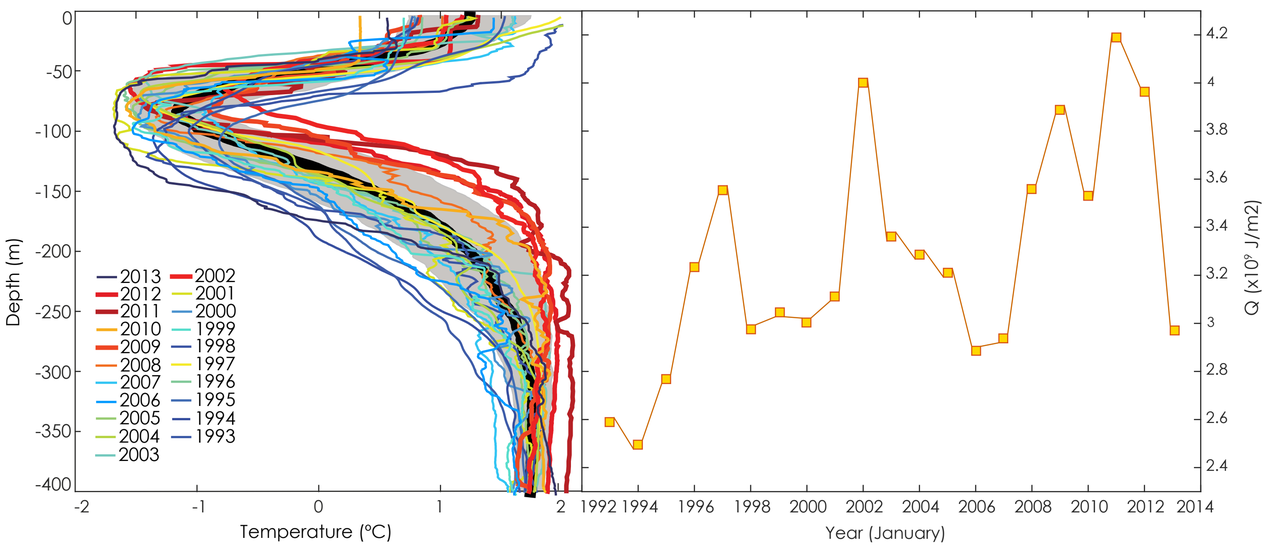

Left: CTD profiles from Marguerite Bay (location in yellow box; data courtesy of the Palmer Station LTER program)
Right: Total heat content of the ocean water available to melt ice in Marguerite Bay, 1993-2013

- Rapid speedup and coincident drawdown of multiple tidewater glaciers with change concentrated at glacier fronts is indicative of ocean forcing
- CTD measurements show warmest ocean waters in Marguerite Bay occurred 2002, 2008-2012, consistent with the timing of the glacier drawdown.

Evidence of dynamic glacier thinning at Marguerite Bay

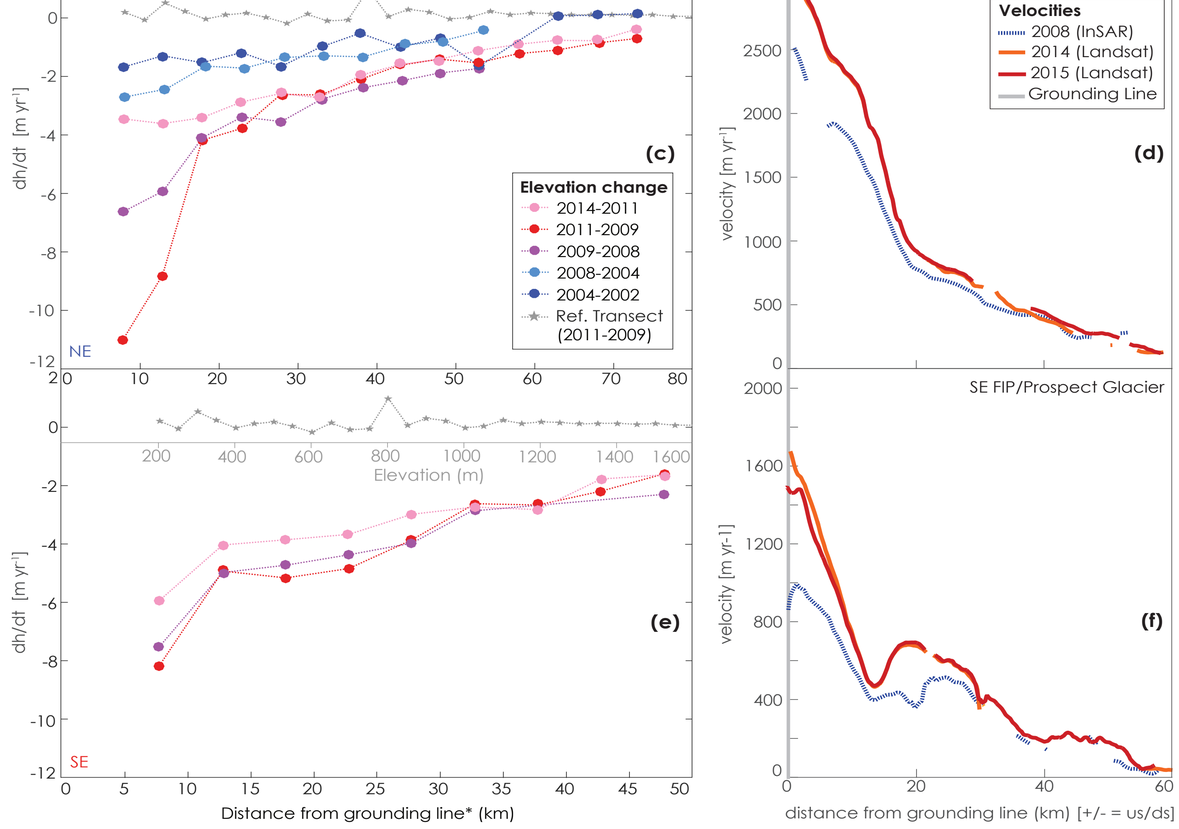

Left: Airborne laser altimetry from Operation Icebridge (ATM) between 2002-2014 shows massive elevation change signal over WIS glaciers, particularly between 2009-2011

Right: Velocities from Gardner et al. (2017) show large speedup near the grounding line. ***This was the largest speedup in all of Antarctica 2008-2014.***

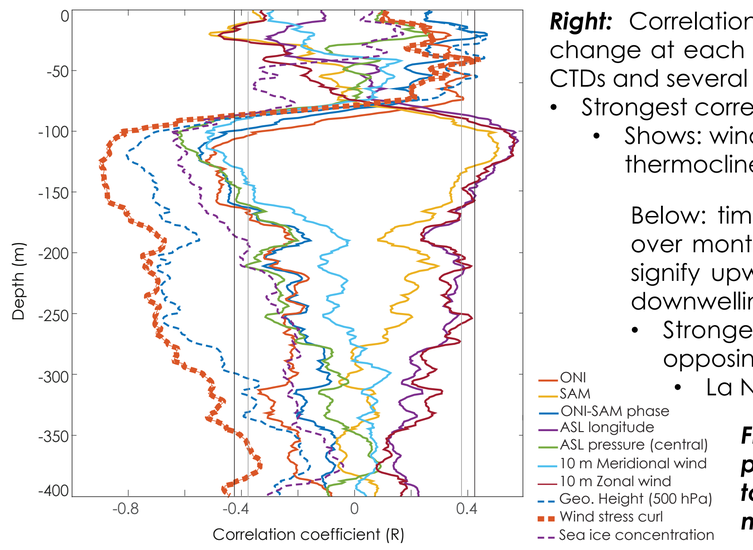

Right: Correlations between time series' of temperature change at each meter of depth measured by Palmer LTER CTDs and several oceanic/atmospheric parameters.

- Strongest correlation: wind stress curl below 100 m depth
  - Shows: wind stress curl accounts for ~81% variability in thermocline depth between 1993-2014.

Below: time series of ENSO (blue) and SAM (green) over monthly averages of wind stress curl. Red bars signify upwelling (-wind stress curl), blue bars signify downwelling (+wind stress curl).

- Strongest upwelling occurs during periods of opposing ENSO/SAM phases
  - La Niña and +SAM = upwelling

Finding: In-phase La Niña/+SAM led to wind patterns that brought increased ocean heat to Marguerite Bay 2008-2012, which led to massive glacier drawdown!

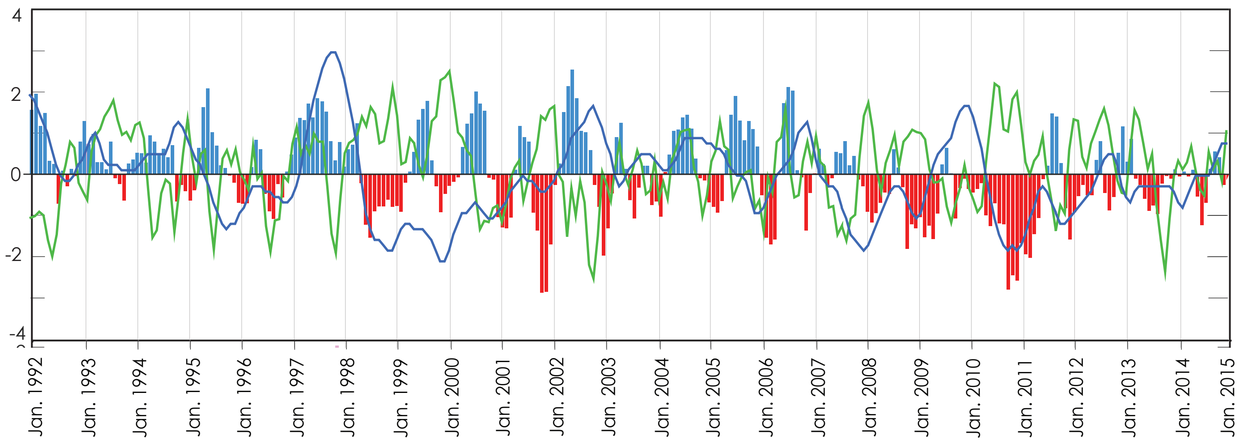

Poster No. EB-08

National Aeronautics and Space Administration

Jet Propulsion Laboratory
California Institute of Technology
Pasadena, California

www.nasa.gov

References: 1) Hyatt et al. (2011), *Top. St. in Oceanog.*, 58, 1553-1568. (2) Klinck et al. (2004), *Deep Sea Res. II*, 51, 1925-1946. (1) Orsi et al. (1995), *Deep Sea Res. I*, 42, 641-673. (4) St.-Laurent et al. (2012), *J. Phys. Oceanog.*, 43, 51-64. (5) Doake & Vaughan (1991), *Nature*, 350, 328-330. (6) Ferrigno et al. (2008), *Report No. 2600B.* (7) Rignot et al. (2005), *GRL*, 32. (8) Wendt et al. (2010), *Ann. Glac.*, 51, 97-102. (9) Rignot et al. (2011), *Science*, 333, 1427-1430. (10) Gardner et al., in press, TCD. (11) Huss & Farinotti (2014), *TC*, 8, 1261-1273. (12) Depoorter et al. (2013), *Nature*, 502, 89-92.

National Aeronautics and Space Administration

Spatial and Seasonal Distribution of Internal Gravity Waves and Balanced Motions in the Global Ocean

Hector S. Torres (329C-Caltech)
Dimitris Menemenlis (329C), Patrice Klein (329C) and Jinbo Wang (329B)

1. Introduction

Recent high-resolution simulations (1/30º , **1/48º resolution Fig. 1**) have led to a new vision of ocean dynamics on global scale that highlights the importance of oceanic motions < 50 km. These results have accelerated the development of a new generation of satellite altimeters. But one issue is the internal gravity waves (IGWs) impact on different oceanographic quantities, i.e., SSH, KE, SST.

This issue is addressed using a unique groundbreaking high-resolution simulation. **The goal is to better understand the spatial and seasonal distributions of IGWs and those motions in geostrophic or gradient-wind balance (balanced motions) in the global ocean.**

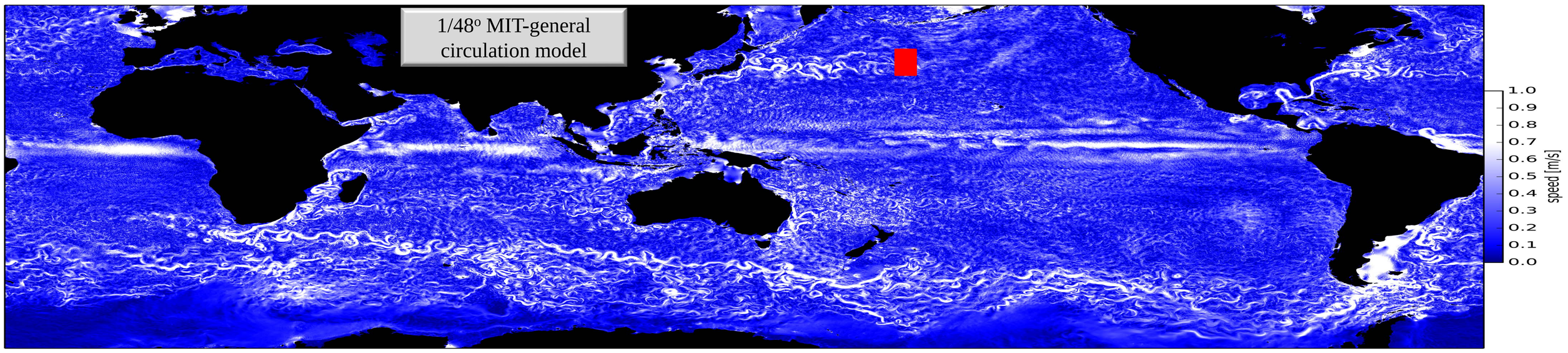

2. Methodology

- The global ocean simulation was divided into 3D (x, y, time) boxes with dimensions of 6º x 6º and 90-days
- Those boxes with depths less than 200 m were excluded
- The isotropic frequency-wavenumber spectra was computed at each box (Fig. 2)

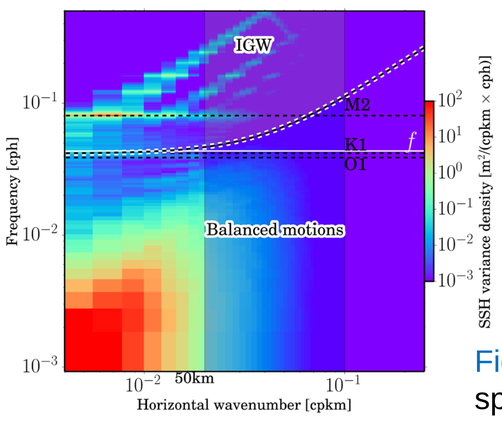

- M2 is the semidiurnal tide
- O1 and K1 are the main diurnal tides
- *f* is the local inertial frequency.

Fig. 2. Frequency-wavenumber spectra of SSH.

The dispersion relation of IGWs:

$$\omega^2 = f^2\left(1 + K\frac{N^2}{f^2 m^2}\right),$$

where ω is the frequency, f is the local inertial frequency, $K = \sqrt{k^2 + l^2}$, and m is the vertical component of the wavenumber vector.

➢The dispersion relation can be used as a dynamical filter (see white dashed line in Fig. 2).

4. Frequency-Wavenumber spectra

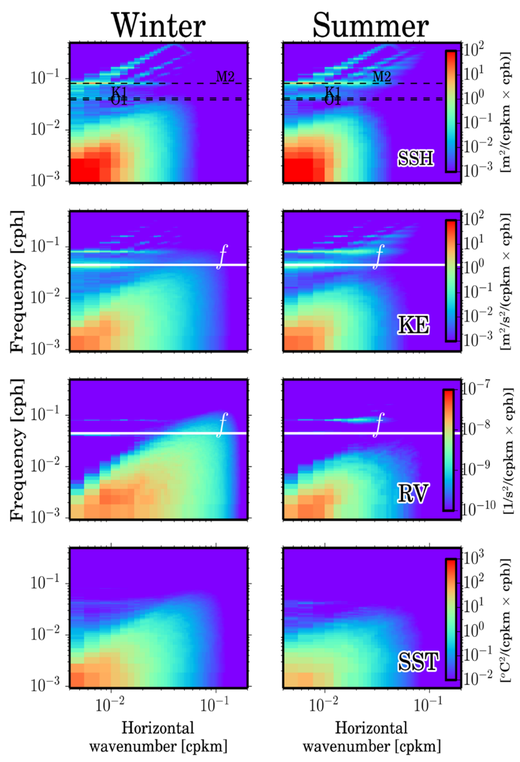

Fig. 3. Frequency-wavenumber spectra for SSH, KE, relative vorticity (RV), and sea surface temperature (SST). Red box in Fig. 1.

Seasonal variability:

➢Balanced motions stronger in winter

➢IGWs stronger in summer

➢Less impact of IGWs on RV and SST!

4. Geographical and seasonal variability

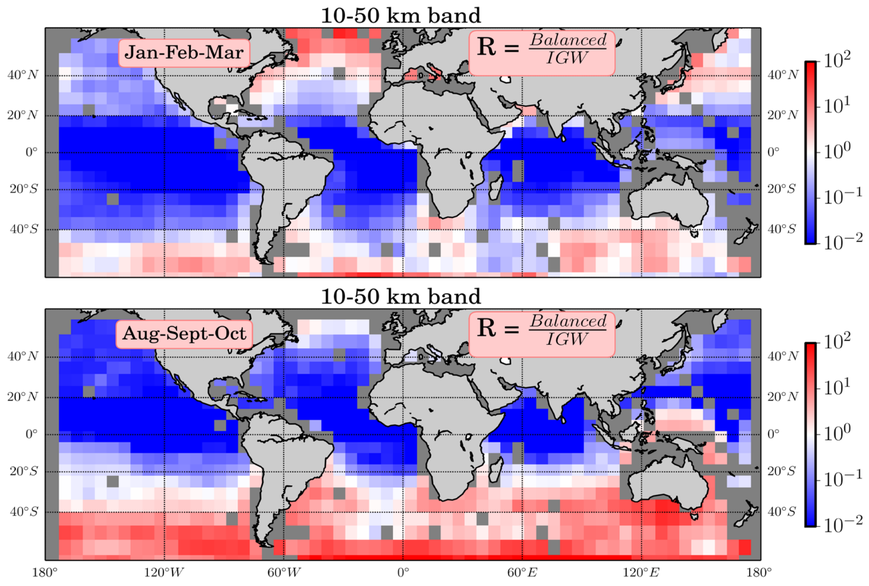

R > 1 → Dominated by balanced motions (red)

R =1 → Equally partition (white)

R < 1 → Dominated by IGWs (blue)

➢Strong diversity of IGWs and balanced motions

➢Strong impact of IGWs in summer, in particular in the Northern Hemisphere

Fig. 4. Geographical variability of R for SSH: Jan-Feb-Mar (top panel), Aug-Sept-Oct (lower panel).

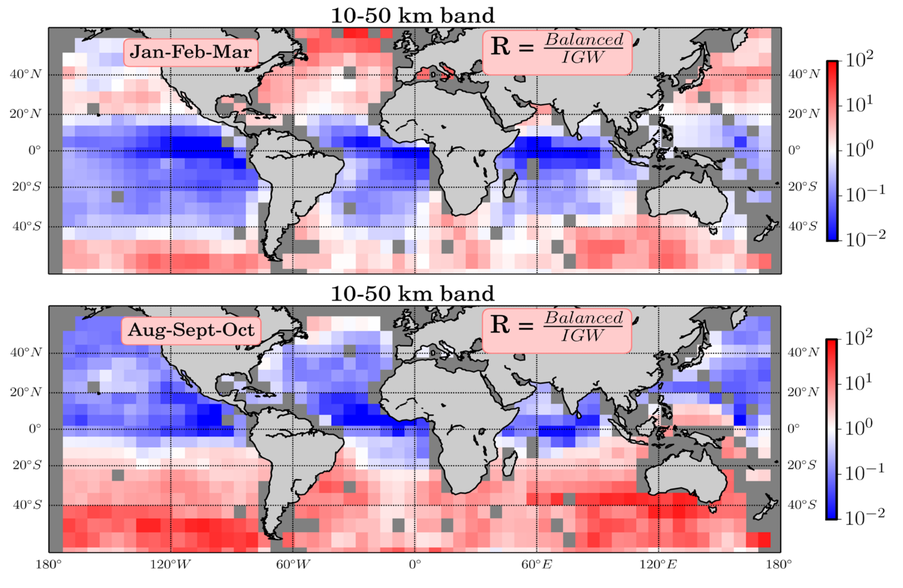

Fig. 5. Geographical variability of R for KE: Jan-Feb-Mar (top panel), Aug-Sept-Oct (lower panel).

5. Benefits for JPL

The work performed here helps to better know the potential of future and existing satellite sensors and how to use its observations in combination with others to have contemporaneous, global, measurements of total surface currents.

6. Acknowledgments

This research was carried out at the Jet Propulsion Laboratory, California Institute of Technology under a contract with NASA and funded through the NASA Ocean Vector Wind Science TEAM (OVWST), DopplerScat project.

Contact:
Hector.Torres.Gutierrez@jpl.nasa.gov

Poster No. EB-09

National Aeronautics and Space Administration

Jet Propulsion Laboratory
California Institute of Technology
Pasadena, California

www.nasa.gov

National Aeronautics and Space Administration
Jet Propulsion Laboratory
California Institute of Technology
Pasadena, California
www.nasa.gov

National Aeronautics and Space Administration

How Well the Early 2017 California Atmospheric River Precipitation Events Were Captured by Satellite Products and Ground-based Radars?

Author: Yixin 'Berry' Wen (329E)
Ali Behrangi (329E) and Bjorn Lambrigtsen (329E)

1. Excessive Rainfall in California in early 2017

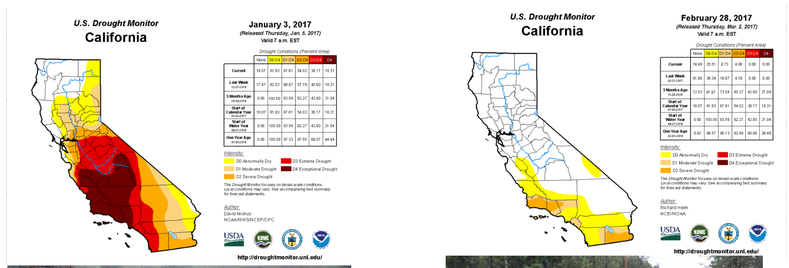

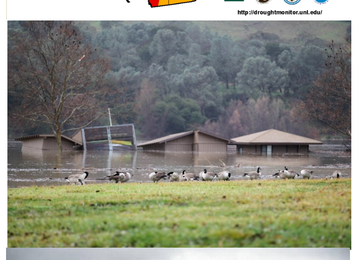

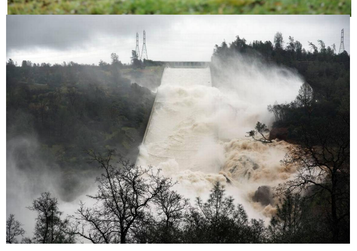

Water rushing down the danmaged Oroville Dam spillway breaches the concrete sides and spreads out across the earthen face of the dam on Thursday, Feb. 9, 2017. (sacbee.com)

In January and February of 2017, excessive precipitation with local amounts exceeding 1000 mm, fell in Pacific coast and Western United States.

- The extreme precipitation alleviated ongoing drought conditions in California,
- but also produced catastrophic flooding and landslides in the Bay Area,
- wrecked Oroville Dam's spillway,
- and closed Interstate 80 in the Sierra Nevada under record-breaking blizzards (Taylor, 2017).

These extreme precipitation events were predominantly fueled by long and narrow channels of large integrated water vapor transport commonly referred to as Atmospheric Rivers (ARs)

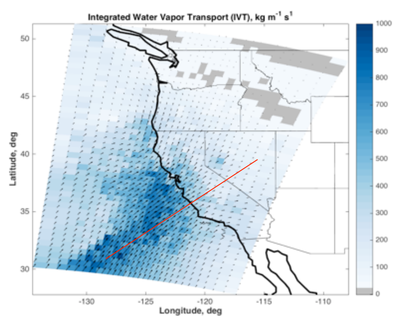

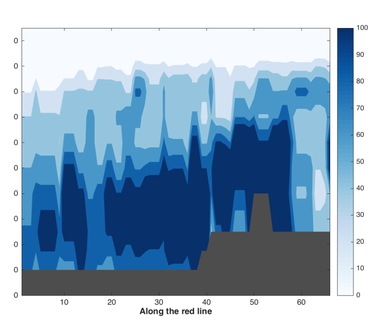

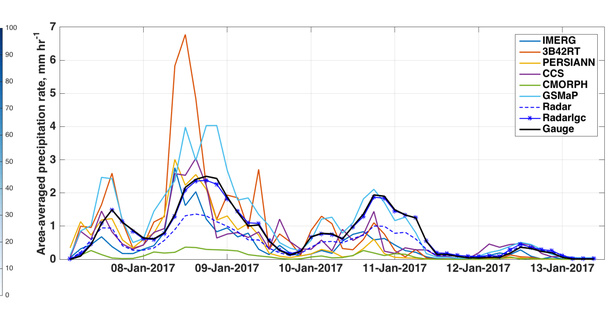

2. Objective

This study evaluates the performance of six commonly used satellite-based precipitation products (IMERG, 3B42RT, PERSIANN, CCS, CMORPH, and GSMaP), as well as ground-based radar products (Radar-only and Radar-lgc) in capturing the ARs precipitation rate and distribution.

3. Results

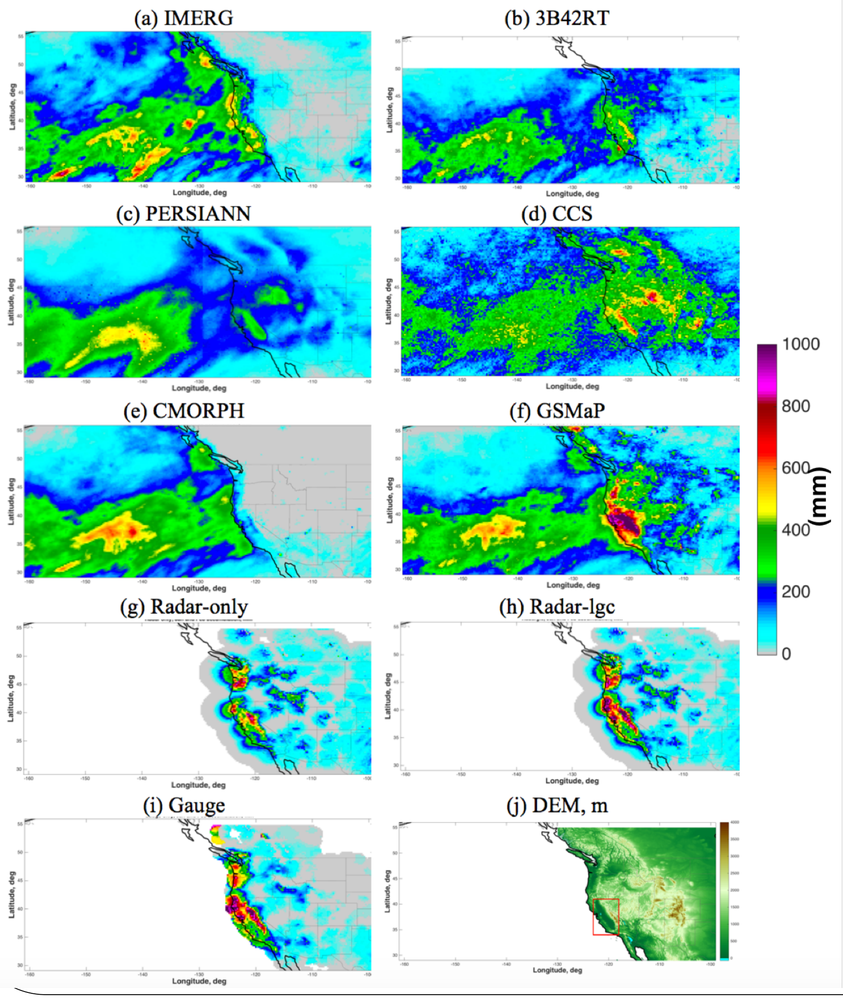

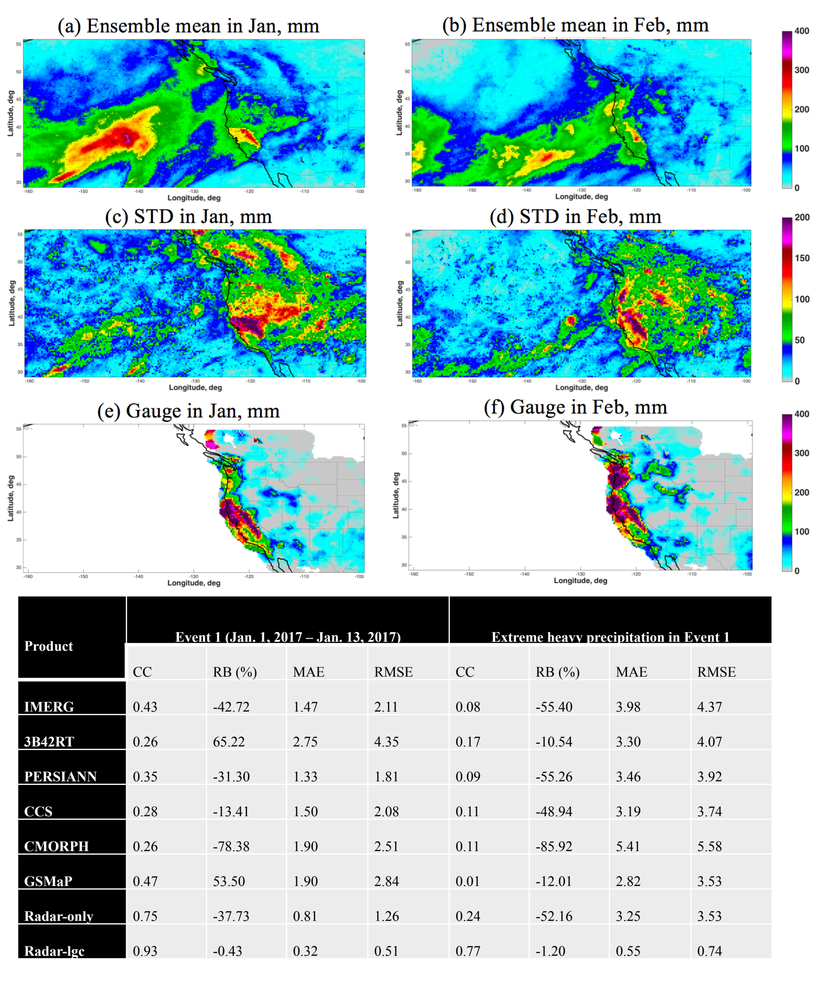

Product	Event 1 (Jan. 1, 2017 – Jan. 13, 2017)				Extreme heavy precipitation in Event 1			
	CC	RB (%)	MAE	RMSE	CC	RB (%)	MAE	RMSE
IMERG	0.43	-42.72	1.47	2.11	0.08	-55.40	3.98	4.37
3B42RT	0.26	65.22	2.75	4.35	0.17	-10.54	3.30	4.07
PERSIANN	0.35	-31.30	1.33	1.81	0.09	-55.26	3.46	3.92
CCS	0.28	-13.41	1.50	2.08	0.11	-48.94	3.19	3.74
CMORPH	0.26	-78.38	1.90	2.51	0.11	-85.92	5.41	5.58
GSMaP	0.47	53.50	1.90	2.84	0.01	-12.01	2.82	3.53
Radar-only	0.75	-37.73	0.81	1.26	0.24	-52.16	3.25	3.53
Radar-lgc	0.93	-0.43	0.32	0.51	0.77	-1.20	0.55	0.74

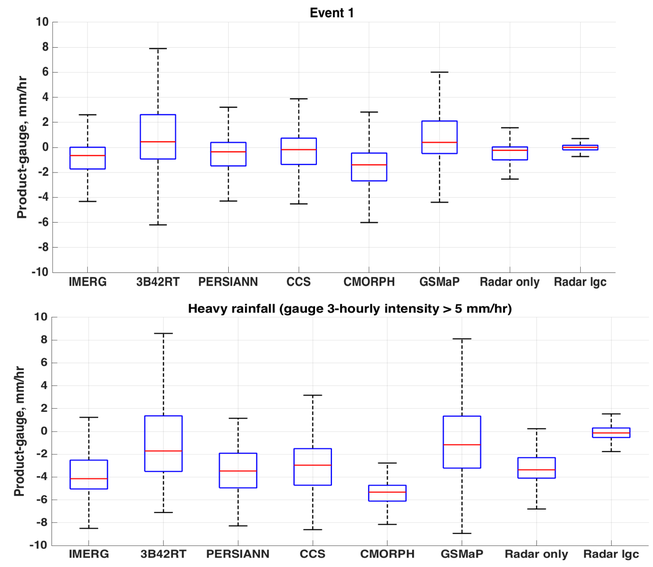

Upper: Error of remote sensing products compared to gauge for Event 1; Lower: focus on the heavy rainfall 3-hourly intensity great than 5 mm hr^{-1} measured by gauge.

4. Conclusion

1) The precipitation map from gauge shows more than 1000 mm precipitation occurred over and in the Sierra Nevada in two months. All satellite QPE products except GSMaP underestimate the heavy precipitation.
2) Over ocean, different satellite products show similar precipitation patterns, except in the area close to the west of southern British Columbia where the precipitation is captured by IMERG, CMORPH, and GSMaP, but missed by IR methods (PERSIANN and CCS).
3) In terms of the statistical performance over land, IMERG correlates the best with gauge observations both in the detection and quantification of precipitation, but it does not yield the best RB and RMSE. CMORPH misses the most precipitation over snow and ice surface.
4) Radar shows totally 38% underestimation of rainfall compared to gauge and is prone to underestimate the heavy precipitation with intensity greater than 2 mm hr^{-1}. Radar-lgc is consistent with gauge measurements because it is bias corrected using gauge measurements.
5) For extremely heavy precipitation (3-hourly precipitation rate > 5 mm hr^{-1}), none of the products show good performance in quantifying the precipitation intensity.

Poster No. EB-10

National Aeronautics and Space Administration

The Impact of the Pacific Decadal Oscillation on the Summertime Temperatures of Inland Water Bodies in Alaska (USA) and Northwest Canada

Nathan C. Healey (329G)
Simon J. Hook (3200)

ABSTRACT

The Pacific Decadal Oscillation (PDO) is a recurring pattern of ocean-atmosphere climate variability affecting the Pacific Basin. Understanding the complex interplay of PDO with climate is particularly important in high latitude regions which are experiencing amplified warming. We have examined the impact of the PDO on the lake surface water temperatures (LSWT) of 15 large inland water bodies in from 2000-2015 using satellite data. Our results indicate the PDO influences summertime (July-September: JAS) LSWT in southern Alaska and northwestern Canada. The strongest influence is on water bodies experiencing a maritime climate, followed by water bodies that experience a transitional regime between maritime and continental classifications, and lastly those that experience a more continental climate regime. Fluctuations in the PDO create increases (decreases) in air temperature when in the positive (negative) phase which are translated to alterations in LSWT (in timing and amplitude) most prevalently in inland water bodies that experience a maritime climate regime. Water bodies in the transitional and continental climates do not show the same response to air temperature fluctuations. In the future, we predict that the water bodies most closely linked to the PDO will likely experience more rapid fluctuations in LSWT on shorter timescales.

MATERIALS AND METHODS

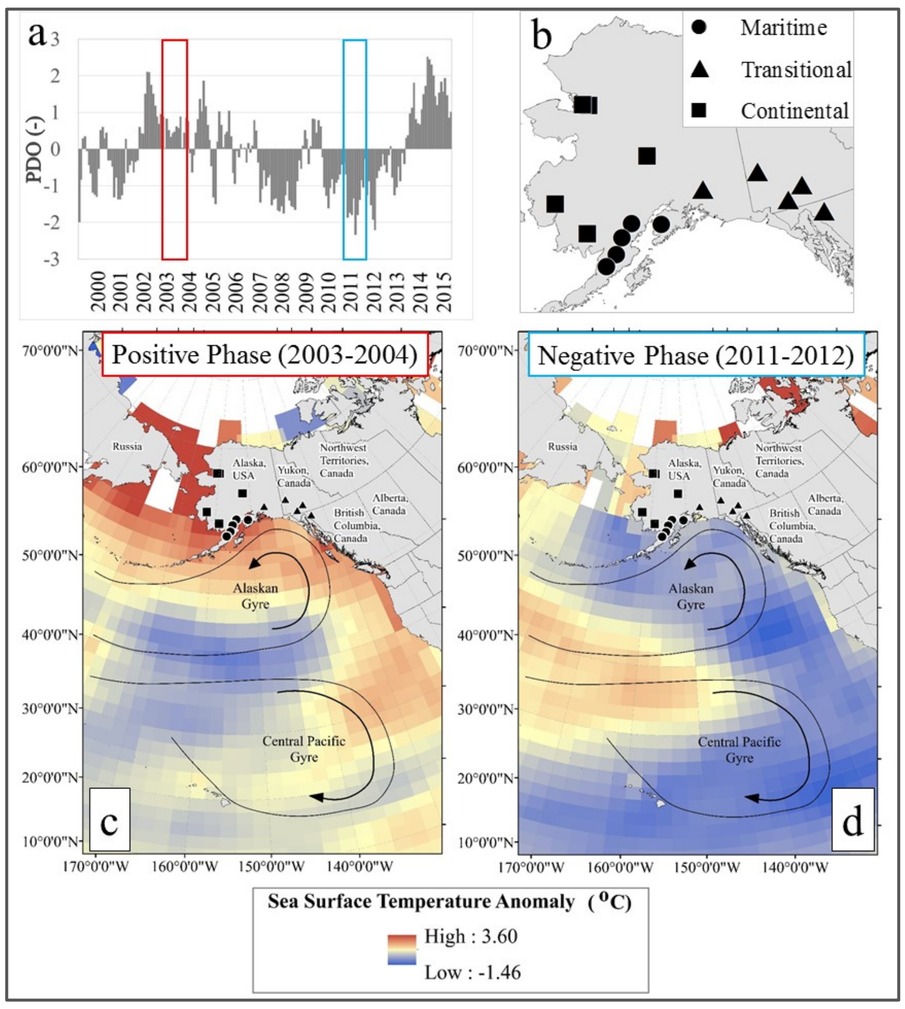

- Three equally sized groups based on generalized climate classification boundaries.
- PDO displays a distinct polynomial distribution. Thus, cubic interpolations were used for comparison between the PDO and summertime (July-September: JAS) inland water body surface temperatures.

Inland Waterbody Surface Temperature (IWbST) v1.0 Algorithm

$$T_s = a_o + a_1 T_{11} + a_2(T_{11} - T_{12}) + a_3(T_{11} - T_{12})\left(1 - sec(\theta)\right)$$

$a_o, a_1, a_2, and\ a_3$: split-window coefficients (water body and satellite specific)
T_{11} and T_{12}: 11 and 12 μm band brightness temperatures
θ - sensor view angle [*Hulley et al., 2011*]

Variable	Value
Location	3 x 3 pixel window around target
Minimum points in JAS Range	6
Smoothing	LOWESS interpolation
Image Time	Nighttime only
Range from Target Coordinates	< 1 km
Standard Deviation in 3 x 3 pixel window	< 0.5 K
Sensor Zenith Angle	< 45°
Cloud Masking	Cirrus Cloud Test (MODIS) High Cloud Test (MODIS) Thermal Test (MODIS) Cloud Mask Intermediate Product – CMIP (VIIRS)
Temperature Range	<= 308.15 and >= 237.15 K

Comparison of MODIS (Terra & Aqua) and VIIRS IWbST Retrievals

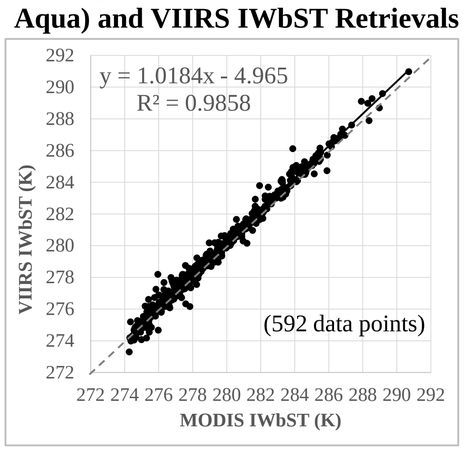

RESULTS AND DISCUSSION

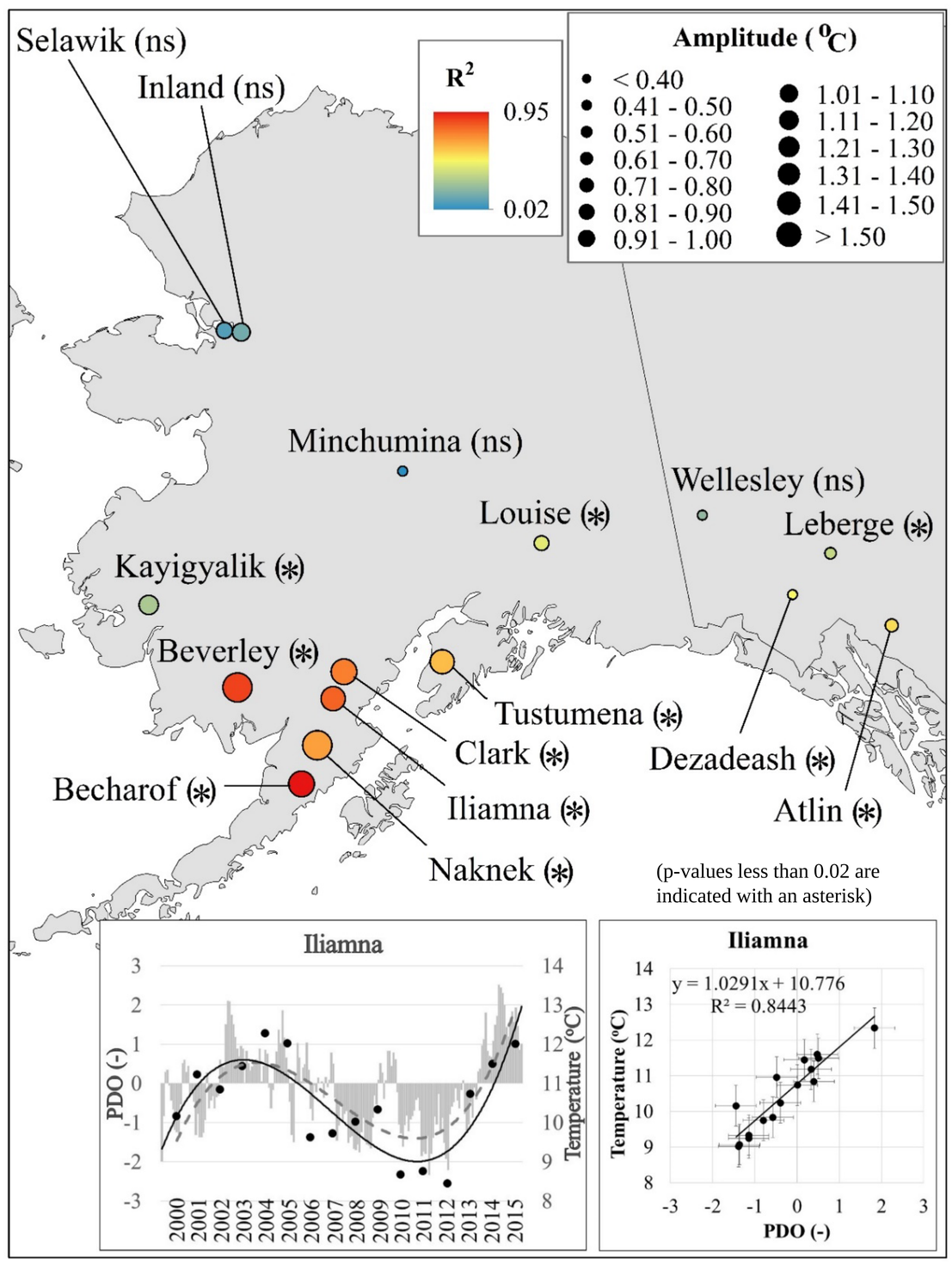

PDO — JAS LSWT

Plotting predicted sinusoidal functions of the PDO vs. LSWT. Error bars: standard error between predicted and observed values.

Value	Units	Maritime (●)	Transitional (▲)	Continental (■)
Average R^2	(-)	0.81	0.54	0.27
R^2 Range	(-)	0.72 - 0.94	0.21 - 0.69	0.02 - 0.89
Average Amplitude	(°C)	1.35	0.44	0.91
Amplitude Range	(°C)	1.22-1.54	0.25 - 0.69	0.36 - 1.67

Influence of the Pacific Decadal Oscillation (PDO) on JAS inland water body surface temperatures:

- **Strongest** on water bodies closest to the Gulf of Alaska (**Maritime and Transitional Groups**).
- **Weakest** on water bodies that are situated adjacent to the Bering Sea on the western/northwestern Alaskan coast as well as in interior Alaska (**Continental Group**).

FUTURE RESEARCH

- Investigate the influence of other climate indices (Pacific North American Index, Arctic Oscillation, etc.) to gain a better understanding of what regulates inland water body temperatures when the PDO influence is not dominant.
- Investigate a larger sample size (more water bodies) that may reveal intricate region-specific details about how different inland water bodies respond to ambient climate conditions.
- Examine potential connections between lake ice dynamics (cover, duration, etc.) and the PDO. This is an extension of recent research [*Screen and Francis, 2016*] showing a strong connection between the PDO and Arctic sea ice extent.
- Improve future modelling of interactions at the atmosphere-water interface and in assessments of (1) future impacts on the global climate system, (2) future management of water resources, and (3) understanding impacts of climate change on the global hydrologic cycle.

National Aeronautics and Space Administration
Jet Propulsion Laboratory
California Institute of Technology
Pasadena, California
www.nasa.gov

Poster No. EB-11

National Aeronautics and Space Administration

High-Resolution THz Spectroscopy of BrO Generated in an Inductively Coupled Plasma

Deacon J. Nemchick (329H), Brian J. Drouin (329H)

Atmospheric Relevance of BrO and Survey of Remote Sensing Observations

A member of the halogen monoxides (XO), this transient radical is a known participant in catalytic ozone degradation cycles.

Stratospheric Chemistry Cycles

Sources of halogen contain compounds in the atmosphere become increasingly less anthropogenic in origin as a function of decreasing row on the periodic table.

Halogen atoms are released from common reservoirs compounds (*i.e.*, HX and CH3X) by either direct photolysis or radical attack.

Once released halogen atoms can return to reservoir through combination with other species (i.e., organics, H2O) or participate in a catalytic ozone degradation cycle where the halogen monoxides are key intermediates.

$$CH_3X + OH\cdot \rightarrow \cdot CH_2X + H_2O$$
$$\cdot CH_2X + O_2 + M \rightarrow \cdot CH_2XO_2 + M$$
$$\cdot CH_2XO_2 + NO \rightarrow NO_2 + CH_2O + X$$

Halogen (X)	Preferred Reaction Path by Percentage	
F	100	0
Cl	50	50
Br	1	99
I	0	100

$X + RH \rightarrow R\cdot + HX$ or $X + H_2O \rightarrow HX + OH\cdot$

$X + O_3 \rightarrow XO + O_2$

$XO + h\nu \rightarrow X + O$

$$\alpha = \frac{\delta O_{3,Br}/\delta Br_y}{\delta O_{3,Cl}/\delta Cl_y} \approx 40 - 60$$

Computational based modeling studies reveal the stratospheric ozone degradation potential of bromine far exceeds that of chlorine.

Stratospheric Br budget is poorly understood prompting the call for remote sensing studies.

Satellite Observation — Global Scale

Optical Wavelengths (338 - 376.6 nm)

Optical Spectrograph and Infrared Imager System	OSIRIS
Scanning Imaging Absorption Spectrometer for Atmospheric Chartography	SCIAMACHY

Rotational (635 & 650 GHz)

Microwave Limb Sounder	MLS
Superconducting Submillimeter-wave Limb Emission Sounder	SMILES

Balloon Observation — In-Situ

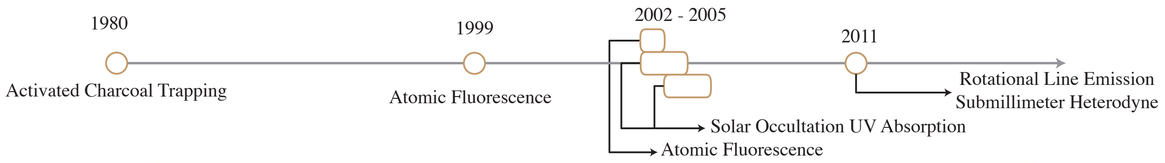

Targets for rotational emission based remote sensing missions include the highest laboratory observed transition ($J' \leftarrow J'' = 51/2 \leftarrow 49/2$) at ~650 GHz.

Experimental Setup

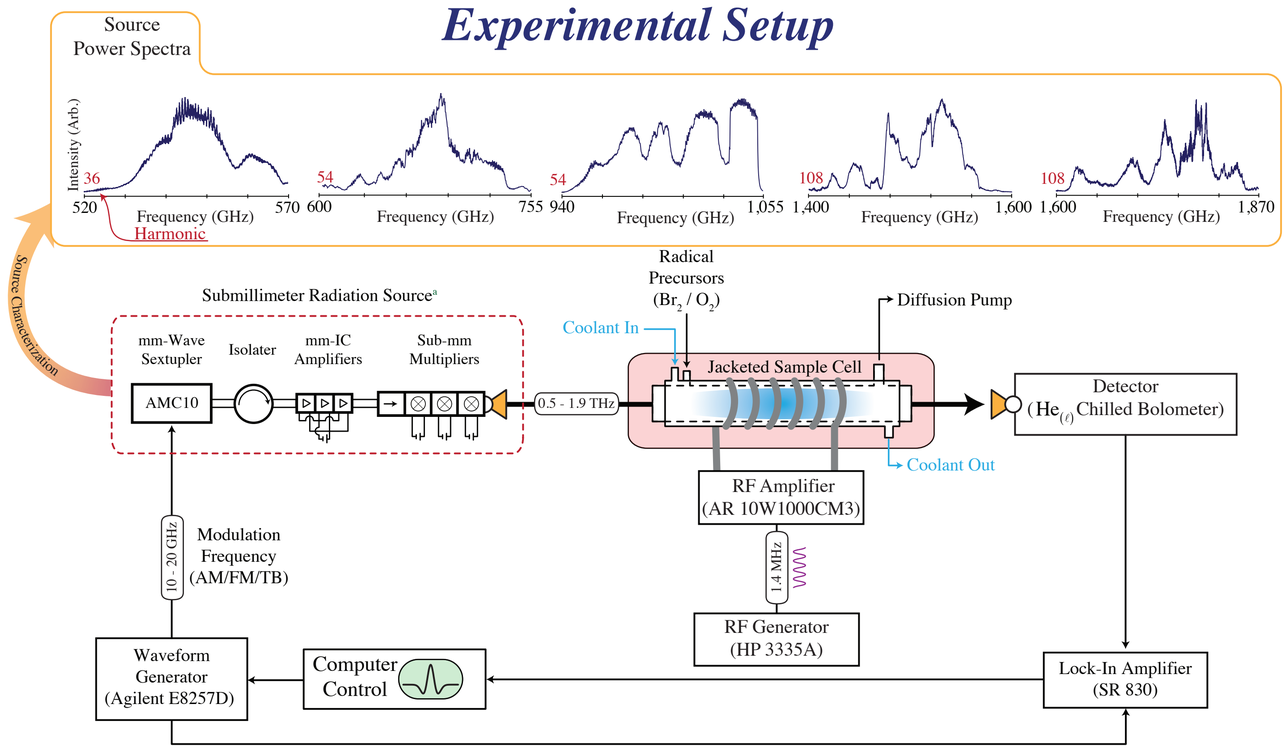

New Spectroscopic Observations

Contrasting phenomenon (*i.e.*, collapse of hyperfine structure and onset of lambda doubling) in the $X_1\,^2\Pi_{3/2}$ state produce intriguing spectral patterns.

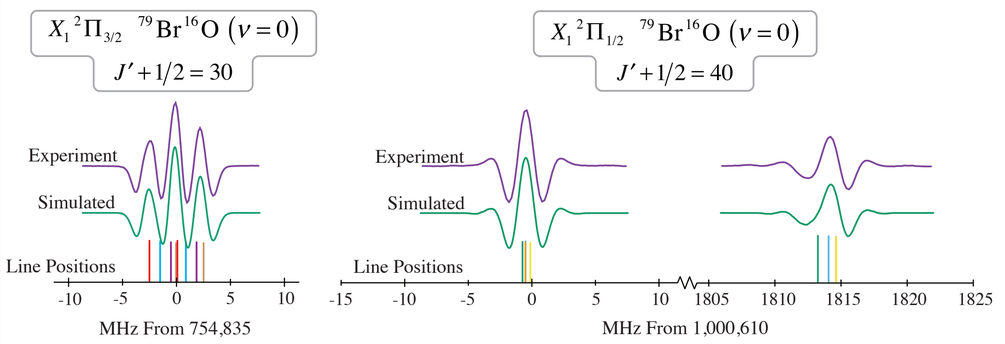

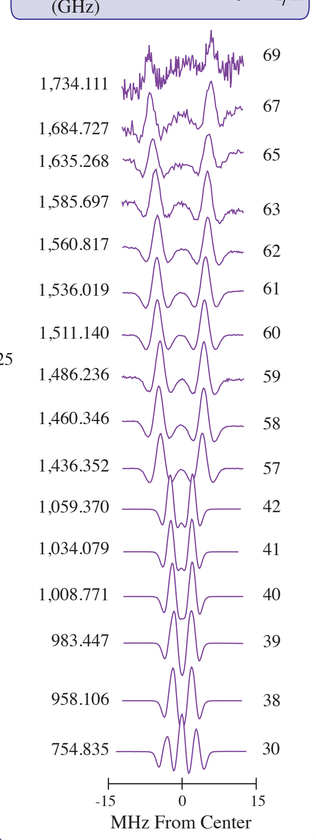

Introduction to BrO and Review of Previous Pure Rotational Studies

Hund's case (a) system, $A_e/B \approx -2200$, where negative spin rotation constant gives rise to an inverted $^2\Pi$ system.

$^2\Pi$ $\Omega = 1/2$ or $3/2$

Isotopologs

$^{79}Br^{16}O$ $^{81}Br^{16}O$ $^{79}Br^{18}O$ $^{81}Br^{18}O$

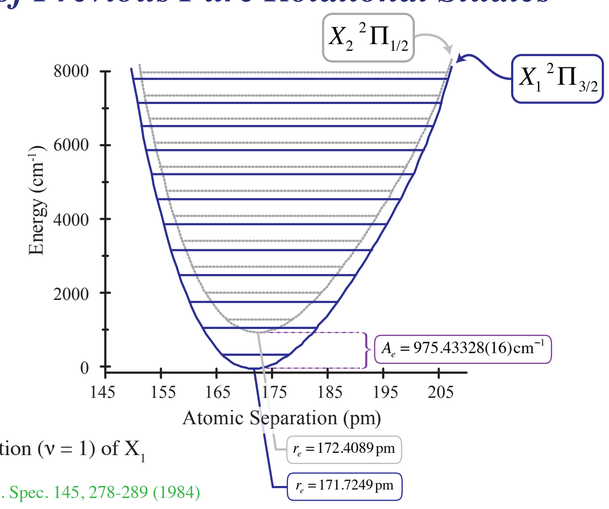

Early Pure Rotational Spectroscopy observed X_1 up to ~350 GHz
- F. X. Powell, D. R. Johnson, J. Chem. Phys. 50, 4596, (1969)
- T. Amano, A Yoshinaga, E. Hirota, J. Mol. Spec. 44, 594 - 598 (1972)
- E. A. Cohen, H. M. Pickett, M. Geller, J. Mol. Spec. 87, 459 - 470 (1981)

Rotationally resolved infrared work targeted the fundamental vibration (v = 1) of X_1
- J. E. Butler, K. Kawaguchi, E. Hirota, J. Mol. Spec. 104, 372 - 379 (1984)
- J. J. Orlando, J. B. Burkholder, A. M. R. P. Bopegedera, C. J. Howard, J. Mol. Spec. 145, 278-289 (1984)

LMR studies provided the first insight into the X_2 manifold allowing for the determination of A_0 and several hyperfine constants
- A. R. W. McKellar, J. Mol. Spec., 86, 54-54 (1981)

Detailed rotational investigation probed both X_1 and X_2 up to ~650 GHz
- B. J. Drouin, C. E. Miller, H. S. P. Müller, E. A. Cohen, J. Mol. Spec. 205, 128-138 (2001)

Objective of the current work is to expand observations to previously unprobed spectral regions allowing for further refinement of spectroscopic parameters with new findings being added to JPL's database

Lambda Doubling for BrO $^2\Pi_{1/2}$ and 3/2

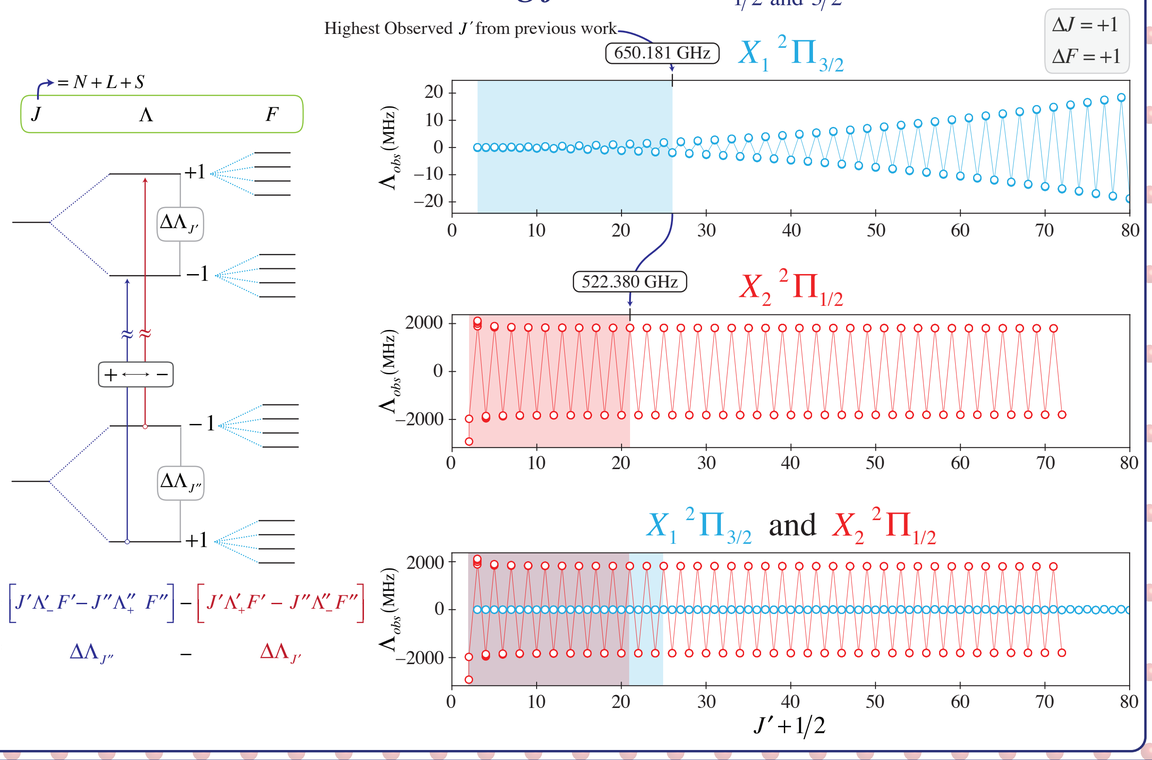

Least-Squares Fitting Results

New line positions are fit to a global Hamiltonian that contains both fine and hyperfine terms allowing for both the refinement of previously determined parameters and the addition of new terms (highlighted below).

Parameter	Value in MHz	Δ_{val} / Δ_{unc}
U_{01}	12834.9533(38)	8.4×10^{-5} / 15.6
Y_{11}	−109.15920(76)	4.5×10^{-3} / 25.5
Y_{21}	−0.20117(39)	−1.0 / 11.0
Y_{31}	−0.012984(70)	1.6 / 3.3
$Y_{41}\times10^3$	−0.3126(48)	−1.4 / 10.0
Y_{02}	−0.01787998(42)	2.7×10^{-2} / 65.3
$Y_{12}\times10^3$	−0.07276(94)	−10.4 / 48.9
$Y_{22}\times10^6$	−1.71(46)	59.3 / 38.0
$Y_{32}\times10^6$	−0.544(50)	−75.7 / 32.3
$Y_{03}\times10^6$	−0.011027(57)	−10.5 / 94.4
Y_{04}	$3.54(58)\times10^{-14}$	
A_e(average)	-29242760.7(43)	-2.2×10^{-5} / 8.5
A_{01}	102.0310(35)	6.4×10^{-3} / 12.3
A_{11}	1.01838 (70)	-8.5×10^{-2} / 2.8
A_{21}	0.02044(20)	1.8 / 2.0
$A_{31}\times10^3$	0.681(18)	−4.0 / 3.1
$A_{02}\times10^3$	0.31040(47)	−0.1 / 64.1
$A_{12}\times10^6$	7.38(64)	−13.5 / 17.9
γ	−663.5(42)	1.0 / 6.7
p_{00}	−1827.832(23)	4.2×10^{-3} / 12.0
p_{10}	−13.511(36)	-4.4×10^{-2} / 1.1
p_{20}	−0.3338(99)	0.2 / 0.0
$p_{30}\times10^3$	−3.04(91)	-1.1 / 0.0
$p_{01}\times10^3$	−0.168(27)	−36.0 / 2.9
$p_{11}\times10^6$	−0.257(24)	0.5 / 1.6
q	−0.6401(47)	6.0 / 41.0
$q_{11}\times10^6$	1.71(46)	
a_{00}	641.44(13)	-1.6×10^{-3} / 0.7
a_{01}	−11.43(26)	−0.3 / 0.0
b_F	19.92(92)	−9.7 / 3.2
c_{00}	−428.0(15)	−0.7 / 3.2
c_{10}	8.22(76)	−2.2 / 0.0
d_{00}	849.70(70)	7.1×10^{-3} / 0.0
d_{10}	−16.1(14)	0.5 / 0.0
$d_{01}\times10^{-3}$	−3.96(17)	0.2 / 1.1
C_I	0.06881(62)	−1.4 / 3.1
eQ_{q2}	860.68(34)	0.2 / 28.0
$eQ_{q1_{00}}$	658.645(74)	5.4×10^{-3} / 9.8
eQ_{qs}	−21.859(84)	−0.2 / 3.1
$eQ_{q1_{10}}$	4.38(11)	−0.8 / 1.2
$eQ_{q1_{01}}\times10^3$	1.644(91)	1.4 / 63.2

Percent Deviation Relative to Previous Work

	Single Lines	Unresolved Pairs
Previous Work	451	279
New Additions	65	115
Total	516	394

Microwave RMS = 0.2902 MHz

$$H_\nu = T_\nu + B_\nu\mathbf{N}^2 - D_\nu\mathbf{N}^4 + H\mathbf{N}^6 + L\mathbf{N}^8 + (1/2)[A_\nu + A_{D_\nu}\mathbf{N}^2 + A_H\mathbf{N}^4), L_zS_z]_+ + \gamma\mathbf{N}\cdot\mathbf{S} + (1/4)[(p_\nu + p_{D_\nu}\mathbf{N}^2), (\Lambda_+^2S_-N_- + \Lambda_-^2S_+N_+)]_+ - (1/2)[(q_\nu + q_{D_\nu}\mathbf{N}^2)(\Lambda_+^2N_-^2 + \Lambda_-^2N_+^2)]$$

$$B_\nu = \sum_l Y_{l,1}(\nu+1/2)^l \qquad H \approx Y_{03}$$
$$D_\nu = \sum_l Y_{l,2}(\nu+1/2)^l \qquad L \approx Y_{04}$$

effective

$$H_{hfs} = aI_zL_z + b_F\mathbf{I}\cdot\mathbf{S} + c(I_zS_z - \mathbf{I}\cdot\mathbf{S}/3) + (1/2)d(\Lambda_+^2I_-S_- + \Lambda_-^2I_+S_+) + C_I\mathbf{I}\cdot\mathbf{N} + [(eQq_1 + N_zS_zeQq_S(3I_z^2 - \mathbf{I}^2) + eQq_2(I_x^2 - I_y^2)]/[4I(2I-1)]$$

hyperfine

Summary, Conclusions, and Future Work

The ground electronic manifolds ($^2\Pi_{1/2}$ and $^2\Pi_{3/2}$) of BrO generated in an inductively coupled plasma (ICP) have been interrogated by employing JPL developed cascaded frequency multiplier sources with $v = 0$ observations being extended from $J'+1/2 = 25\,(21)$ to $J'+1/2 = 70\,(42)$ for $\Omega = 3/2\,(1/2)$.

Only features up to $v = 3$ have been observed with the current ICP setup (10W RF amplifier) implying a near thermal population distribution relative to the cell walls.

Future experiments will target natural abundance ^{17}O lines in the 300 GHz region.

This work will be extended to other halogen monoxides (XO) including X=Cl and I.

Acknowledgements

Special thanks are directed to both Ed Cohen and ShanShan Yu for helpful conversation and instruction.

This work is supported by an appointment to the NASA Postdoctoral Program at the Jet Propulsion Laboratory, administered by the Universities Space Research Association under contract with NASA.

National Aeronautics and Space Administration

Retrieving Cloud Properties with OCO-2

Author: Mark Richardson (329J)
James McDuffie (398E), Jussi Leinonen (329J), Graeme Stephens (3292)

Introduction

- Warm, reflective marine stratus clouds cool the climate
- But they are too thick for CALIPSO (lidar) and too low for CloudSat (radar) to work out their thickness, which would constrain key physics
- **Our in-development OCO-2 cloud retrieval is unique as it obtains marine stratus thickness**
- This is only possible with OCO-2's very high spectral resolution A-band spectra, combined with the weak-CO_2 band to determine liquid phase clouds.

Demonstration case

- Off coast of Argentina, see **top:** MODIS image with yellow line showing OCO-2/CALIPSO track and **bottom:** CALIPSO curtain showing cloud/aerosol.

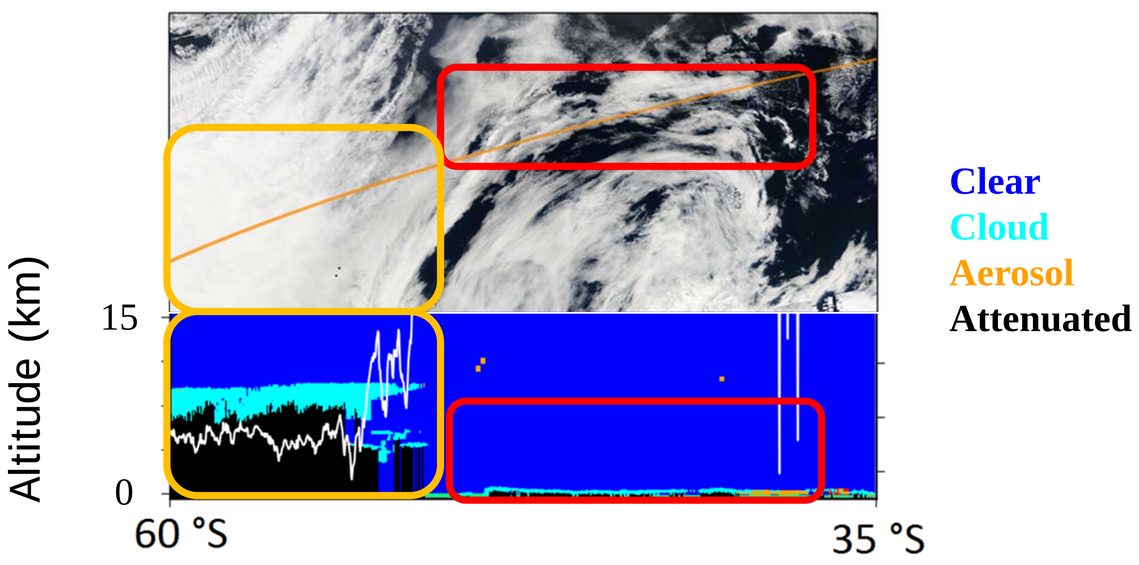

- OCO-2 in good agreement with CALIPSO tops for stratus deck (red box), weaker for multi-layer clouds with overlying cirrus

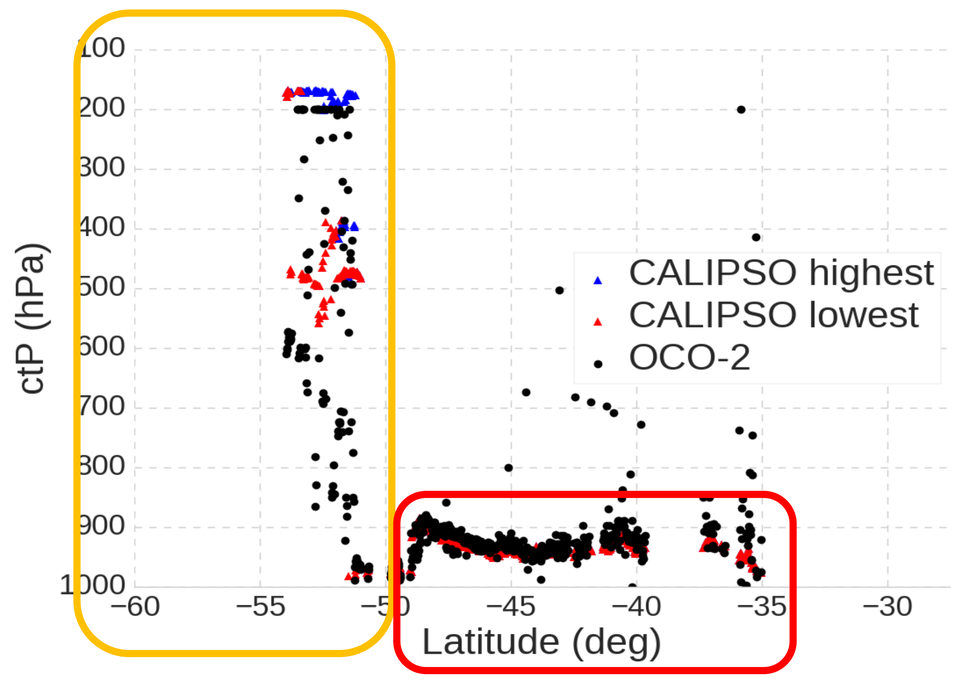

Principle

- Brighter non-absorbing channels mean optically thicker cloud
- Darker absorption channels mean longer photon paths
- Retrieval splits this path into above- and within-cloud components for altitude and thickness. This needs very high spectral sampling.

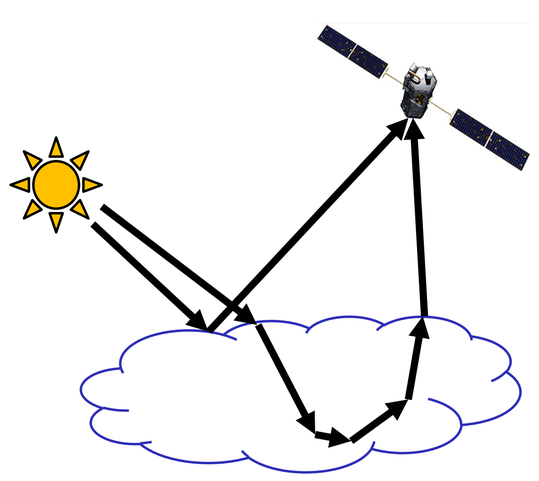

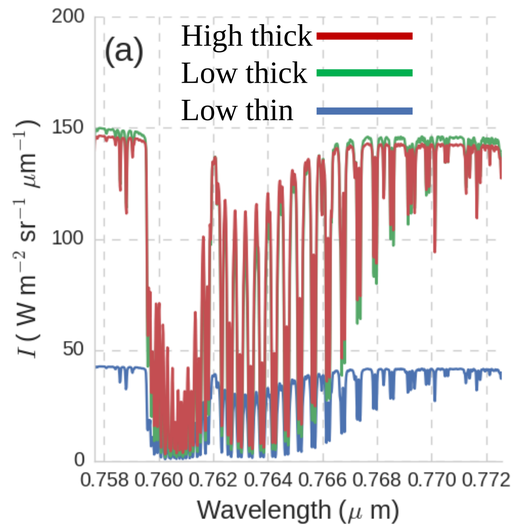

Methods and validation

- Optimal estimation with 75 most-informative channels
- Compare marine stratocumulus measurements of OCO-2 versus CALIPSO cloud-top pressure (left) and MODIS optical depth (right) with ~5 minute difference
- Cloud thickness not yet testable, will use airborne/in-situ.

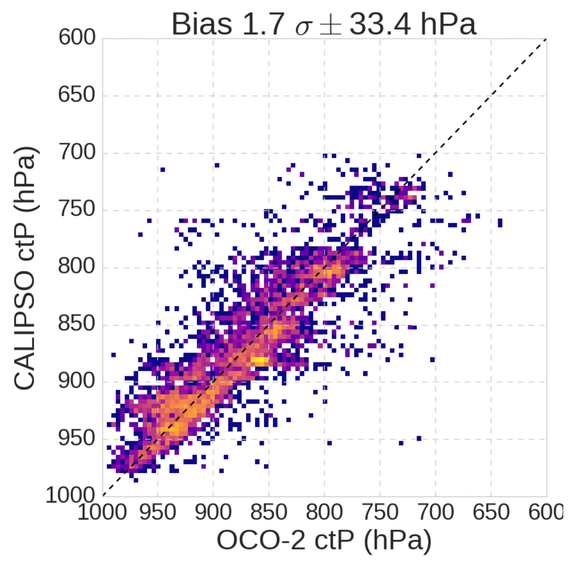

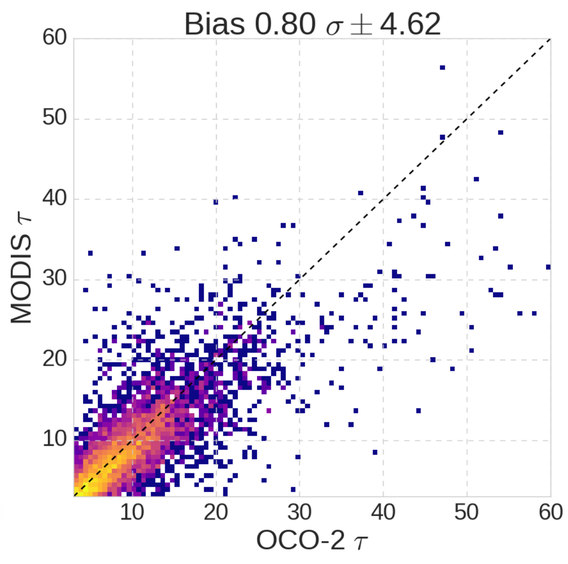

Conclusions and ongoing work

- We exploit unused NASA data – OCO-2 scenes that are too cloudy for CO_2 retrievals. We uniquely retrieve stratocumulus thickness. This should also work for OCO-3 or other A-band instruments, adding to their value.
- Our ctP-τ retrieval works, thickness to be validated by airborne data. Product will be published, allowing new tests of physics that are key for climate feedbacks.

National Aeronautics and Space Administration
Jet Propulsion Laboratory
California Institute of Technology
Pasadena, California

www.nasa.gov

Poster No. EB-13

National Aeronautics and Space Administration

Improvements to the JPL EDMF Cloud Parameterization by a Suite of A-Train Satellite Observations

Author: Mark Smalley (329J)
Matthew Lebsock (329J) and Kay Suselj (398K)

I. Introduction

The Problem

- The representation of shallow maritime clouds in Global Circulation Models (GCM) constitutes one of the largest sources of inter-model spread in future climate projections.
- The development of a cloud parameterization is usually supported by comparisons to Large Eddy Simulations (LES), initialized by idealized observations from field campaigns.
- Idealized initial conditions and selection bias in field campaigns lead to parameterizations that are over-tuned to specific conditions targeted by those field campaigns.

Our Solution for the JPL EDMF

- We tune internal variables of the JPL Eddy-Diffusivity/Mass-Flux (EDMF), a unified turbulence and convection parameterization, according to biases between its simulations and global observations from space-borne satellites.
- Global observations of clouds and precipitation are provided by NASA satellites and instruments (CloudSat, CALIPSO, and MODIS).

II. JPL Eddy-Diffusivity/Mass-Flux Cloud Parameterization

- JPL EDMF parameterizes sub-grid scale atmospheric simulations (Sušelj and Teixeira 2017).
- JPL EDMF is run within a single-column model, but will soon be implemented in a GCM.
- A single-moment microphysics package is coupled to updraft dynamics, conserving total H_2O and θ_L.

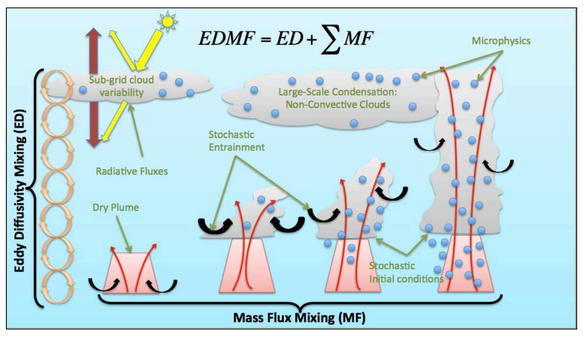

III. Initial Conditions and Experiment Design

- Initial conditions are provided by the NASA MERRA global reanalysis.
- Profiles are taken along GPCI transect (shown at right).
- All profiles have downward motion at 500 mbar.
- 2400 individual EDMF profiles are run for 3 model hours.
- Assessment is performed at the end of the simulation.

MERRA Profiles Near GPCI

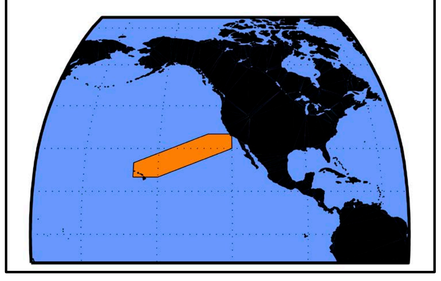

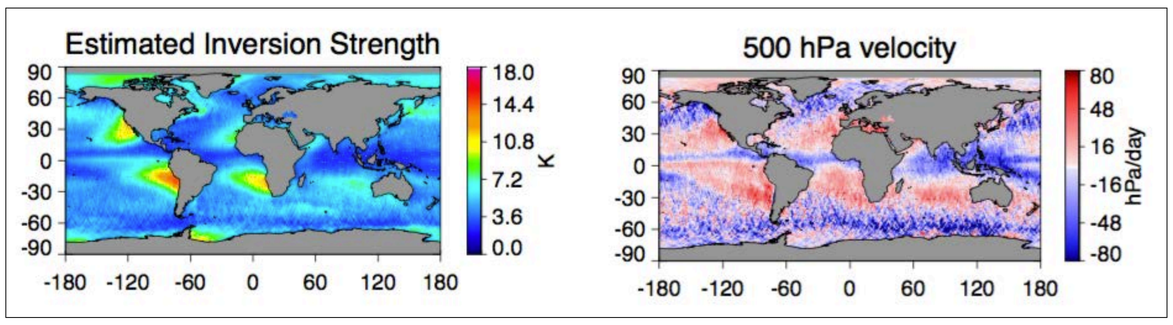

IV. Validation Observations

- CALIPSO/CloudSat vertically-resolved cloud fraction
- MODIS Liquid Water Path (LWP)
- CloudSat rain rate and frequency
- Co-located with MERRA grid in time and space

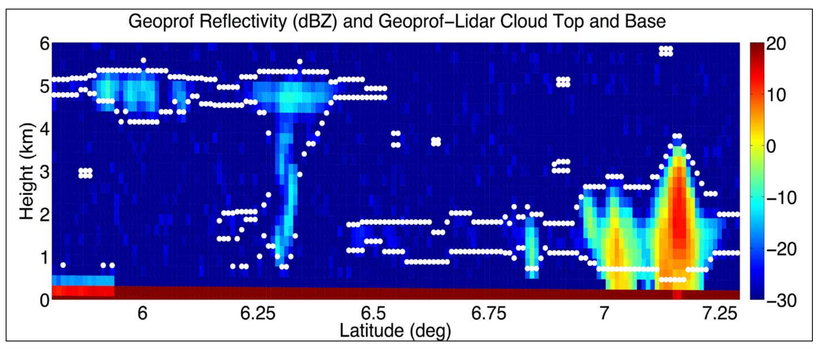

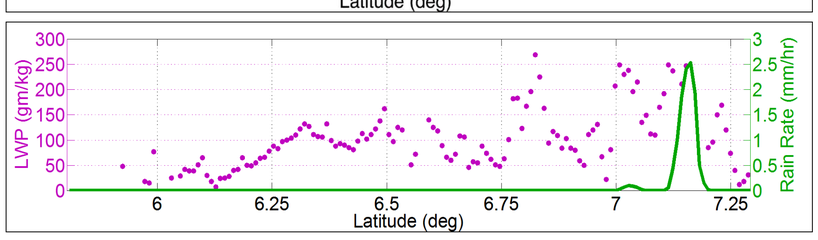

National Aeronautics and Space Administration

Jet Propulsion Laboratory
California Institute of Technology
Pasadena, California

www.nasa.gov

V. General Results

- The EDMF does not reproduce high-CF scenes at high or low altitudes.
- EDMF almost always exhibits very low CF, even in the mid-Troposphere.
- Cirrus are well-represented.

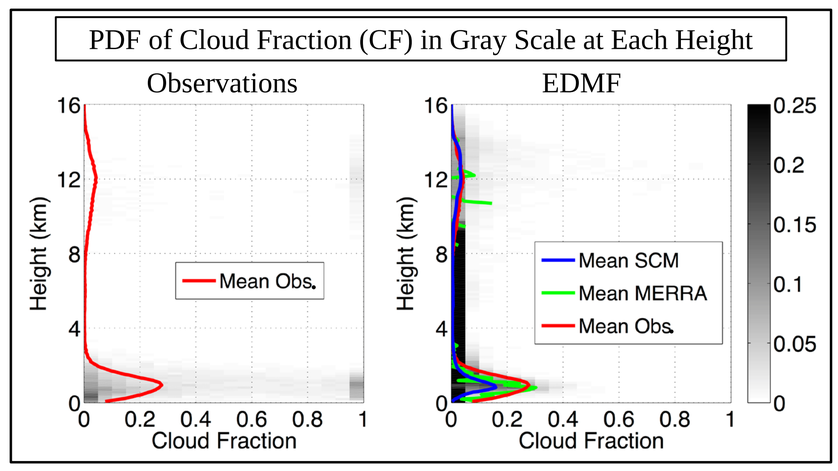

VI. Experimental Results

Example motivation: Control runs have too much heavy rain and rain events are too infrequent.

Description	Desired Effect	Control	Experiment
Average distance between entrainment events (m)	Increase # of Entrainment Events	60	30
Portion of plume mass entrained per event (%)	Increase Effect of Entrainment Events	2	5
Minimum liquid water needed for rain (gm/kg)	Lower Requirement for Rain Initiation	1.0	0.50
Auto-conversion timescale (s)	Increase Rain Rate	45	15

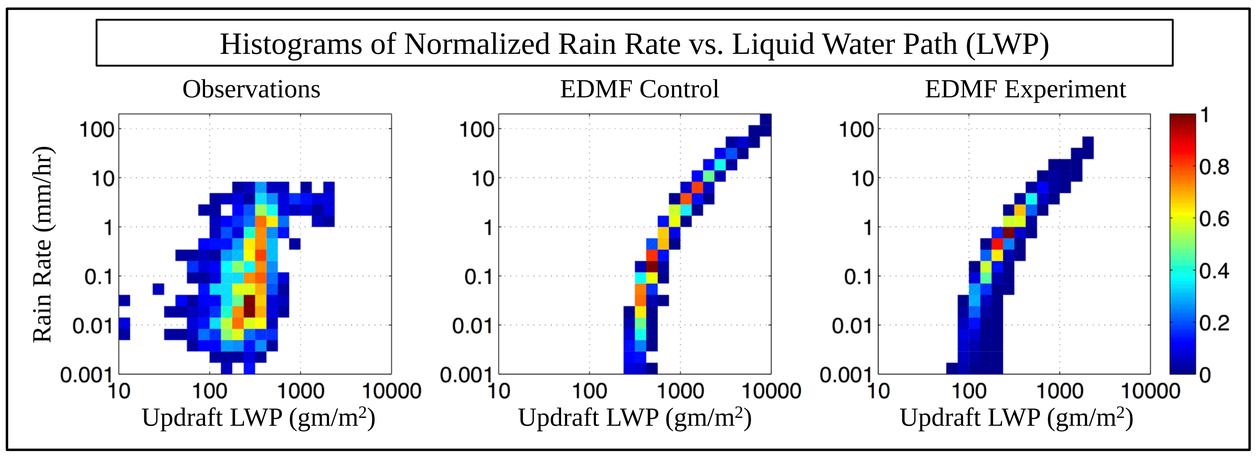

- Increasing entrainment in the Experiment reduces the frequency of heavy rain events that are not observed by CloudSat/MODIS.
- LWP for drizzle events is also reduced from about 300-400 gm/m^2 to just over 100 gm/m^2.
- Average conditional rain rate is still too high in Experiment compared to observations.

VII. Challenges: Sensitivity to Quality of Initial Conditions

- Co-located MAGIC radiosonde profiles of potential temperature (θ) and relative humidity (RH) reveal warm and dry biases in MERRA that can halt updrafts.
- EDMF results are highly dependent on MERRA initial conditions.
- "Garbage-In, Garbage-Out"

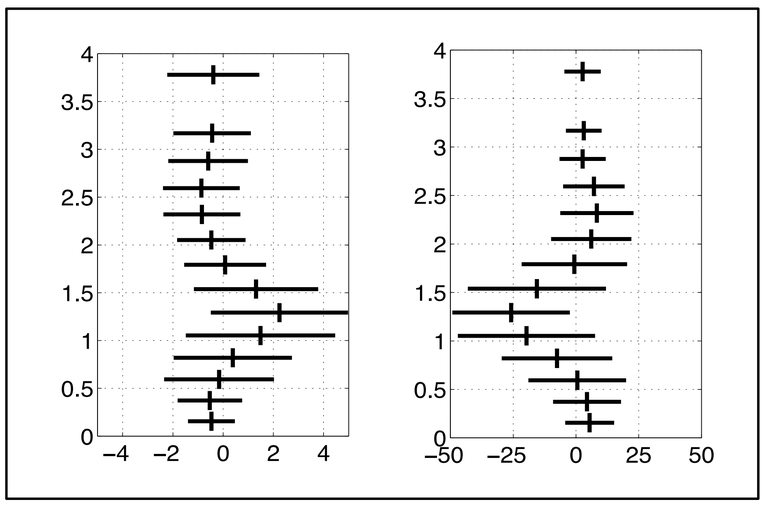

VIII. Conclusions

- ✓ Satellite observations provide a reliable assessment of cloud parameterizations, avoiding selection bias that plagues the standard LES technique. A combined observations/LES validation approach is ideal.
- ✓ JPL EDMF mean cloud fraction compares well with CALIPSO/CloudSat, but the EDMF produces more instances of CF close to the mean and observations report more cloud-free and overcast scenes.
- ✓ Adjustments to the EDMF can alter performance to more closely match observations.
- ✓ The accuracy of simulations is limited by the accuracy of the initial conditions.
- ✓ Next steps: Expand to global observations and then implement EDMF in a GCM for routine use.

References

Sušelj, K., J. Teixeira, 2017. A unified eddy-diffusivity/mass-flux approach for modeling atmospheric convection. Unpublished manuscript.

This research is funded by NASA CloudSat/CALIPSO science team funding to JPL under RTOP/WBS (105357/ 967701.02.01.02.08)

Poster No. EB-14

National Aeronautics and Space Administration

Can we deduce cloud top height changes from GPS-RO bending angle?

Authors: M. Z. Hakuba (329J-Affiliate), C. O. Ao (335G), P. Vergados (335G), A. J. Mannucci (335G), G. L. Stephens (3292)

Introduction

- Temperature and humidity profiles derived from GPS-RO measurements are a vital component in climate studies & weather forecasting. The "raw" measurement, the bending angle (BA), is less commonly used.
- GPS-RO "sees" through clouds. However, Biondi et al. (2011, 2012, 2013) showed that for individual deep convective systems, BA anomalies show a sharp spike highly correlated to the cloud top height (CTH) associated with anomalously cold temperatures (fig. 1).
- Alternatively, the altitude gradient of BA is used to detect the height of tropopause (fig.2) & PBL, characterized by significant changes in temperature & water vapor (e.g., Narayana Rao et al., 2007; Guo et al., 2011; Chien et al., 2016).

⇒ Can we use the **bending angle to track the temporal variability in cloud top height** induced by climatic changes, i.e., changes in convection strength or large-scale dynamics, on climatological time scales?

fig. 1

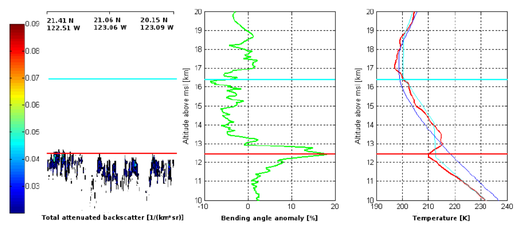

fig. 2

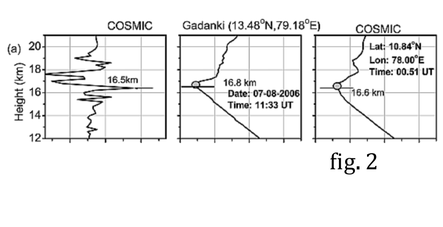

Objectives

1. Do bending angle (BA) anomalies & gradients identify the height of cloud tops (CTH) on larger spatial (e.g., zonal) and temporal (monthly) scales?
2. Does the CTH derived from BA in different regions change as a consequence of global warming & internal variability, such as ENSO?

Methods

- Monthly mean BA as function of MSL height from 1) gridded zonal mean **ROMSAF** climatology & 2) **JPL-Genesis** Cosmic 1-6 collection.
- Histograms of the heights of cloud tops (CTH) & vertically resolved cloud fraction from combined **CloudSat-CALIPSO** 2B-GEOPROF-LIDAR dataset.
- For zonal bands, compute regional anomaly profiles of **BA, CTH frequency** & other parameters in % of the global mean (ROMSAF).
- In the central-eastern Pacific (**NI**) & western Pacific warm pool (**WP**), compute BA (JPL-**GENESIS**) altitude gradient & compare to absolute CTH profiles.
- **Correlate** BA and CTH profiles **& find mutual peaks** to derive **time series & seasonal cycles of cloud top height** from both products.

Results

Zonal mean analysis of bending angle anomaly & CloudSat cloud top height histograms

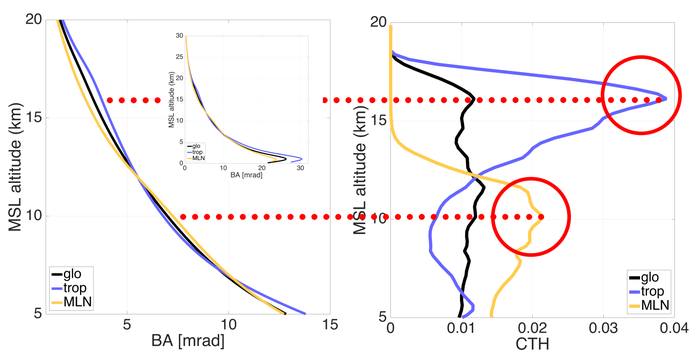

Annual mean (2007-2010) bending angle (BA, left) & cloud top height frequency (CTH, right) for global mean (black), tropics (blue) & Northern mid latitudes (orange).

zonal – global

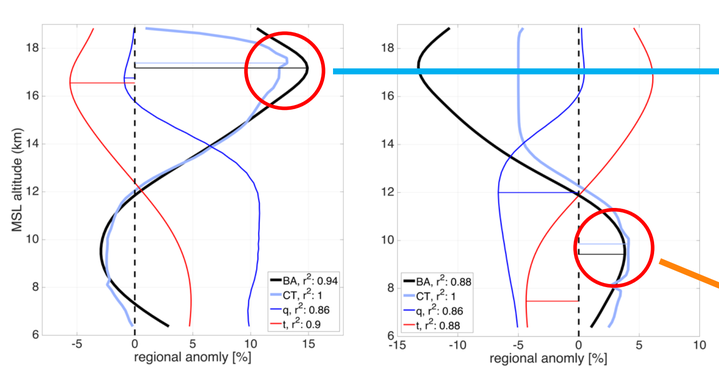

Annual mean anomalous profiles (zonal – global) of BA, CTH, temp. & spec. humidity. Left: **Tropics** (10°S – 10°N), right: Northern **mid latitudes** (40°N – 70°N)

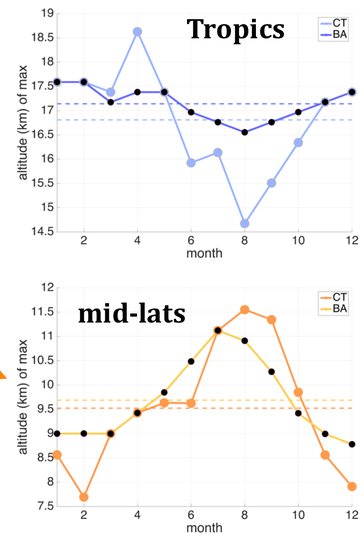

Height of collocated peaks in CloudSat CTH and BA per month. BA reflects annual cycle in CTH almost perfectly in **mid-lats**., but overestimates summer CTH in **tropics**.

R^2 between BA & CloudSat CTH anomalous profiles is **highest in mid-lats & tropics**. Annual cycle of **R^2** is high & consistent in mid-lats., while tropics experience a drop during summer (not shown).

Timeseries of monthly anomalies (not shown) of CTH from BA & CloudSat do not correlate well, but **average CTH agrees well**. Tropics CTH: **17km;** mid-lats CTH: **9.5km**. No significant trend in mid-lats. In the **tropics, CTH increases by 0.06 km per year** according to BA analysis.

Regional analysis based on JPL-GENESIS GPS-RO & "gradient" analysis

1984-2015 cloud liquid water(kgm^{-2})

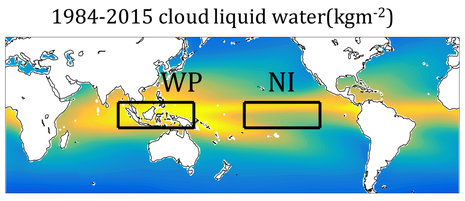

Annual cycles including R^2 & monthly timeseries of CTH from BA (dark) & CloudSat (bright) for the **NI** region (blue) & **WP** (orange). Black dots: R^2<0.3. Green boxes: **El Niño**, red boxes: **La Niña**. **WP** shows significant trend (BA) at 0.14km per year; all other trends are insignificant, but slightly negative in NI (-0.02km per year).

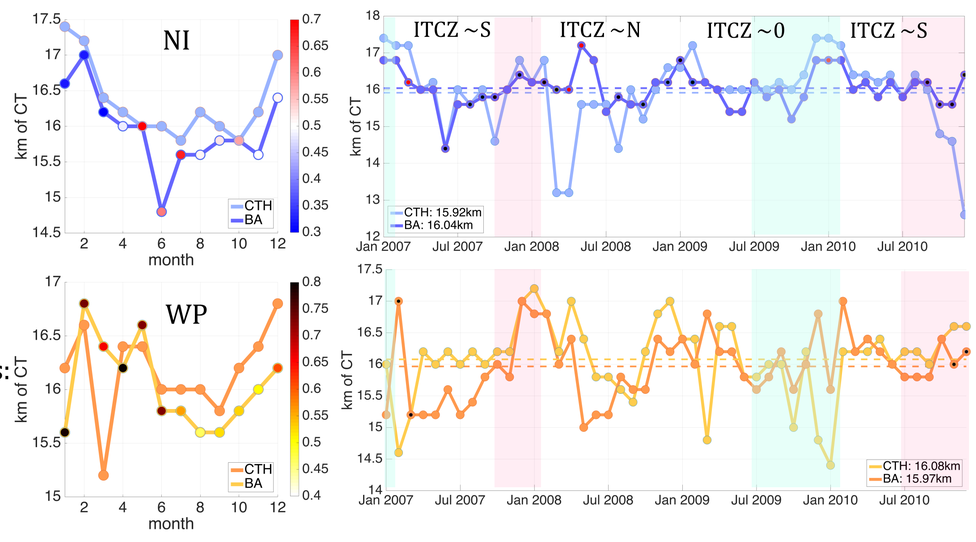

Conclusions

- Peaks in BA regional anomalies & altitude gradients coincide well with peaks in corresponding CloudSat CTH profiles on monthly and annual time scales.
- **R^2** between long-term mean anomalous BA & CloudSat profiles is **highest in the tropics & mid latitudes**.
- Seasonal cycle of R^2 & derived CTH agree well in mid-lats.; tropical BA overestimates CTH in summer. Why?
- No trend in mid lats.; tropical trend at 0.06 km/year.
- In tropical Pacific, peak in altitude gradient of BA coincides well with peak in absolute CloudSat profiles.
- Overall, **BA analysis appears useful to track interannual and seasonal variability in CTH.**
- **Why** does this work & why only in certain places & seasons? Reanalysis of temp. & RH & lapse rate …
- **Can we use BA as a cloud proxy for long-term climate trend research?**

National Aeronautics and Space Administration
Jet Propulsion Laboratory
California Institute of Technology
Pasadena, California

www.nasa.gov

References

- Biondi et al., 2011: Radio occultation bending angle anomalies during tropical cyclones, Atmos. Meas. Tech., 4, 1053–1060.
- Biondi et al., 2012: Thermal structure of intense convective clouds derived from GPS radio occultations, Atmos. Chem. Phys., 12, 5309–5318.
- Biondi et al., 2013: Tropical cyclone cloud-top height and vertical temperature structure detection using GPS radio occultation measurements, JGR, 118.
- Narayana Rao et al., 2007: Identification of tropopause using bending angle profile from GPS radio occultation (RO): A radio tropopause, GRL, 34.
- Chien et al., 2016: Estimation of Marine Boundary Layer Heights over the Western North Pacific using GPS Radio Occultation Profiles, SOLA, 12.
- Guo et al., 2011: Estimating Atmospheric Boundary Layer Depth Using COSMIC Radio Occultation Data, JAS, 68.

Poster No. EB-16

National Aeronautics and Space Administration

Southern Ocean sea level response to large-scale climate forcing

Author: Thomas W. K. Armitage (334H)
Ron Kwok (3340)

Research questions:

- Can we extend the altimeter sea level record to coastal Antarctica *year-round*?
- What is the response of Southern Ocean sea level to large-scale modes of climate variability?
- How did Southern Ocean sea level respond to the recent strong El Niño?

1. Data

Utilize data from CryoSat-2 (2011-) to get full Southern Ocean coverage with monthly resolution. Example, Nov 2014:

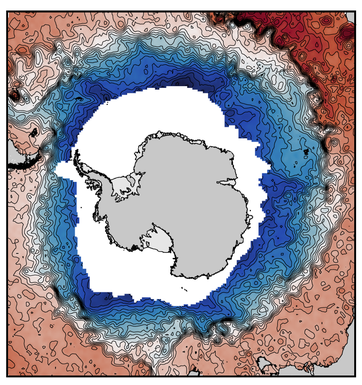

Ice-free ocean:

- Use conventional open ocean altimeter data
- Take along-track CS-2 data from RADS

+

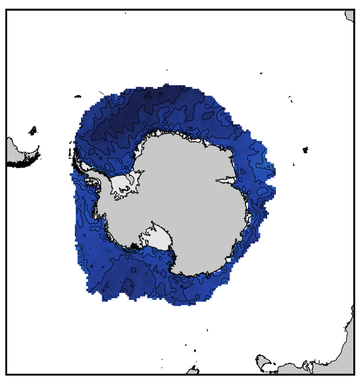

Ice-covered ocean:

- Sea level retrieved from leads and polynyas
- Distinguished based on echo power and width

II

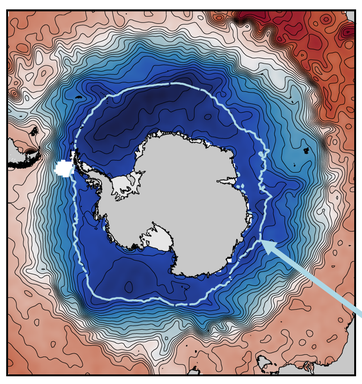

Combined:

- Level the ice-covered and ice-free regions at ice edge
- Nearest neighbor gridding
- Smoothed with Gaussian filter, 80km std. dev.

Sea ice edge (15% concentration)

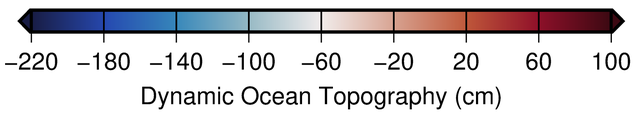

2. Geoid comparison

The EGM2008 geoid is often combined with altimetry to estimate DOT, but it is only constrained by GRACE in coastal regions of Antarctica. The GOCO05c geoid incorporates GOCE data, leading to significant improvement near the coasts.

EGM2008 **GOCO05c**

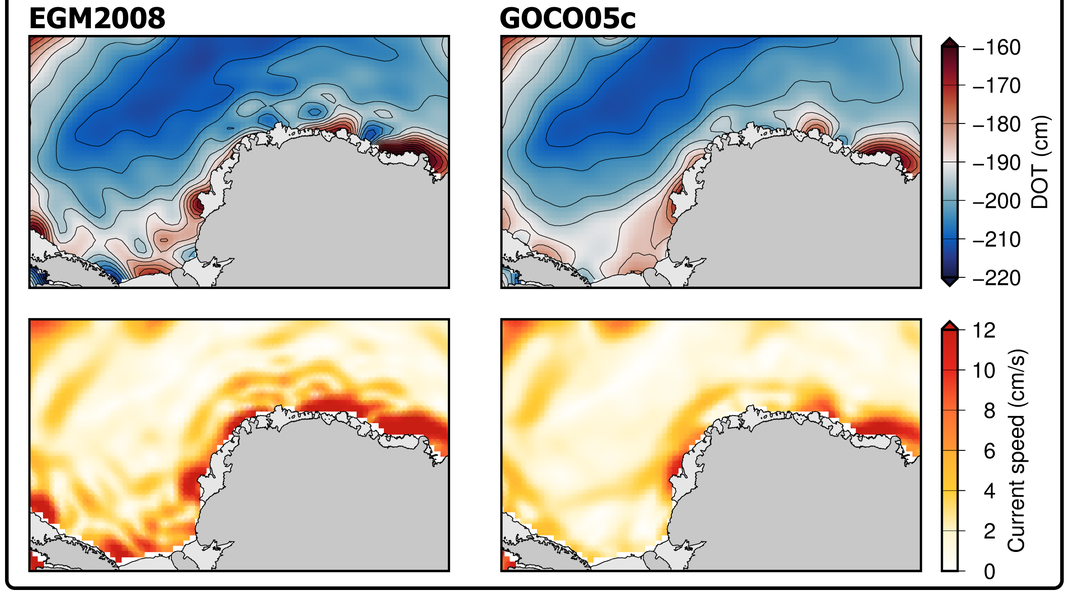

3. Climate forcing

- We construct composites of sea level anomaly based on positive and negative phases of climate indices
- We take the weighted mean of the monthly sea level anomalies for all positive/negative months, weighted by the value of the climate index
- The composites are noisy due to the relatively short time series, but show distinct spatial patterns that are significantly correlated with the associated climate indices (contained by the black contours).

Southern Annular Mode

- The SAM is the leading mode of atmospheric variability in the Southern Hemisphere
- Positive (negative) phases of the SAM are associated with a contraction (expansion) of the belt of westerly winds surrounding the continent
- Along-shore wind anomalies enhance or suppress on- or off-shore transport

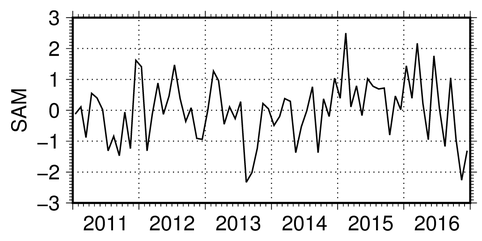

Southern Oscillation

- Positive (negative) phases of the Southern Oscillation are associated with low (high) pressure anomalies centered in the South Pacific
- The resulting wind anomalies cause divergence/convergence in the South Pacific
- Significant coastal sea level anomalies in the Ross, Amundsen and Bellingshausen Seas are associated with along-shore wind anomalies

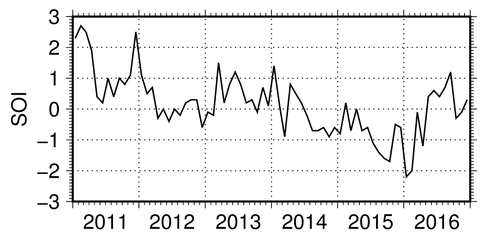

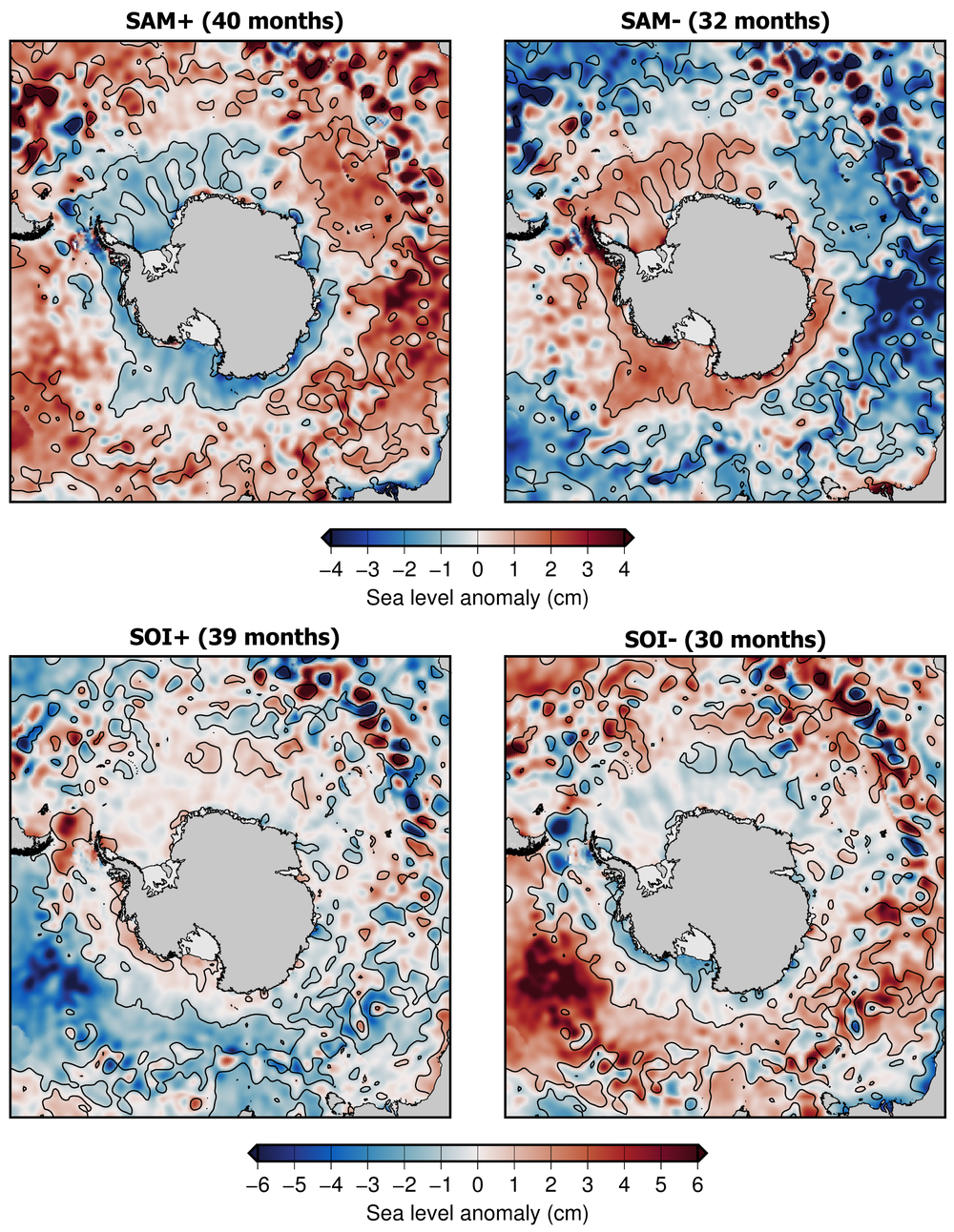

4. Sea level response to the 2014-16 El Niño

- We compute the sea level anomaly for June 2015-April 2016, the period that this event was at it's most intense
- We compute the sea level anomaly for June 2015-April 2016, the period that this event was at it's most intense
- As expected, the sea level anomaly pattern resembles the SOI- composite
- Surface pressure/wind anomaly consistent with the observed sea level anomaly
- Along-shore wind anomalies act to reduce/reverse on-shore Ekman transport

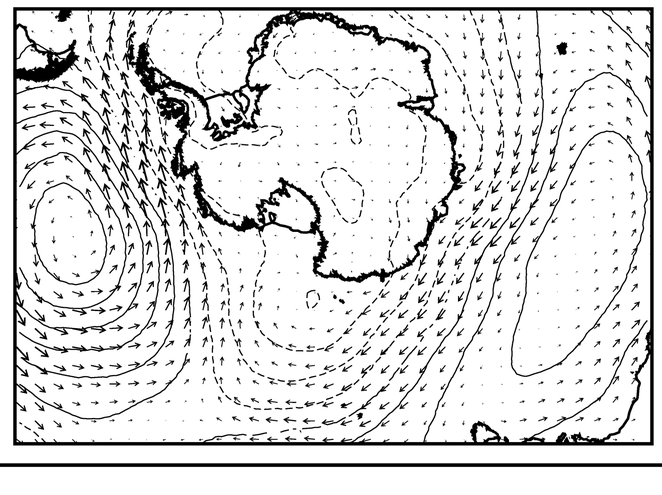

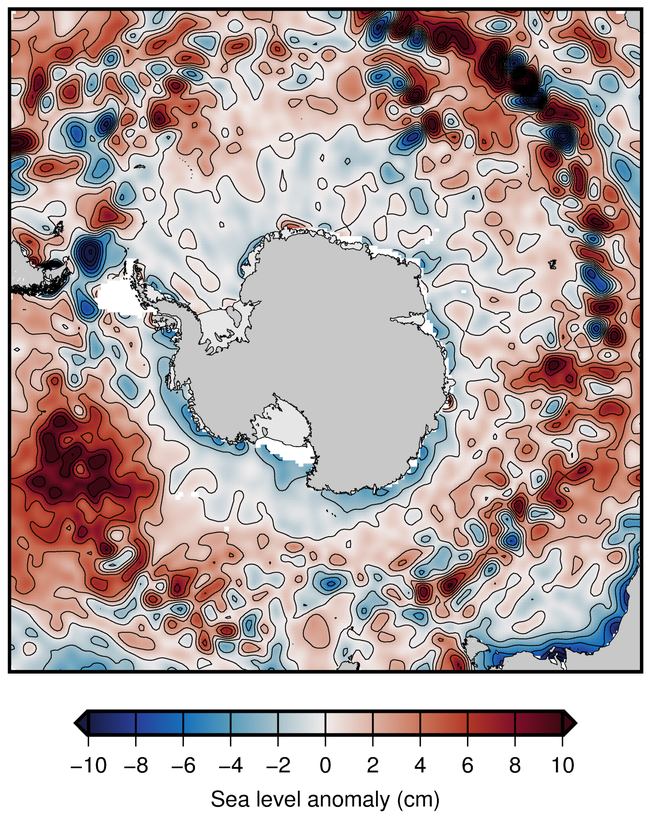

Summary:

- With CryoSat-2 we can generate basin-wide composites of Southern Ocean SSH with monthly resolution
- Southern Ocean sea level shows a significant response to both the Southern Annular Mode and the Southern Oscillation, with influence extending to coastal regions of Antarctica
- El Niño/Southern Oscillation could influence warm Circumpolar Deep Water reaching West Antarctic ice shelves by modulating the strength of the Antarctic Slope Front

Poster No. EB-18

National Aeronautics and Space Administration

Jet Propulsion Laboratory
California Institute of Technology
Pasadena, California

www.nasa.gov

National Aeronautics and Space Administration

Impacts of ducting and heavy precipitation on GPS Radio Occultation (RO) retrieval

Author: K.-N. Wang(3222), C. O. Ao(335G), M. de la Torre Juarez(3222), F. J. Turk(334H)

GPS Radio Occultation (GPS-RO) and PBL

- GPS-RO is an effective technique to profile atmospheric temperatures from accurate **refractivity measurements**.

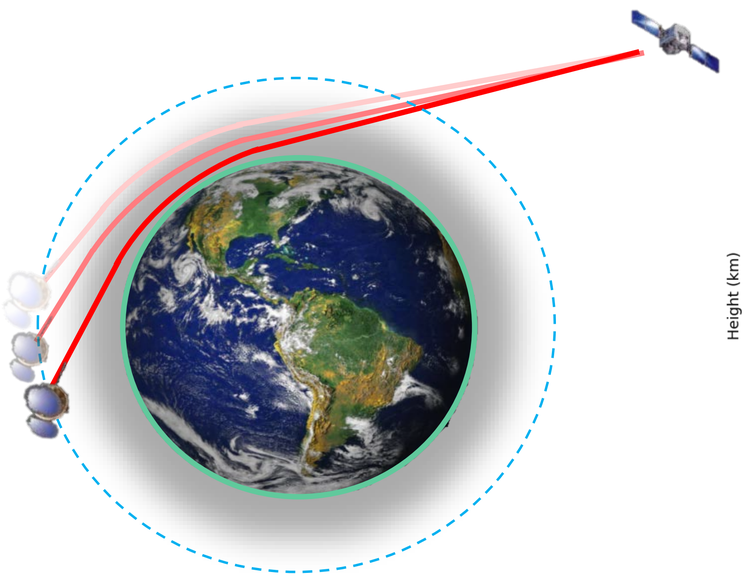

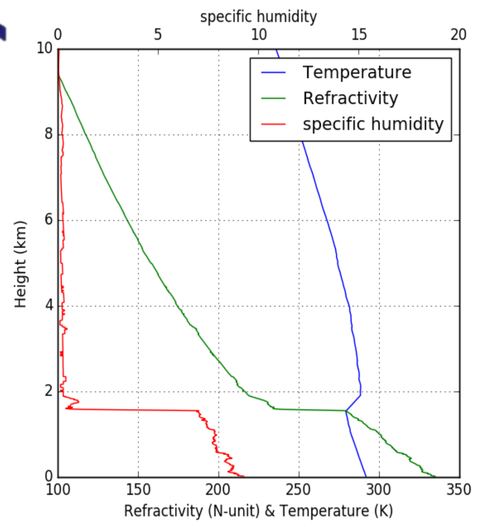

- The retrieved refractivity profiles can also be used to characterize the **PBL height** and the **strength of inversion**.

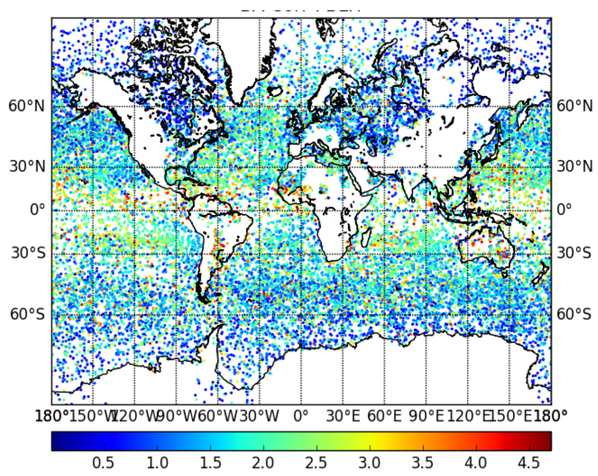

< PBL Height >

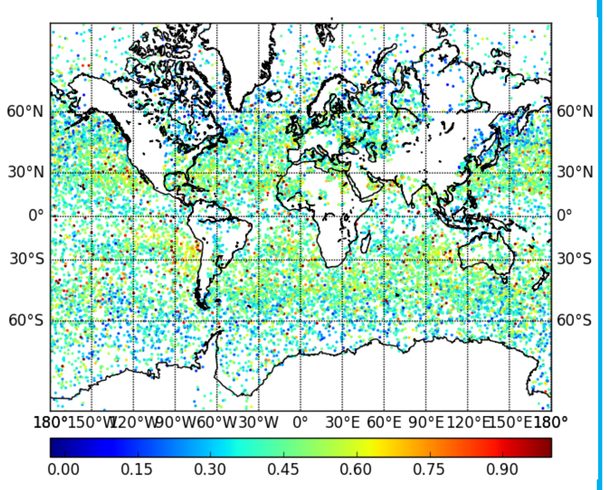

< PBL sharpness >

Ducting and Refractivity Correction with PW

- **Ducting**: causes the transmitting ray to follow the Earth's curvature due to a large negative refractivity gradient.
- Extreme refractivity gradients can **violate the uniqueness condition** to perform traditional inverse Abel transform. [*Xie et al, J. of Atmos. and Ocean. Tech., Vol. 23, 2006*]
- RO refractivity measurements will be **negatively biased (N-bias)** below ducting layers in the lower atmosphere.

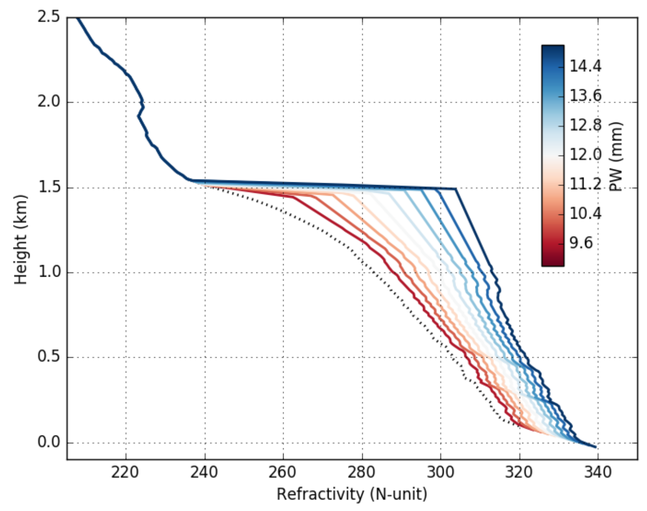

- A novel approach is shown to implement **optimal estimation** into RO retrievals by selecting the profile whose **precipitable water (PW)** best matches a measurement, that can be acquired by NASA remote sensing instruments such as AMSR-E and GPM.

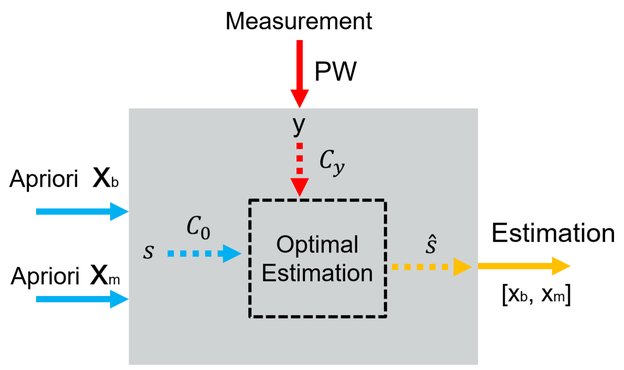

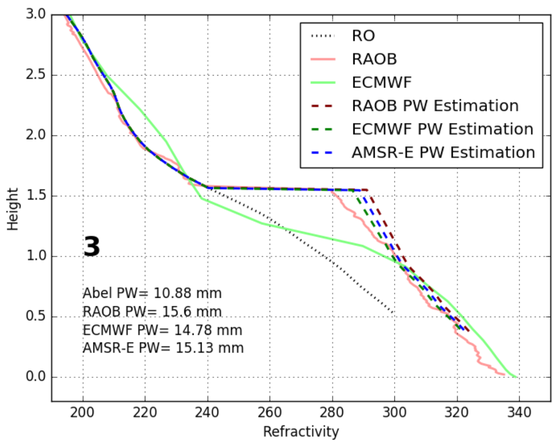

- Statistical results show that the **PW-constrained optimization** can retrieve the RAOB-based refractivity profiles with **low biases** (<1%) below the ducting layer**.** Different external PW sources affect the reconstruction results differently [*Wang et al, Atmos. Meas.. Tech., Discussion Paper, 2017*].

N-bias due to Heavy-Precipitation

- The refractivity profiles retrieved by GPS-RO are significantly greater (>1%) than the collocated ECMWF results **when precipitation occur**.
- The impact of precipitation upon signal phase can be simulated by the **ray tracing program** considering the known rain rate along the ray path measured by **TRMM**.

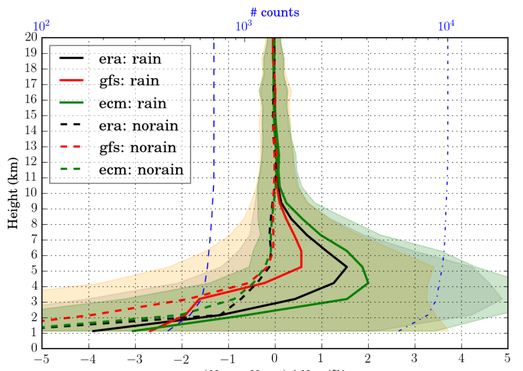

[*Ramon, 2017*]

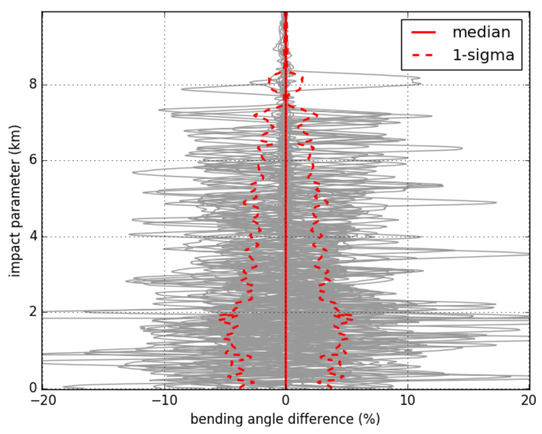

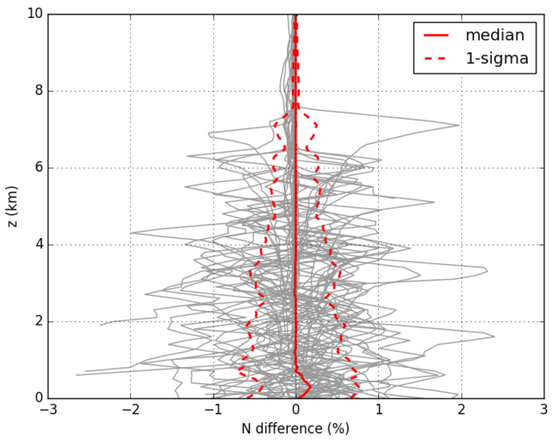

- The statistical test containing 64 cases of ray tracing data shows the **profiles are un-biased** when precipitation occurred. The observed bias can be due to the underestimation of refractivity in ECMWF model.

Ducting and Reconstruction with Reflected signal

- The bending angle of the **reflected GPS-RO signal** may contain ducting layer information for **self-correcting** refractivity retrievals.

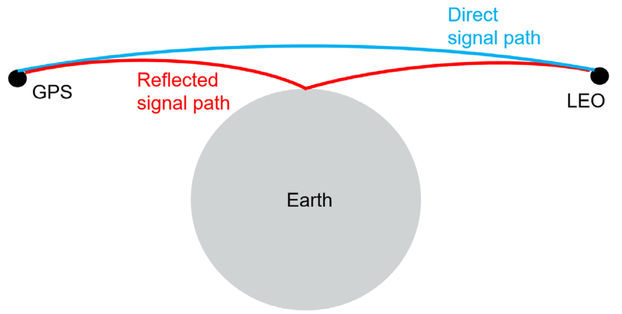

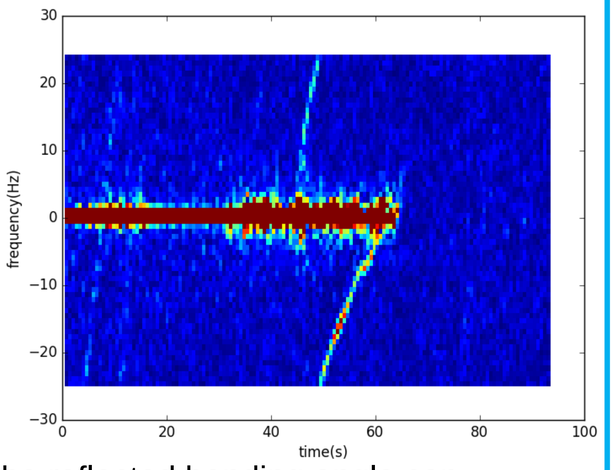

- Forward model simulation shows that the reflected bending angle can **distinguish different refractivity profiles below ducting** – which indicates the potential of being an extra external measurement in optimization approach.

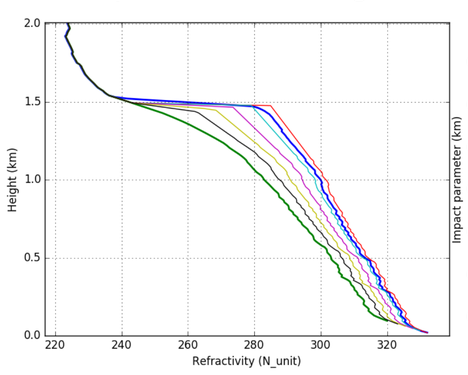

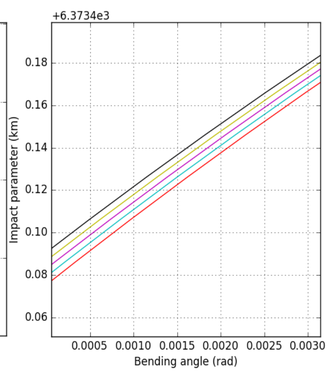

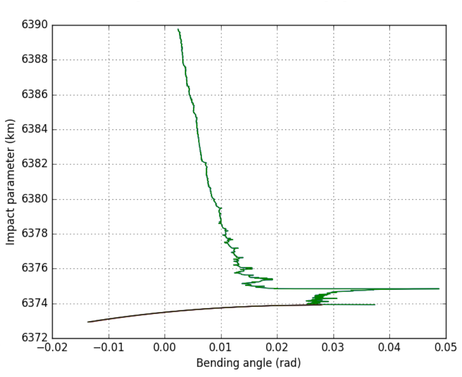

National Aeronautics and Space Administration

Jet Propulsion Laboratory
California Institute of Technology
Pasadena, California

www.nasa.gov

Poster No. EB-20

National Aeronautics and Space Administration

COWVR and CYGNSS Synergy

Mary Morris (382G)
Shannon T. Brown (382G)

CONTEXT

- **Motivation:** location of tropical cyclone (TC) center useful for a variety of applications

- **CYGNSS** [1]
  - Cyclone Global Navigation Satellite System
  - Constellation of 8 small satellites currently on-orbit
  - Observations of ocean surface wind speed in all precipitating conditions

- **COWVR** [2]
  - Compact Ocean Wind Vector Radiometer
  - Similar performance to WindSat [3], lower cost
  - Provides observations of ocean surface wind vector
  - Launch anticipated early 2018

- **Objectives:**
  - ➢ Develop wind direction retrieval algorithms using WindSat data, in anticipation of COWVR launch
  - ➢ Combine information from CYGNSS and WindSat in TC scenes
  - ➢ WindSat TC wind direction retrieval, assuming wind speed from CYGNSS algorithms developed in [4]

TEST CASE

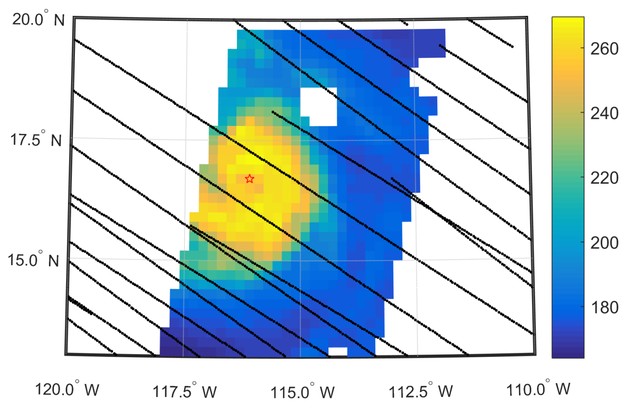

Figure 1: Hurricane Hilary (2011) as seen from WindSat. Color shows brightness temperature (K), 37.0 GHz (H-pol), aft swath. Black lines show locations of simulated CYGNSS data. Red star is location of center fix from best-track files.

- Hurricane Hilary, 12 UTC, 27 Sep. 2011, Cat 3 storm
- WindSat data: use overlapping fore-aft swath position
- CYGNSS data: simulated from mission simulator/HWRF

REFERENCES

[1] Ruf, C., and Coauthors, 2016: New Ocean Winds Satellite Mission to Probe Hurricanes and Tropical Convection. Bull. Amer. Meteor. Soc., 97, 385-395, doi:10.1175/BAMS-D-14-00218.1.
[2] Brown, S. and Coauthors, 2014: The compact ocean wind vector radiometer: A new class of low-cost conically scanning satellite microwave radiometer system. 94th American Meteorological Society Annual Meeting, Atlanta, GA.
[3] Gaiser, P. W., and Coauthors, 2004: The WindSat space borne polarimetric microwave radiometer: Sensor description and early orbit performance. IEEE Trans. Geosci. Remote Sens., 42, 2347–2361.
[4] Morris, M., and C. S. Ruf, 2017: Determining Tropical Cyclone Surface Wind Speed Structure and Intensity with the CYGNSS Satellite Constellation, J. Appl. Meteor. Climatol., doi: 10.1175/JAMC-D-16-0375.1.

METHODS

- Experiment:
  - Replace areas of difficult wind speed retrievals from WindSat with an estimate from CYGNSS-based parametric model
  - Parametric model algorithm: takes patchy and noisy CYGNSS data and creates continuous TC wind speed vortex
  - Using CYGNSS wind speed, retrieve wind direction from WindSat
    - 18.7, 37.0 GHz
    - 3rd and 4th stokes
    - fore and aft swath

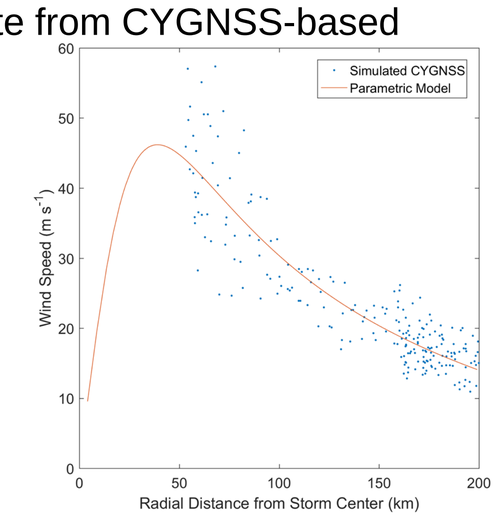

Figure 2: Resulting parametric model fit to simulated CYGNSS observations within 200-km of storm center for test case shown in Fig.1.

RESULTS

WITHOUT CYGNSS →

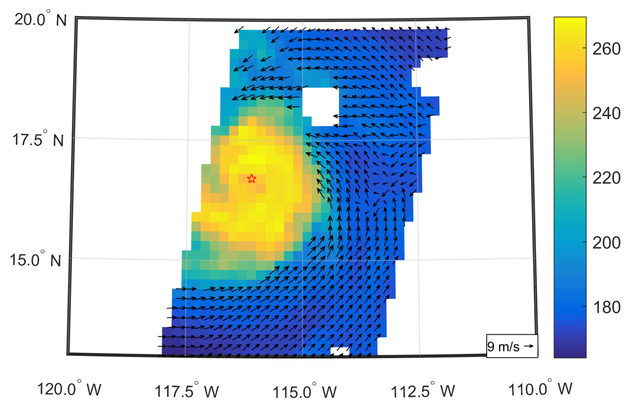

Figure 3: Hurricane Hilary (2011) as seen from WindSat. Color shows brightness temperature (K), 37.0 GHz (H-pol), aft swath. Black arrows indicate the wind direction retrieved, with quality control applied, and no CYGNSS information used.

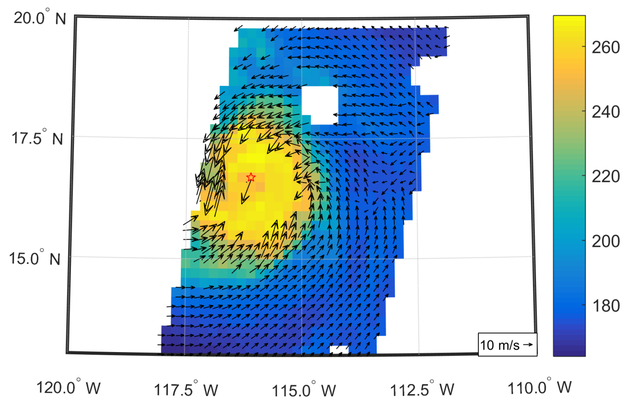

← WITH CYGNSS

Figure 4: The same as Figure 3, except that CYGNSS information is now used in the wind direction retrieval.

ACKNOWLEDGEMENTS

Many different sources of data were used in this analysis and we gratefully acknowledge the institutions and research groups providing data and support: particularly, the CYGNSS Science Team, Remote Sensing Systems, and the Naval Research Laboratory.

National Aeronautics and Space Administration
Jet Propulsion Laboratory
California Institute of Technology
Pasadena, California

www.nasa.gov

Poster No. EB-21

National Aeronautics and Space Administration

Improving spinups of the present day Greenland Ice Sheet (GrIS) by using ISSM to simulate the evolution of the GrIS over the last 120,000 years.

Author: Josh K. Cuzzone(329C-Affiliate)
Eric Larour (329C), Mathieu Morlighem (329C), Nicole Schlegel (329C)

Introduction

- Because of the large thermal inertia of ice sheets, the present day temperature distribution of the Greenland Ice Sheet (GrIS), is a reflection of conditions the ice sheet endured during the last glacial cycle.
- Although much success has been garnered in obtaining detailed ground, airborne, and space borne measurements useful in the modeling of the GrIS, the accuracy of future projections also rely on properly simulating the history of the GrIS over timescales equivalent to its thermal and dynamic evolution.

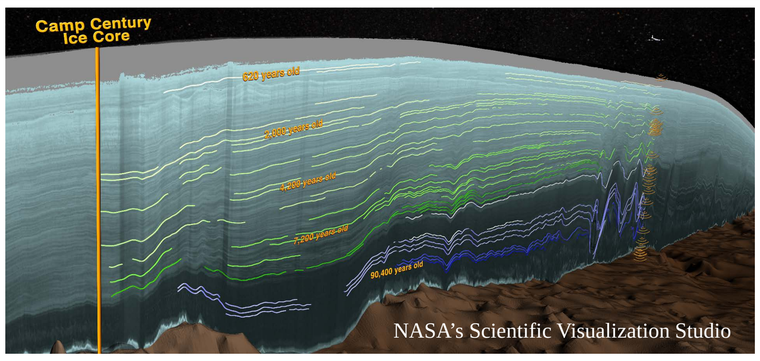

Objectives

1. Use the Ice Sheet System Model (ISSM) to produce the first of its kind, higher order simulation of the GrIS over the last glacial cycle (120 kyr ago to present).

2. The simulated present day GrIS will capture the thermal and dynamic memory of the ice sheet, therefore improving the spinup of the GrIS needed for future simulations.

Methods

- Begin with present day GrIS geometry (Ice, surface height, bedrock, and thickness).
- Inversions of InSAR present day ice surface velocities to estimate basal sliding.
- Higher order, 3 dimensionsl (5 layers) thermal model using P1xP3 finite elements in the vertical. Anisotropic mesh with resolution ranging from 3km to 20 km.
- Scale a present day climatology along the NGRIP oxygen isotope record to produce temperature and precipitation forcings back to 120 kyr ago.
- Implement a sliding scheme which allows the basal friction coefficient to vary as a function of modeled basal temperatures.
- Surface mass balance relies on a positive degree day scheme.

Results

1.)

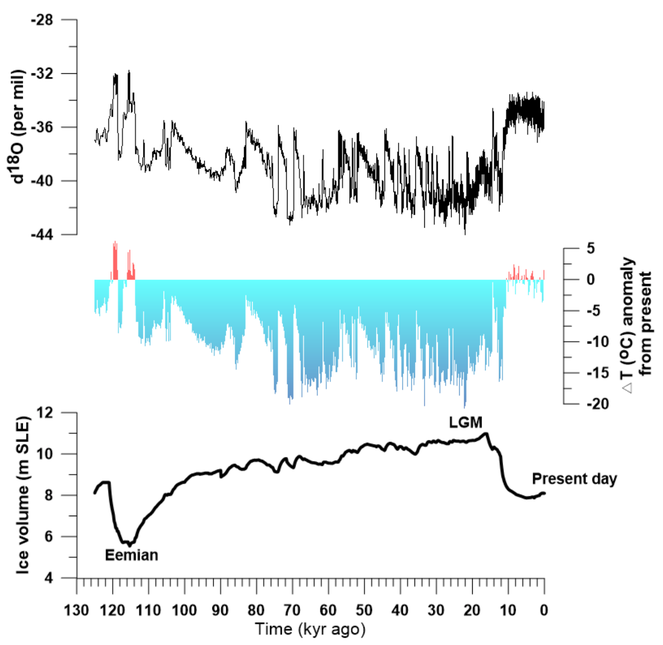

1.) NGRIP oxygen isotope record (**top**), temperature anomaly from present (**middle**), and simulated total GrIS ice volume in meters of sea-level equivalent (**bottom**). **Simulated present day total ice volume is 6% lower than observed** .

2.)

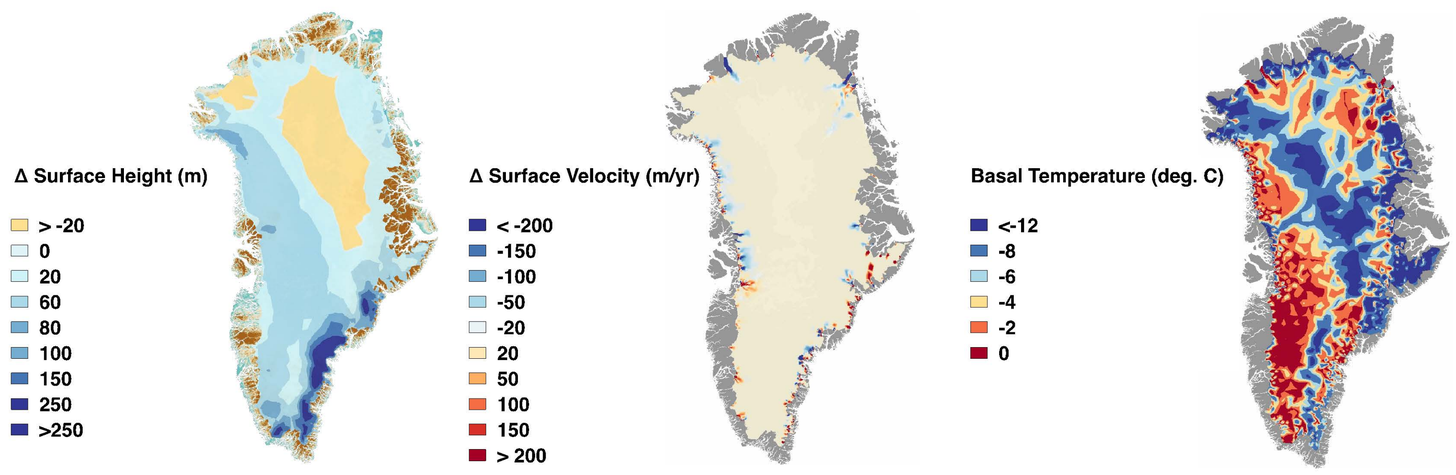

2.) Left: Simulated present day surface height anomaly (model – observed). **Middle:** Simulated present day surface velocity anomaly (model – observed). **Right:** Simulated basal temperatures at the end of model spinup (present day).

Conclusions and future work

- We present the **first 3D Higher Order simulation** of the GrIS evolution over the last glacial cycle.
- Simulated ice volumes at the Eemian and LGM are well within the range of uncertainty in the literature.
- ISSM reasonably simulates present day total ice volume, surface topography, surface ice velocity, and basal temperatures, and represents an improvement over many Shallow Ice models used for similar experiments.
- Future improvements will take advantage of **ISSM's data assimilation** capabilities, and integrate data of past GrIS margin history to invert for unknown parameters such as basal friction and surface mass balance, therefore improving the model spinup and ultimately the initial condition used for simulating the response of the GrIS into the future.

A.)

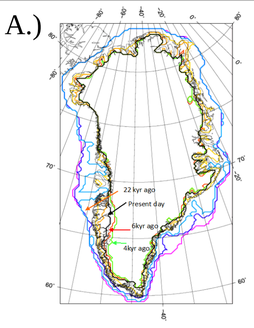

B.)

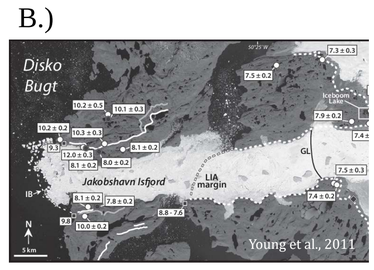

Examples of past margin history for GrIS which can be used as data assimilation targets to improve spinups. **A.)** Continental GrIS **B.)** Jakobshavn region

National Aeronautics and Space Administration

Jet Propulsion Laboratory
California Institute of Technology
Pasadena, California

www.nasa.gov

Acknowledgments

We acknowledge model setup help and fruitful discussions with our JPL colleagues Helene Seroussi and Surendra Adhikari. This work was supported under NASA Grants and NSF grant 1504230 .

Poster No. EB-22

National Aeronautics and Space Administration

Satellite synoptic view of the Bay of Bengal "river in the sea"

Séverine Fournier[1] (329B)
J. Vialard[2], M. Lengaigne[2,3], T. Lee[1] , M. Gierach[1] and A.V.S. Chaitanya[4]

[1]Jet Propulsion Laboratory, California Institute of Technology, Pasadena, California, USA, email : severine.fournier@jpl.nasa.gov
[2] LOCEAN-IPSL, Sorbonne Universités, UPMC, Université Paris 06, CNRS-IRD-MNHN, Paris, France
[3] Indo-French Cell for Water Sciences, IISc-NIO-IITM-IRD Joint International Laboratory, NIO, Goa, India
[4] National Institute of Oceanography, Council of Scientific & Industrial Research, Goa, India

1 - MOTIVATIONS

- The Bay of Bengal (BoB) is affected by several large rivers
- The resultant freshwaters influence:
  - salinity stratification
  - air-sea interactions (tropical cyclones, convection, rainfall)
  - biogeochemistry (low productivity)
- Lack of in-situ data to monitor spatiotemporal sea surface salinity (SSS) changes in BoB
- Limitations in SSS data from previous satellite missions: Aquarius (low resolution), SMOS (poor quality in northern BoB)
- Thus, there is a lack of understanding about processes causing BoB SSS variability. However, since May 2015, there are SMAP SSS data

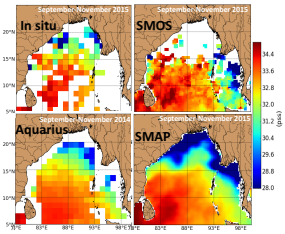

3 - DATA

- SMAP Sea Surface Salinity (SSS)
- In situ SSS
- Altimetry: Sea Surface Anomaly (SLA) and ocean currents

4 - VALIDATION OF SMAP DATA

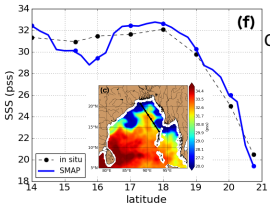

Comparisons SMAP/in situ SSS along transects:
- Good agreement
- Strong gradients well captured by SMAP

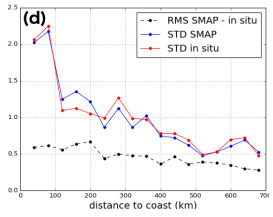

SMAP/in situ RMSD as a function of the distance to the coast:
- slightly larger within 200 km of the coast than offshore
- always smaller than the STD of the SMAP or in situ SSS signals

2 - KEY REGIONAL OCEAN AND CLIMATE FEATURES

- **Eastern Indian Coastal Current (EICC)**:
  - Redistributes freshwater within the BoB
  - Reverses seasonally (flows southward in October-March)
  - Confined to the western boundary

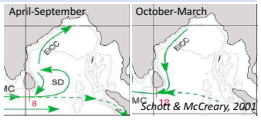

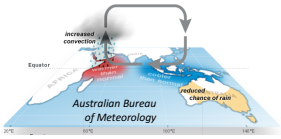

- **Indian Ocean Dipole (IOD)**: interannual climate mode in the Indian Ocean similar to El Niño in the Pacific Ocean. It peaks in fall and lasts for ~6 months

During a positive IOD: anomalous easterly winds strengthen along the equator:
-> temperature gradient across the Indian Ocean (cold waters Java/Sumatra)
-> negative sea level anomaly (SLA) along the rim and anomalously weak EICC

5 - OBSERVATIONS OF THE VARIABILITY OF THE FRESHWATER PLUME SOUTHWARD EXTENSION

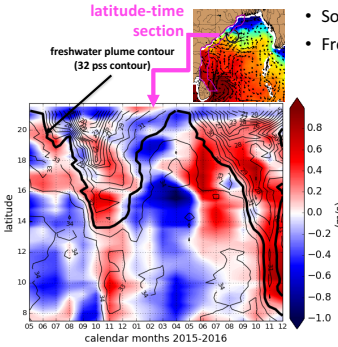

- Southward alongshore currents stronger in 2016
- Freshwater plume carried further south (2016: 8°N, 2015: 13°N)

Alongshore southward currents (colors) and SSS (contours) within 200 km of the eastern coast of India

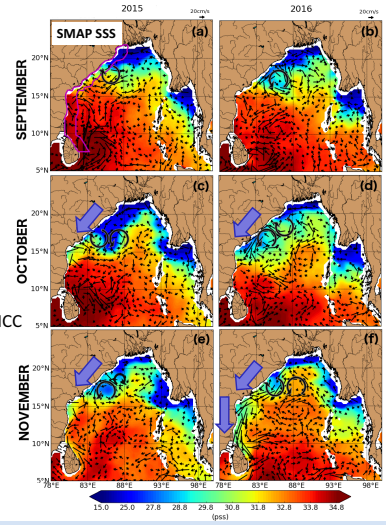

2015: "river in the sea" confined north of 13°N - far weaker EICC

2016: "river in the sea" extends further south to Sri Lanka

The freshwater plume extends further south in 2016 than in 2015

CAUSES ?

6 - CAUSE 1: LARGE SCALE INDIAN OCEAN DIPOLE

Method: Projection of ocean parameters (η=SLA or currents) on the IOD index to study the effect of the IOD

The freshwater plume transport is influenced by the IOD because the latter modulates the strength of the EICC (coastal current)

$\eta(year,month) - \eta_{ISC}(year,month) = IOD_{index}(year)*\eta_{IOD}(year,month) + \eta_{RES}(year,month)$

- $\eta(year,month) - \eta_{ISC}(year,month)$: *Departure from the seasonal cycle*
- $IOD_{index}(year)*\eta_{IOD}(year,month)$: *IOD signal*
- $\eta_{RES}(year,month)$: *Residual (reflects meso-scale oceanic eddies)*

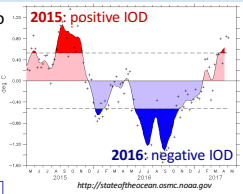

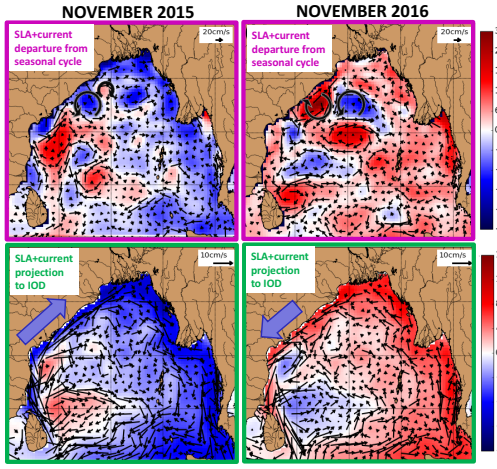

2015
Negative SLA anomalies explained by the positive IOD

Strong northward current anomaly

↓

anomalously weak southward EICC and freshwater transport

2016
Positive SLA anomalies explained by the negative IOD

Weak current anomaly northward

↓

anomalously strong southward EICC and freshwater transport

7 - CAUSE 2: MESO SCALE EDDY VARIABILITY

Mesoscale eddies influence the cross-shore transport, affecting the along-shore transport

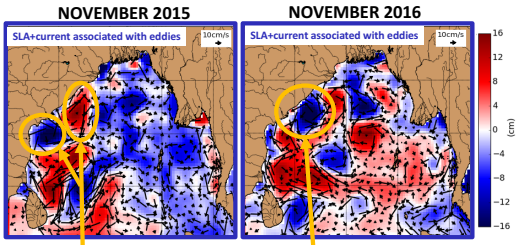

2015
anticyclonic + cyclonic eddies prevent the southward transport of the freshwater plume and export it offshore

2016
cyclonic eddy carries freshwater plume southward

8 - CONCLUSIONS

- First demonstration of the satellite SSS capability to monitor the spatiotemporal distribution of freshwater in BoB coastal regions
- SMAP provides unprecedented views of the freshwater plume transported by the EICC on synoptic to interannual time scales
- Altimeter data are important to explain processes regulating the freshwater plume variability
- The interannual variability of the freshwater plume is modulated by mesoscale eddies and the IOD
- SMAP can help improve our understanding of salinity impacts on regional climate, tropical cyclones, and oceanic productivity

National Aeronautics and Space Administration
Jet Propulsion Laboratory
California Institute of Technology
Pasadena, California
www.nasa.gov

Poster No. EB 23